Title
Characterization and Applications of a CdZnTe-Based Multimode Imager

Author
Galloway, Michelle

Publication Date
2014

Peer reviewed|Thesis/dissertation

Characterization and Applications of a CdZnTe-Based Gamma-Ray Imager

by

Michelle Lee Galloway

A dissertation submitted in partial satisfaction of the requirements for the degree of

Doctor of Philosophy

in

Engineering - Nuclear Engineering

in the

Graduate Division

of the

University of California, Berkeley

Committee in charge:

Professor Kai Vetter, Chair
Professor Steven E. Boggs
Professor Eric B. Norman
Dr. Mark Amman

Spring 2014

Characterization and Applications
of a
CdZnTe-Based Gamma-Ray Imager

Abstract

Characterization and Applications
of a
CdZnTe-Based Gamma-Ray Imager

by

Michelle Lee Galloway

Doctor of Philosophy in Engineering - Nuclear Engineering

University of California, Berkeley

Professor Kai Vetter, Chair

Detection of electromagnetic radiation in the form of gamma rays provides a means to discover the presence of nuclear sources and the occurrence of highly-energetic events that occur in our terrestrial and astrophysical environment. The highly penetrative nature of gamma rays allows for probing into objects and regions that are obscured at other wavelengths. The detection and imaging of gamma rays relies upon an understanding of the ways in which these high-energy photons interact with matter.

The applications of gamma-ray detection and imaging are numerous. Astrophysical observation of gamma rays expands our understanding of the Universe in which we live. Terrestrial detection and imaging of gamma rays enable environmental monitoring of radioactivity. This allows for identification and localization of nuclear materials to prevent illicit trafficking and to ultimately protect against harmful acts. Additionally, terrestrial-based detection is essential, for example, in monitoring the widespread contamination within the Fukushima prefecture in Japan as a result of a nuclear power plant accident.

This dissertation focusses on the development and characterization of a gamma-ray detection and imaging instrument and explores its capabilities for the aforementioned applications. The High Efficiency Multimode Imager, HEMI, is a prototype instrument that is based on Cadmium Zinc Telluride (CdZnTe) semiconductor detectors. The detectors are arranged in a two-planar configuration to allow for both Compton and coded-aperture imaging. The front plane consists of active detectors in a random mask pattern to serve simultaneously as a coded mask and a Compton scatter plane, thus providing high detection efficiency. The use of multimode imaging extends the energy range to allow for localization of sources with gamma-ray emissions from tens of keV to a few MeV.

HEMI was initially developed as a prototype instrument to demonstrate its capabilities for nuclear threat detection, spectroscopy, and imaging. The 96-detector instrument was developed and fully characterized within the laboratory environment, yielding a system energy resolution of 2.4% FWHM at 662 keV, an angular resolution of 9.5° FWHM at 662 keV in

Compton mode, and a 10.6° angular resolution in coded aperture mode. After event cuts, the effective area for Compton imaging of the 662 keV photopeak is ∼0.1 cm^2. Imaging of point sources in both Compton and coded aperture modes have been demonstrated. The minimum detectable activity of a ^{137}Cs at a 20 m distance with 20 seconds of observation time is estimated to be ∼0.2 mCi in spectral mode and ∼20 mCi in Compton imaging mode. These performance parameters fulfilled the requirements of the nuclear security program.

Following the Fukushima Dai-ichi Nuclear Power Plant accident of March, 2011, efficient methods to assess levels of radioactive contamination over large areas are needed to aid in clean-up efforts. Although a field study was not initially intended for the HEMI prototype, its portability, low mass, and low power requirements made it a good candidate to test Compton imaging from an aerial platform. The instrument was brought to Japan in August, 2013, allowing for the first test of a Compton imager from a helicopter. The instrument and detectors proved reliable and performed well under high temperature, high humidity, and vibrations. Single-detector hit energy resolutions ranged from 2.5 - 2.8% FWHM at 662 keV. The field testing of the HEMI instrument in Fukushima revealed areas of higher activity of cesium among a diffuse background through aerial-based countrate mapping and through ground measurements. Although the Compton reconstructed events were dominated by random coincidences, preliminary Compton imaging results are promising.

A future mission in medium-energy gamma-ray astrophysics would allow for many scientific advancements, e.g., a possible explanation for the excess positron emission from the Galactic Center, a better understanding of nucleosynthesis and explosion mechanisms in Type Ia supernovae, and a look at the physical forces at play in compact objects such as black holes and neutron stars. A next-generation telescope requires good energy resolution, good angular resolution, and high sensitivity in order to achieve these objectives. Large-volume CdZnTe detectors are an attractive candidate for a future instrument because of their good absorption, simple design, and minimal or no cooling requirements. Using the benchmarked HEMI CdZnTe detectors, a Compton telescope with a passive coded mask was designed and simulated with the goal of creating a very sensitive instrument that is capable of high angular resolution. The simulated telescope showed achievable energy resolutions of 1.68% FWHM at 511 keV and 1.11% at 1809 keV, on-axis angular resolutions in Compton mode of 2.63° FWHM at 511 keV and 1.30° FWHM at 1809 keV, and is capable of resolving sources to at least 0.2° at lower energies with the use of the coded mask. An initial assessment of the instrument yields an effective area of 183 cm^2 at 511 keV and an anticipated all-sky sensitivity of 3.6 x 10^{-6} photons/cm^2/s for a broadened 511 keV source over a 2 year observation time. Additionally, combining a coded mask with a Compton imager to improve point source localization for positron detection has been demonstrated.

♥

"There isn't a particle
in creation
that doesn't carry
your Light

Yesterday I was asking others
for a sign of You
Today there isn't a sign
that isn't of You."

—Jami

♥

Contents

List of Figures

List of Tables

Acknowledgments

This dissertation reflects the effort and support of many people who have contributed to the HEMI project as well as towards my scientific growth. It has been a great honor and privilege to work with the following people, to whom I am sincerely grateful:

- Professor Steve Boggs, my research advisor, for his unfailing encouragement, optimism, and patience, for his continual interest in the success of the HEMI project and in my professional development, and for providing me with various opportunities to pursue my scientific interests. I am very grateful for his open-door policy, which allowed for many clarifying discussions throughout the course of the project. He generously shared with me his knowledge and expertise, and cultivated my abilities through the way he approached and solved problems with clarity, intuition, and common sense. I am so thankful that he took me on as a graduate student and welcomed me into his group.

- Professor Kai Vetter for the many opportunities he has provided me throughout my time in the Ph.D. program. I am very grateful for his encouragement and support of my admission into the program, for everything I have learned from him about radiation detection, and for the expert advice he provided throughout the course of this work. The opportunity to field test HEMI in Fukushima would not have been possible without his leadership, dedication to the project, and his concern about the situation in Japan.

- Dr. Mark Amman, the principal investigator of HEMI, for his vital role in the project, for serving on my qualifying exam and dissertation committee, and for entrusting me with the handling and care of the detectors and the instrument. I have appreciated the knowledge he shared with me in the laboratory and on the whiteboard, and for doing so with remarkable clarity, thoroughness, and patience. I am also grateful for his invaluable advice and pep talks on getting through grad school and beyond.

- Professor Rick Norman for serving on my dissertation committee and as the chair of my qualifying exam committee. I am grateful that he fueled my interest in nuclear physics through his inspiring lectures and for his patience and thoughtful responses to my many questions.

- Dr. Andreas Zoglauer, my esteemed mentor, who was a main contributor to the HEMI project and without whom this work would not have been possible. He deserves my

utmost gratitude for his patience, guidance, inspiration, finely-tuned analysis package, meticulous proof-reading of my work, for cheering me on in the best of times and providing me with chocolate in the darkest of times. I am so thankful for his generosity of time and spirit, his cultivation of my abilities, and for his friendship.

- Dr. Cornelia Wunderer, who welcomed me into the HEMI group in the beginning, and for the invaluable first bits of analysis methods and ROOT programming I learned from her.

- Paul Luke for introducing the HEMI concept and for his hard work, dedication, and expertise that went into developing the detectors and the instrument. I am especially grateful for his generosity of time in preparing for the field tests, such as redesigning the HEMI box, completely reassembling the instrument and allowing me to help, and coming in to troubleshoot in a moment of crisis. Without Paul the HEMI project would not have been possible.

- Julie Lee for her meticulous work and expertise in the laboratory as well as Victor Negut and Anders Priest for helping with CdZnTe testing during the early stages of the project.

- In addition to the direct help I received with the HEMI project at Berkeley, I was very fortunate to participate in enlivening and helpful discussions with the high-energy astrophysics group at Space Sciences. I am especially grateful to Dr. John Tomsick for offering great advice and readily sharing his knowledge with me, to Dr. Nicolas Barrière for his encouragement and friendship, and to Dr. Philip von D. for believing in me. I am also grateful for the camaraderie, good humor, and helpful feedback from my fellow graduate students, Alex, Carolyn, and Francesca, and to all of the unnamed past and present members of the group for their advice and companionship.

- Lisa Zemelman for guiding me through the administrative aspects of the program.

- The U.S. Department of Homeland Security, Domestic Nuclear Detection Office, and the Department of Energy for funding the HEMI project and for granting us permission to bring HEMI to Japan and fly it.

"The laws of nature transcend international boundaries." – Arthur H. Compton

I am very honored to have been given permission to witness the present situation in Fukushima and to have, perhaps, contributed in some small way to the recovery effort. The field testing of the HEMI instrument in Fukushima was only possible because of the care, dedication, and hard work of many people. I would like to express my gratitude to the following groups and individuals:

- The Applied Nuclear Physics group at LBNL: Dr. Benjamin Sturm for his role in managing the project, for readily sharing his expertise on CdZnTe detectors with me, and for his conviviality, Dr. Daniel Chivers for the copious amounts of time and effort he spent in designing the enclosure and in specifying many of the components, Dr. Donald Gunter and Andy Haefner for useful discussions on imaging, Dr. Mark Bandstra for good advice on various topics, Gabrielle Scott for taking care of several necessary details of the project, and Dr. Brian Quiter for his recommendation on time travel via Google. My utmost gratitude goes to John Kua for all of his hard work, knowledge, attention to detail, support in the field, and for his companionship.

- Professor Hiroyuki Takahashi for welcoming me into his group and hosting me over the summer. I am sincerely grateful for his careful arrangement of many opportunities during my time there, such as meetings with other professors, the summer school, and, of course, the field tests. He was responsible for making all of the arrangements with the JAEA and local governments which allowed us to enter and conduct tests in Fukushima. Because of his kindness and generosity I learned many valuable things about detection systems, the situation in Fukushima, and Japanese culture.

- Professor Kenji Shimazoe for his guidance in the laboratory, in the field, and with the analysis. His hard work and dedication as well as his consistently cheerful spirit was an inspiration. I am also grateful that he did not laugh too often at my poorly spoken Japanese.

- Dr. Tadayuki Takahashi and Dr. Takeda of JAXA for sharing their knowledge and experience with me regarding Compton imaging, specifically as applied to Fukushima. Their advice proved invaluable both in the field and during the analysis stages. I am very grateful for their generosity.

- Professor Tanimori of Kyoto University for his advice and foresight regarding the aerial measurements and subsequent analysis. I am grateful to him and his students for welcoming me at the University and providing thorough answers to my questions.

- I am very grateful to all of my friends and fellow students in the Takahashi group. I received a tremendous amount of help throughout the summer with everything from meeting me at the train station on my first day to helping with the safe return of HEMI on my last day. I had many wonderful experiences with group members, such as climbing Fuji-san, discovering umi hotaru, and learning true enjoyment of udon. Gambatte kudasai!

- Kami for many things, especially for fine flight weather.

✿

I am grateful for the funding and support I received through the Soroptimist Foundation, the National Science Foundation EAPSI program, and the Dissertation-Year Fellowship through the University of California at Berkeley.

✿

In addition to those who directly contributed to this work, I greatly appreciate the many wonderful people who have offered me their support, love, and kindness along the way:

- My family, especially my mother for her nurturance, prayers, and compassion, and to my father for teaching me a strong work ethic and for always supporting my decisions. I am also grateful for having grown up with loving grandparents, my encouraging sister, and my endearing brother, as well as my nieces and nephews for brightening my life.

- Dr. Jennifer Hudin for her continual encouragement, for serving as a role model, and for many fruitful and inspiring philosophical discussions. I am especially grateful to her for always holding a bigger perspective of my work throughout the trials and tribulations of the past 5 years.

- Dr. Carmen Hering for her professional care, wisdom, and love, and Dr. Randy Specterman, for her deep insights and compassionate approach to removing obstacles. I am grateful to both of them for their significant contributions to my well-being.

- Yumi Kori for her friendship, openness, and generosity, and for providing me with a place I could call home during my summer in Tokyo. Her creativity, honesty, and deep concern about the current situation in Japan was a source of strength for me and fostered my sense of purpose.

- Craig Coss who has helped me tremendously over the years. With painstaking attention to detail, persistence, and patience he has guided me through many a poster, presentation, and allegorical situation. He deserves my utmost gratitude for sharing his artistic skills and depth of knowledge with me, as well as for always kindly lending me his ear.

- Barbara Cushing, my dear friend, for still listening to me and making me laugh.

- Zoe, Barbara S., Cynthia, and Anat for offering me a space to write and to be, Hannah, Michelle M., and Catrina for their encouragement and companionship over the years, and the many unnamed people who have supported and guided me in my life and in my work.

- Last but not least, I am deeply grateful to Dr. Llewellyn Vaughn-Lee for recognizing my potential from the very beginning, for focussing my attention towards what is essential, and for the many things he taught me and gifts I was given through grace and love.

Chapter 1

Introduction

Gamma-ray photons are a type of electromagnetic radiation that can be produced in a wide range of phenomena, for example, in nuclear transitions, in high energy acceleration processes such as Bremsstrahlung or synchrotron radiation, or through annihilation of matter with its antimatter counterpart. In the soft to medium-energy gamma-ray range, the emitted photons can have energies from 0.1 MeV to 10 MeV, corresponding to wavelengths between 10^4 and 100 femtometers. Additionally, highly energetic astrophysical processes, such as gamma-ray bursts or jets from Active Galactic Nuclei, can produce gamma-ray photons from $\sim$0.1 MeV to more than 1 TeV in energy.

Gamma-ray detection relies upon the understanding and predictability of how high-energy photons interact with matter in order to confirm the presence of sources of emission. Detection and imaging technologies are driven by the need to maximize gamma-ray source photon interactions within a detector material while allowing for background reduction in the resulting signals. The primary purpose of advanced detector technologies and imaging instrumentation is to infer the presence of sources, to spectroscopically characterize the energy and type of emission, and to deduce the intensity, location, and morphology of sources.

1.1 The Discovery and Nature of Gamma Rays

The existence of gamma radiation was first reported by the French physicist Paul Villard in 1900 (*Gerward*, 1999). Using a radium source provided by the Curies, Villard set out to investigate the reflective and refractive properties of beta rays. In the process he found that a third type of radiation exists that is non-deviable by a magnetic field and appeared to be a highly penetrating type of X-ray. Its existence was subsequently confirmed through the work of Bequerel, Curie, and Rutherford, with the designation of "gamma ray" first appearing in a publication by *Rutherford* (1903). This electrically neutral type of radiation was made visible using radiography that could be intensified through the use of fluorescent screens and was also evident from the ionization of gases in proximity to a source. However at this time the nature of gamma rays, as well as the nature of X-rays which were discovered by Roentgen in

1895, was still not understood (*Nobel Lectures*, 1967). The emission from radioactive sources did not exhibit the characteristic diffraction or interference patterns expected from the wave nature of light. X-rays and gamma rays were observed to be particulate in nature, and at this time the particle-wave duality of light had not yet been realized.

In 1912 M. von Laue conjectured that the atomic spacing in crystals would be on the same order as the wavelength of X-rays (*Eckert*, 2012). If this were the case, X-rays incident upon certain crystals would reveal diffractive patterns similar to the way in which optical light is refracted through a prism. Knipping and Friedrich at the University of Munich proved Laue's hypothesis to be true. The experiment as proposed by Laue produced dots of light on a photographic plate, revealing the lattice structure of calcium sulfate used in the experiment. An experiment conducted in 1914 by Rutherford and Andrade using gamma rays incident upon a crystal revealed similar results (*Rutherford*, 1914). Thus it was concluded that X-rays and gamma rays exhibit both a particle and a wave nature, and subsequently were types of electromagnetic radiation.

Prior to the work by von Laue, in 1907 Charles Barkla showed that the intensity of scattered X-rays varied with scattering angle, consistent with Thomson's theory, and also found that X-rays could be polarized (*Galison*, 1997). Following this work and Laue's studies of the diffractive properties of X-rays, Arthur H. Compton proceeded to experiment with X-rays and found that they had a preferential scattering direction, and that the "echo" from scattering was found to be at longer wavelengths than the incident rays. Compton derived a clear relationship between the increase in scattering angle and the increase in the wavelength shift of the incident photon, known as the Compton effect (*Compton*, 1923). Experimentation by Compton provided further evidence of the particulate nature of light.

1.2 Mechanisms for Gamma-Ray Production

Gamma rays can be produced by a number of different physical processes. They are emitted from production sites and sources as either nuclear lines, e.g., through nucleosynthesis or annihilation, or as continuum spectra, which generally is a result of acceleration processes. The primary production mechanisms of high-energy photons are from up-scattering of photons through collisions with energetic particles, i.e. inverse Compton scattering, the acceleration of charged particles in strong magnetic or gravitational fields, e.g., synchrotron radiation or Bremsstrahlung, nuclear transitions in atomic nuclei, e.g., nuclear de-excitation, beta decay, alpha decay, or pion decay, and annihilations of particle and anti-particle pairs. Detailed information about these processes can be found in *Rybicki and Lightman* (2004) and *Krane* (1988). For the purpose of this work, the gamma-ray band will refer to photons with a minimum energy of tens of keV, although it is noted that many of the lower energy photons are generated through atomic transitions (X-rays) rather than through nuclear transitions or one of the above described processes.

1.3 Sources of Gamma Rays and Applications

Sources of gamma-ray emission are varied and can occur naturally or as a result of man-made processes. The detection, spectroscopy, and imaging of these sources have many applications. This section provides an overview of different sources of gamma-ray emission as well as the motivation for detecting these sources.

1.3.1 Nuclear and Particle Physics

Gamma-ray detection and spectroscopy are important tools that allow for an understanding of nuclear properties as well as fundamental physics processes. Predominately, any nuclear decay or reaction that leaves the nucleus in an excited state can decay with the emission of one or more gamma rays. Because the nucleus is a quantum system, the emitted photon energy is quantized and subsequently characteristic of the difference in nuclear states. This characteristic gamma-ray energy thus provides a unique signature that allows for isotopic identification through spectroscopic analysis. These well-defined energies also allow for an understanding of properties of the nucleus and nuclear states. Additionally, information about the angular distributions as well as polarization measurements can be used to determine, e.g., allowable nuclear state transitions, decay channel probabilities, isospins, and parities (*Krane*, 1988).

In addition to understanding properties of the nucleus, gamma-ray detection is useful in the field of particle physics. First, specific gamma-ray energies can provide a characteristic signature that reveals either the presence of a specific particle or the occurrence of a specific nuclear reaction. For this reason, gamma-ray detection technologies are used in particle physics experiments such as neutrino detection (*The Super-Kamiokande Collaboration*, 2003), direct dark matter searches (*Aprile and Doke*, 2010), and in accelerator experiments, such as the Higgs search at the Large Hadron Collider (*The CMS collaboration*, 2013). Secondly, many of these experiments require a very low radioactive background in order to detect the sought-after signal. For this reason, detection technologies are used to understand the backgrounds, eliminate sources of background through detection or event cuts, and subsequently to increase the statistical significance of a positive detection. Thus, the development of gamma-ray detection techniques have allowed for significant advancements in fundamental physics research.

1.3.2 Astrophysics

The intense electromagnetic and gravitational forces that are at play in our Universe can lead to events of extreme violence, such as stellar explosions, e.g., core-collapse and thermonuclear supernovae, cosmic acceleration of particles, e.g., pulsars and supernovae remnants, as well as the creation of powerful compact objects, such as black holes and neutron stars. The high energies involved in such processes often result in the release of continuum or line emission at gamma-ray energies. Because of the highly penetrative, non-deviable nature of gamma

rays, they can provide a direct line-of-sight back to the source of emission, opening a unique window into the underlying astrophysical processes that are unobservable by other means. Several primary sources of astrophysical gamma-ray emission are briefly described below.

1.3.2.1 Nuclear Line Sources

Nuclear line emission in astrophysics comes from radioactive decay, nuclear de-excitation, neutron capture, or pair production and annihilation of standard model particles, e.g., electron-positron pairs, or, theoretically, exotic particles such as dark matter candidates. The observation of lines and their relative abundances can yield information about the underlying nuclear structure and physics processes within stellar interiors, burning regions of late-stage massive stars, and dynamics within the interstellar medium. This information helps in the understanding of how heavy elements are formed and traverse through the cosmos. Additionally, the shape of an observed nuclear line can reveal the dynamics of the line source, namely, a line can become Doppler broadened or shifted as a result of stellar kinematics.

Table 1.1 lists four prominent types of nuclear line emissions. The first section includes some of the isotopes generated through cosmogenic sites of nucleosynthesis. Primordial nucleosynthesis can explain only a small fraction of nuclei heavier than ^{4}He (*Burbidge*, 1957). The remaining isotopic abundances are a result of nuclear fusion inside stars, processes that occur during different stages of stellar evolution, e.g., explosive hydrogen burning in novae or hydrostatic burning in supernovae (SNe), as well as nuclear reactions that take place within the interstellar medium (*Diehl*, 2013). These processes can lead to the creation of both stable and unstable isotopes, the latter can decay through the emission of gamma-ray lines.

Two notable observations of nuclear lines were obtained by COMPTEL (see Chapter 2.4) which allowed for the first all-sky map of ^{26}Al, and by RHESSI (*Lin*, 2002) which measured the ratio of ^{26}Al to ^{60}Fe. The latter measurement was also confirmed by INTEGRAL/SPI (*Harris*, 2005). These isotopes are thought to be produced from core-collapse supernovae and from late-stage burning in massive stars. The half-lives of ^{26}Al ($t_{1/2}$ $\sim$7x10^5 y) and ^{60}Fe ($t_{1/2}$ $\sim$2x10^6 y) are long enough to allow for accumulation in the interstellar medium, yet short in comparison to the age of most stars, thus providing for a tracer of nucleosynthesis in these sites. The COMPTEL all-sky map showed the ^{26}Al lines to be consistent with the locations of massive star regions along the Galactic plane (*Oberlack*, 1996).

One source of positron emission is the β^+ decay of isotopes from cosmogenic nucleosynthesis. The emitted positrons annihilate with electrons and produce a distinct signature of 511 keV gamma-ray lines. These lines have been observed in locations consistent with the ^{26}Al line emissions, for example. However, β^+ decay alone cannot explain the observed diffuse abundance of positrons across our Galaxy. This is particularly the case in regard to the excess positrons in the Galactic Center region with extension of size $\simeq 10^\circ$ (*Knödelseder et al.*, 2005).

In addition to positrons from β^+ decay, several mechanisms may lead to the production of electron-positron pairs, e.g., jets from compact objects, high-energy collisions, high

magnetic fields. For example, compact objects such as pulsars and microquasars can lead to positron emission, although the location of these sources as observed through other energy bands have not been correlated to the distribution or abundance of Galactic positrons.

In general, the detection of a 511 keV line points to the production of positrons, and the line shape yields information about the positron production environment, such as its temperature. However the propagation of positrons and positronium (a bound electron and positron pair) from their production sites makes tracing the lines back to their sources rather indirect. This is one reason why the source or sources of excess positrons are still unknown. A list of candidate sources can be found in *Prantzos et al.* (2011). Future gamma-ray observation missions with high sensitivity and good angular resolution may help to solve this mystery.

Decay Chain	Energy (keV)	Observation Sites
$^{26}\mathrm{Al} \rightarrow {}^{26}\mathrm{Mg}$	1809, 511	Galactic Plane, Vela, Cygnus, Sco-Cen
$^{60}\mathrm{Fe} \rightarrow {}^{60}\mathrm{Co} \rightarrow {}^{60}\mathrm{Ni}$	59, 1173, 1332	Galactic Plane
$^{44}\mathrm{Ti} \rightarrow {}^{44}\mathrm{Sc} \rightarrow {}^{44}\mathrm{Ca}$	68, 78, 511, 1157	Cassiopeia A
$^{56}\mathrm{Ni} \rightarrow {}^{56}\mathrm{Co} \rightarrow {}^{56}\mathrm{Fe}$	158, 511, 812, 847, 1238	SN 1987A
$^{57}\mathrm{Co} \rightarrow {}^{57}\mathrm{Fe}$	122, 136	SN 1987A , SN 1991T
$\mathrm{e}^{+} \rightarrow \gamma\gamma$	511	Galactic Plane, bulge, disk
$\mathrm{H(n,\gamma)^2H}$	2.22 MeV	solar flares
$^{12}\mathrm{C}^{*}$	4.44 MeV	solar flares
$^{16}\mathrm{O}^{*}$	6.13 MeV	solar flares

Table 1.1: Prominent astrophysical nuclear line emissions (*Diehl*, 2013).

The (n,γ) reaction listed in Table 1.1 refers to neutron capture by a proton resulting in the formation of a deuteron. This nuclear fusion reaction results in the release of a gamma ray with energy equivalent to the binding energy of the deuteron, i.e. 2.22 MeV. In order for this reaction to happen, the neutron must first be thermalized by collisions within a medium, as the cross-section for capture is inversely proportional to the neutron's velocity. Additionally, free neutrons have a mean lifetime of $\sim$14 minutes, therefore the location of an observed 2.22 MeV line must occur near a source of neutrons. Because of these restrictions, it follows that the observation of this line in the vicinity of a neutron star requires that the neutron capture must occur near the surface of the star. The strong gravitational field of the neutron star and the environment in the capture region would cause the line to be gravitationally redshifted and broadened depending on how close to the surface of the star the interaction took place. The amount of broadening and redshift of the line could be used to directly probe the mass-radius ratio of a neutron star, thus providing one strong component in constraining the neutron star equation of state (*Bildsten*, 1993).

No redshifted neutron capture lines have so far been observed, but unredshifted lines have been detected from solar flares. Because the observed lines were spatially separated from observed hard X-ray Bremsstrahlung, it lead to the conclusion that the acceleration processes in solar flares were different for ions than for electrons (*Lin et al.*, 2003).

Finally, collisions of cosmic rays in the interstellar medium with abundant nuclei such as ^{12}C and ^{16}O can lead to excitation and subsequently de-excitation through gamma-ray emission as noted in Table 1.1. The lines were first thought to be observed in the Orion region, but later were found to be a spurious result (*Bloemen et al.*, 1999). These de-excitation lines have been observed in coincidence with solar flares (*Lin et al.*, 2003).

1.3.2.2 Continuum Sources

Astrophysical sources with extreme gravitational fields, magnetic fields, or both can accelerate particles, leading to the emission of continuum gamma-ray emissions through such processes as, e.g., inverse Compton scattering, synchrotron radiation, Bremsstrahlung, and the production of pair plasmas. These sources include Active Galactic Nuclei (AGN), stellar-mass compact objects such as black holes or pulsars, and gamma-ray bursts (GRB)s. Spectral observations of continuum emissions can inform theoretical models regarding the dynamics of these sources and their acceleration mechanisms, however measurements of gamma-ray polarization are essential for decisively constraining the models.

1.3.3 Radiation in the Terrestrial Environment

Several natural sources of gamma rays exist in the environment. For example, ^{40}K and isotopes from the uranium and thorium decay chains, such as radon, are naturally prevalent in soil and consequently are found in many building materials. Cosmic rays that enter the Earth's atmosphere can lead to the excitation of atmospheric nuclei and the subsequent emission of gamma rays and are a natural component of the gamma-ray background. Among these cosmogenic nuclides is ^{14}C, as it is produced from cosmic ray excitation and decay of atmospheric ^{14}N. However excess ^{14}C and other gamma-ray background sources, predominately ^{134}Cs and ^{137}Cs, were dispersed into the environment as a result of nuclear weapons testing fallout. Additionally, nuclear power plant accidents and, historically, the disposal of low-level radioactive waste into the environment (*IAEA*, 1999) have also lead to an increase in the gamma-ray background.

In addition to these predominately diffuse sources, specific isotopes that are used for medical diagnostics, e.g., ^{123}I and ^{99m}Tc, and those used for industrial purposes, e.g., ^{137}Cs and ^{60}Co, can be detected in the environment. By localizing, spectroscopically characterizing, and estimating the activity of these sources, they can be distinguished from natural and other man-made sources of emission in the environment.

Understanding and gaining perspective on the types and typical activities of gamma-ray emission sources in the environment provides the basis for setting standards for detection of radioactive anomalies as well as for informing environmental remediation activities. Ad-

ditionally, the ability to accurately measure and characterize background isotopes can be applied to radioactive dating in geophysics, archaeology, and also has applications in nuclear forensics.

1.3.3.1 Environmental Remediation

Historically, nuclear weapons production and testing and nuclear power plant accidents, e.g., Chernobyl, Three Mile Island, Fukushima, have necessitated the use of gamma-ray detection technologies for environmental remediation purposes. Radioactive materials that are released into the environment pose a threat through direct airborne exposure and as a potential contaminant of food and water sources. The exposure can be short-term, such as the uptake through food and dairy products of ^{131}I with its half-life ($t_{1/2}$) of 8 days, or long-term, such as the chronic exposure from ^{137}Cs, $t_{1/2}$= 30 years, that may be dispersed in the environment and last for generations. Additionally, nuclear weapons production and test sites can have residual contamination of very long-lived in addition to extremely toxic heavy radioactive isotopes, such as uranium and plutonium.

The characterization and monitoring of contaminated areas requires consistent and reliable technologies in order to assess the activity, spectroscopic characterization, and distribution of radioactive contamination within the environment. Detection technologies are needed to ensure that radioactive contaminants are first contained and then safely and effectively removed. This includes understanding the transport of contamination through air, on ground, and also in groundwater. Monitoring the presence and spread of contamination allows for estimating dose rates and setting safe limits of exposure times for humans. From this information, appropriate boundaries on geographical areas that are safe for human habitation can be designated. Additionally, imaging of contaminated areas has the potential to make these environmental assessment tasks more efficient and effective, as will be discussed in Chapter 6.

1.3.3.2 Nuclear Security

The capability to produce, the illicit trafficking of, and the possession of nuclear weapons or special nuclear materials (SNM) by rogue individuals, groups, and non-nuclear weapons states is considered to be the primary nuclear threat to world security and public health at this time in history. In order to detect the presence of these type of weapons and materials as well as to enforce the nuclear nonproliferation treaty, instruments that are capable of detecting, localizing, as well as providing the ability to distinguish a threat source from a non-threat source within a reasonable amount of time are needed.

1.3.4 Nuclear Medicine

Gamma-ray detection is the basis for many of the tools used in nuclear medicine, as the use of nuclear sources provides a minimally invasive diagnostic of internal biological processes.

Relatively short-lived gamma-ray emitting isotopes such as ^{123}I or ^{99m}Tc are introduced into the body and accumulate in the organ or region to be imaged. The emissions from these isotopes are absorbed or scattered as they travel through the organ based upon the variabilities in density or structures present in the tissue. The emissions can be collimated and detected and Compton imaged with a gamma camera, achieving good spatial resolution and depth resolution of the imaged organ. The detection and imaging of emissions allows for a visual diagnostic of the structure and function of the organs.

In the case of positron-emission tomography, a positron emitting isotope is introduced into the tissue or organ to be diagnosed. The positron subsequently annihilates with an electron within the tissue, releasing two coincident 511 keV photons that travel in opposite directions from one another. The photons are detected within a surrounding detector array, yielding spatial information about the line of original decay based upon the directionality of the detected photons. Repeated annihilations result in imaging at specific depths within the body, providing a visual reconstruction of the structure and function of the area of concern.

1.4 Summary

The discovery of gamma rays opened a door to a previously unseen aspect of our electromagnetic universe as well as provided humanity with a deeper understanding about the nature of light. As nuclear science and technology evolved, insights into particle and astrophysical phenomenon through observations in the gamma-ray energy regime followed. The development of gamma-ray detection technologies also addresses critical issues in human and environmental health and security, as well as provides an important perspective on our changing terrestrial and astrophysical environment.

Chapter 2

Detection and Imaging

Understanding gamma-ray interactions with matter provides the basis for detection, spectroscopy, and imaging of gamma-ray emitting sources. This chapter describes the underlying physical processes that enable detection and localization of low to medium-energy gamma-ray emission sources, i.e. tens of keV up to a few MeV. Detector materials and technologies that are applicable to this energy range are summarized, along with a few historical and contemporary examples of gamma-ray spectrometers and imagers.

2.1 Gamma-ray Interactions in Matter

Detection of radiation depends upon the ability to recognize and quantify the interactions of gamma-ray photons within matter, in this case within the material of the detector. An incoming gamma-ray photon can become absorbed in the detector material, scatter coherently or incoherently, produce pairs of matter and antimatter, or pass through the material without interaction. Within the energy range of a few keV up to several MeV, the primary interaction processes are photoelectric absorption, Compton scattering, and pair production (nuclear). The probabilities of each of these interactions depend upon the incoming photon energy and the atomic number (Z) of the detector material. For Cadmium Zinc Telluride detectors (average Z = 49), a comparison of the dominant photon interaction cross sections are shown in Fig. 2.1.

2.1.1 Photoelectric absorption

Photoelectric absorption occurs when an incident gamma-ray photon with an energy greater than the binding energy of an atomic electron interacts with an atom, resulting in the complete absorption of the photon and the ejection of an electron from one of its bound shells (*Knoll*, 2010). The vacancy in the electron shell is quickly filled by an outer shell electron, resulting in the emission of a characteristic X-ray or an Auger electron. A recoil of the atom from this interaction is required for conservation of momentum, however in the gamma-ray

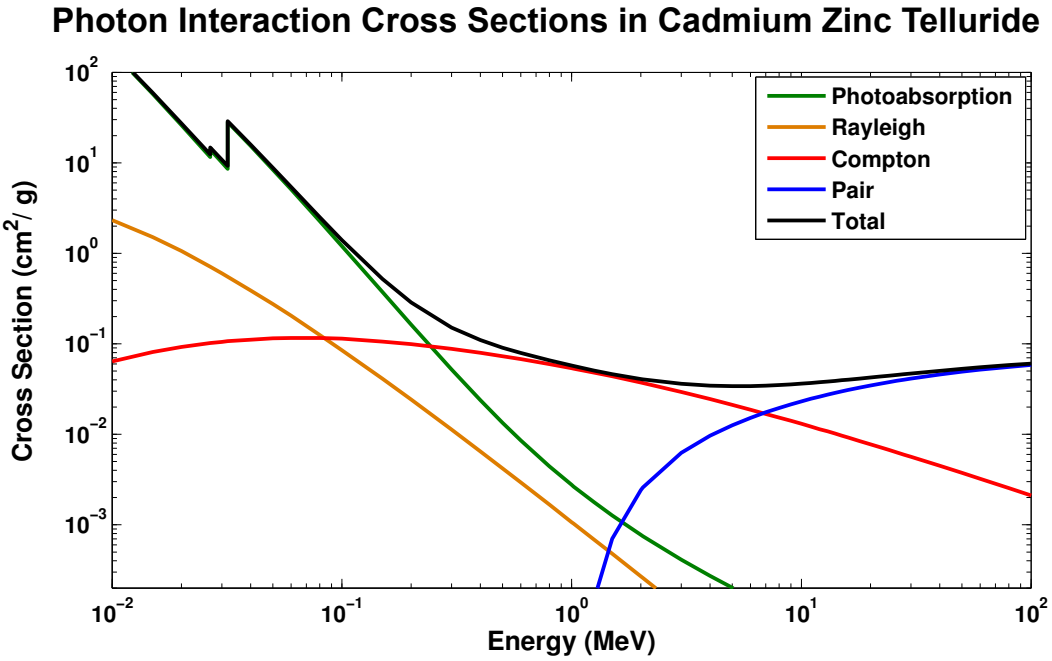

Figure 2.1: Dominant interaction processes of gamma-ray photons in Cadmium Zinc Telluride as a function of energy (data from *Berger*, 1998).

energy range dominated by photoelectric absorption this energy is negligible. Therefore the initial photon energy is transferred into the kinetic energy of the ejected electron minus the binding energy required to eject the electron. For CdZnTe the binding energies range from 10 eV up to ∼30 keV (*Fuggle*, 1980). In Fig. 2.1 one can see a discontinuity in the photoelectric absorption cross section at 27 keV, corresponding to the K-absorption edge of cadmium. Photoelectric absorption is the dominant process for x-rays and low energy gamma rays. In CdZnTe, photoelectric absorption dominates at energies below about 200 keV. The photoelectric absorption process is illustrated in Fig. 2.2.

2.1.2 Compton Scattering

Compton scattering is an incoherent scattering process that occurs when an incident photon scatters off of a free or bound electron and subsequently transfers some of its energy to the electron as illustrated in Fig. 2.3. Using conservation of energy and momentum, this effect is precisely described by the Compton formula, Eq. 5.2, where ϕ is the azimuthal scattering angle of the photon, $m_e c^2$ is the rest energy of the recoil electron, and E_e and E_γ represent the energies of the recoil electron and the scattered gamma-ray photon energy, respectively (*Compton*, 1923). The energy of the initial gamma-ray photon, E_i is given by the sum of these two energies as shown in Eq. 2.2.

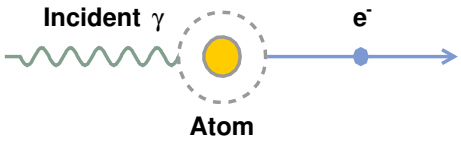

Figure 2.2: Illustration of complete photoelectric absorption of a photon resulting in the ejection of an atomic electron (X-rays and Auger electrons not shown).

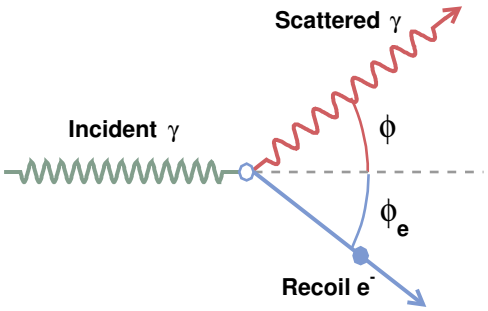

Figure 2.3: Illustration of an incident photon Compton scattering off of a free electron.

$$cos\phi = 1 - m_e c^2 (\frac{1}{E_\gamma} - \frac{1}{E_e + E_\gamma}) \tag{2.1}$$

$$E_i = E_e + E_\gamma \tag{2.2}$$

By calculating the scatter angle using the Compton formula, the trajectory of the incoming photon corresponds to a path along a cone with opening angle ϕ. The origin of the photon is then limited to locations that lie along this Compton cone or "event circle". This is the basis for Compton imaging and will be described in further detail in the Quantum Optics section of this chapter.

One can see from Fig. 2.1 that the dominant interactions in CdZnTe within the energy range of interest (tens of keV to a few MeV) reside primarily in the Compton regime. This regime has the lowest total cross-section, indicating that Compton scattered photons are the most difficult to detect, yet many terrestrial and astrophysical sources of interest emit nuclear lines or continuum spectra within this energy regime. For this reason it is necessary to find materials and techniques that can quantify and optimize Compton interactions within a detector.

2.1.2.1 Klein-Nishina differential scattering cross-section

The angular distribution for Compton scattered gamma rays is given by the Klein-Nishina differential scattering cross-section, $(\frac{d\sigma}{d\Omega})$, Eq. 2.3, where r_e is the classical electron radius (*Klein and Nishina*, 1929). As the photon energy is increased, the likelihood of scattering in the forward direction also increases.

$$\frac{d\sigma}{d\Omega} = \frac{r_e^2}{2}(\frac{E_i}{E_\gamma})^2(\frac{E_\gamma}{E_i} + \frac{E_i}{E_\gamma} - sin^2\phi) \tag{2.3}$$

For linearly polarized gamma rays, the polarization information is preserved in Compton scattering as a cosine-shaped modification of the azimuthal scatter angle. In this case the differential scattering cross-section for linearly polarized photons is given by Eq. 2.4, where the angle between the polarization vector and the plane of the scattered photon is given by ψ.

$$\frac{d\sigma}{d\Omega} = \frac{r_e^2}{2}(\frac{E_i}{E_\gamma})^2(\frac{E_\gamma}{E_i} + \frac{E_i}{E_\gamma} - sin^2\phi cos^2\psi) \tag{2.4}$$

2.1.3 Pair Production

When the energy of a photon is equal to or exceeds twice the rest mass energy of any given particle, a quantum field interaction with the Coulomb field of a nucleus allows for the conversion of the photon into a particle and corresponding antiparticle pair. This phenomenon, illustrated in Fig. 2.4 for electron-positron pairs, is known as nuclear pair production. Analogously, a photon with energy equal to or exceeding four times the rest mass energy of a particle can produce pairs when it interacts with the electron field of an atom. This process is know as triplet production, as historically bubble chambers revealed three tracks corresponding to the electron, positron, and the recoil electron. A historical overview beginning with the prediction of the positron (*Dirac*, 1928) and its experimental confirmation (*Anderson*, 1933) can be found in (*Hubbell*, 2006).

For nuclear pair production to occur, the required incident photon energy is dictated by the threshold energy from the mass-energy equivalence. Within the medium energy gamma-ray regime, pair production is relevant for the creation of an electron-positron pair (e^+e^-), corresponding to a threshold energy of $2m_ec^2$, or 1.022 MeV.

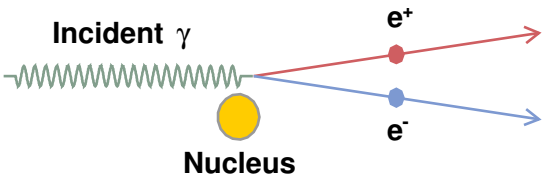

Figure 2.4: Illustration of nuclear pair production from a high energy photon entering the Coulomb field of a nucleus.

The probability for pair production increases with increasing photon energy to a plateau, as seen in Fig. 2.1. For a given detector material the cross-section increases approximately as the square of the atomic number of the material, $\sigma_{pp} \propto Z^2$ (*Oppenheimer and Plesset*, 1933). For CdZnTe, the cross-section for pair production exceeds that of Compton interactions at energies above about 7 MeV.

Pair production may also occur when a photon is in the presence of an extremely strong magnetic field, such as in the periphery of magnetars or in the primordial cosmic magnetic fields conjectured to have formed shortly after the Big Bang (*Zweibel and Heiles*, 1997). The inverse process of pair production is annihilation, where a particle and its antiparticle collide and annihilate, producing two photons with energies equivalent to the rest mass energy of the particle plus the kinetic energy of each particle at the time of collision.

Pair production and its subsequent annihilation can yield many distinct features within a gamma-ray spectrum. The full-energy peak from pair production corresponds to twice the rest mass of the electron plus any excess energy from the incident photon that is imparted to the electron and positron as kinetic energy. The presence of single and double escape peaks at energies of 511 keV or 1.022 MeV below the full-energy peak in the spectrum indicate that an incident gamma ray with energy exceeding the threshold energy produced an electron-positron pair within the detector material.

2.1.4 Rayleigh scattering

Other processes such as Rayleigh scattering can also occur within the detector material. Rayleigh scattering, as opposed to Compton scattering, is a coherent, elastic scattering process that does not result in ionization. The incoming photon scatters off of bound electrons

in the atom, preserving its initial energy but resulting in a small angle scattering of the photon. Rayleigh scattering is predominant at low energies, but one can see from Fig. 2.1 that the total interaction cross-section is still dominated by photoelectric absorption and Compton scattering. The maximum contribution from Rayleigh scattering is $< 10\%$, occurring at around 200 keV. This is the region of crossover where the Compton scattering begins to dominate over photoelectric absorption interactions. Due to the minimal contribution from Rayleigh scattering, the unchanged photon energy, and the small change in scatter angle when this interaction occurs, these effects are considered to be negligible for the detectors relevant for this work.

2.2 Detector Technologies

The ability to detect radiation relies on an interaction taking place between an incident photon and the material of the detector, whereby the photon transfers all or part of its energy within the detector material. In order to extract meaningful information from this interaction, e.g., spectroscopy, the deposited energy from the photon interaction should be proportional to the derived signal. The quality of the resulting signal depends primarily upon the detector material and geometry as well as the method of collection and signal extraction, e.g., readout electronics. The energy resolution, position resolution, time resolution, and detection efficiency are essential features used for comparisons between detectors. This section provides a brief overview of prominent detector materials and technologies used for gamma-ray detection and spectroscopy. Except where noted, the information in this section was referenced from *Knoll* (2010).

2.2.1 Gas Detectors

Gamma radiation that is incident upon a volume of gas can transfer energy to one or more of the electrons in the gas and generate an ionized atom and an electron, i.e. an ion pair. The simplest kind of gas detector that is capable of spectroscopy is the ion chamber. In this case, the ion pairs generated through direct ionization are collected by applying an electric field across the detector, causing the ion pairs to drift to their respective electrodes. In the case of ideal ion pair collection, the energy deposited in the detector gas from the incident photon can be deduced from the total collected charge. Typically noble gases (Xe, Ar) under some pressure are used in ion chambers.

Another example of a spectroscopic gas detector is a proportional counter. By applying a larger electric field across the chamber than with an ion chamber, ion pairs are accelerated and generate more ion pairs along their path. As this electric field is increased, the secondary electrons have kinetic energies that are higher than the ionization energy of the gas, and a multiplication of ion pairs in the gas takes place. In the specific case of a proportional counter, the chamber is operated with an applied voltage that allows the gas multiplication to remain linear, i.e. proportional, to the ionization energy from the initial photon interaction. This has

two distinct advantages: Gas multiplication amplifies the initial signal, thereby increasing the signal to noise ratio, and if the proportionality remains throughout the collection phase good spectroscopy can be obtained. Additionally, because the multiplication effect only takes place when an electron is very close to the anode, the gas multiplication remains independent from the depth of interaction. These factors allow for the resulting signal to be used to infer the energy of the incident radiation, providing good spectroscopy. In proportional chambers, noble gases (Ne, Ar, Xe), typically with some quenching material to limit de-excitation photons, are used at above atmospheric pressure for better efficiency. Position sensitivity can be obtained by using an array of anode wires, such as in a multi-wire proportional chamber.

A third example of a gas detector is a time projection chamber, although in this case some portion of a noble gas is liquified using cryogenics to form a combined scintillation (see next section) and gas detector. This type of detector provides spectroscopy and also allow for position reconstruction, as the signal timing and the light collection from the ionization in the gas and the scintillation in the liquid are used to deduce the energy of incident radiation as well as the position of initial interaction. More information can be found in *Nygren* (1978).

2.2.2 Scintillation Detectors

Certain materials exhibit luminescence from an interaction with ionizing radiation. In the case of organic scintillator materials, ionizing radiation can produce scintillation light in certain materials by transferring energy to an atom or molecule and inducing an excited state. The de-excitation of the atom or molecule results in photon emission in the UV or visible light waveband. In the case of inorganic scintillators, the excitation and emission is due to the electronic band structure of the crystal. Scintillating materials are coupled to one or more photomultiplier tubes or photodiodes that convert the incident light into an electrical signal. Ideally the scintillation light created is linear with respect to the deposited energy, therefore the light yield maintains a proportionality with the deposited energy. Efficient light collection in combination with a linear response allows for good spectroscopy. The differences in performance between organic and inorganic materials is generally dependent upon the efficiency in converting the interaction energy scintillation light, the decay time of the excited atoms or molecules, and the Z-dependent cross-section of interaction. With respect to light collection, the statistical broadening of the response function is minimized with better light collection, thus improving the energy resolution. Other factors, e.g.,the uniformity in light collection efficiency as a function of interaction position within the scintillator material and non-proportionality also affect the energy resolution of the detector.

Common inorganic scintillator materials include sodium iodide, cesium iodide, and bismuth germanate. These scintillators generally have a higher stopping power and higher efficiency, and therefore better energy resolution and sensitivity, but often a slower de-excitation time in comparison to organic scintillators. Although organic scintillators, typically in plastic or liquid form, have a low Z, this is advantageous when used as a Compton scatter plane (see Quantum Optics section below) or as an anti-coincidence shield for reducing background

events. The fast response of organic scintillators, which can be on the order of a few nanoseconds, allows time-of-flight measurements as well as pulse shape discrimination, i.e. the ability to distinguish between different particle interactions based upon their respective decay times.

In addition to the above performance parameters, the scintillating medium also needs to be transparent to the wavelengths of de-excitation photons and, in the case of photomultiplier tubes, have a refractive index that allows for easy coupling to the light collecting instrument. The number of generated photoelectrons, or electron-hole pairs in the case of photodiodes, generated per incident scintillation photon, i.e. the quantum efficiency of the collecting device, is also important to allow for good statistics.

2.2.3 Semiconductor Detectors

In semiconductor detectors an incident photon transfers some of its energy in the detector resulting in the generation of electron-hole pairs within the crystal. The simplest description of a semiconductor detector is that of an ideal planar detector, whereby a potential difference is applied to a single cathode and single anode on opposite sides of a slab of semiconductor material. The resulting electrical field across the detector causes the charge carriers to drift towards their respective electrodes. Initially, the net charge induced on the electrodes is zero from the equal amount of electrons and holes located at the interaction site. As the charge carriers drift and separate, an increasing signal appears as a function of the increasing separation distance between the electrons and holes. In the ideal case, all of the charge carriers are collected, thus the total collected charge is proportional to the energy of the incident photon, allowing for good spectroscopy. In reality, effects such as charge carrier trapping or recombination, material non-uniformities, etc., can affect this proportionality relationship. These drawbacks and solutions are discussed in the next chapter for the case of CdZnTe. More information about semiconductor detectors can be found in *Spieler* (2005).

A primary advantage of semiconductors over scintillation detectors is that the number of electron-hole pairs produced in semiconductors exceeds the amount of photoelectrons produced in scintillators from an equivalent incident photon energy. This is advantageous as it greatly increases the charge carrier statistics thus allowing for very good energy resolution, e.g., typically $\sim$0.2% for a coaxial commercially-produced germanium detector, as compared to $\sim$6% for a single element sodium iodide detector at 662 keV, for example.

2.3 Principles of Imaging

In addition to spectroscopic information, several techniques can be used to obtain spatial information about a source by determining the arrival direction of the incoming gamma rays. Spatial distribution and localization, i.e. imaging, can either be obtained directly by reconstructing each photon interaction, or indirectly by using an accumulation of photon interactions to infer the source position. Whether gamma-ray interactions are better described by the wave aspect or the particle aspect of light depends upon the frequency of

radiation and the experimental arrangement. Below is a brief description of the methods used to image photons in the hard x-ray to medium-energy gamma-ray band, i.e. from tens of keV to a few MeV.

2.3.1 Geometrical Optics

Geometrical optics depends upon complete absorption of photons either within the detector material or within a passive material surrounding the detector. In this case a particle description of light is most appropriate, as the diffraction and interference effects are too small to see. Geometrical optics is an indirect form of imaging, as the reconstructed image relies upon the accumulation of photons in order to reconstruct the source location. These instruments utilize either spatial modulation such as pinhole cameras or coded aperture imagers, or temporal modulation, such as scanning collimators and rotating modulation collimators. For astrophysical telescopes, occultation from an astrophysical body, such as the Earth, is an example of a temporal modulation imager. Instruments that rely upon geometrical optics are optimal within the energy range where photoelectric absorption is the dominant interaction.

As a relevant example of geometrical optics, the concept of coded-aperture imaging is illustrated in Fig. 2.5. A coded mask consists of an array of pixels that are either filled with an absorbing medium or left empty. The pattern of the mask and the proportion of full to empty pixels varies depending upon the application. The mask array is placed in front of a position sensitive detection plane. Gamma rays from a far-field source are incident upon the coded aperture and, ideally, either pass through the holes in the mask or are absorbed by the pixels of the mask, creating a shadow pattern of the mask upon the back detection plane.

2.3.2 Quantum Optics

Imaging through quantum optics utilizes single photon interactions for localization. For medium-energy gamma-ray imaging, the Compton telescope, or Compton camera, is an example of a quantum optics imager, whereby incoherent scattering is used to reconstruct the position of the gamma-ray source. An incoming photon scatters within the detector material, depositing energy at each position of interaction. The sum of deposited energies yields the initial photon energy. The Compton formula, Eq. 5.2 is then used to calculate the scatter angle of the incoming photon. The resulting cone narrows the possible locations of the emission source to a projected event circle on the sky (*Schönfelder et al.*, 2001). If the direction of the recoil electron is also known, the possible location of the emission source can be further narrowed down, reducing the event circle to an arc. By accumulating multiple Compton events, the Compton circles or arcs begin to overlap, revealing the most probable location of the source. This method is illustrated in Fig. 2.6.

Figure 2.5: Illustration of the coded-aperture technique. A far-field source of radioactive emission casts a shadow of the mask pattern onto a focal plane. The resulting pattern can be used to identify the location of the source.

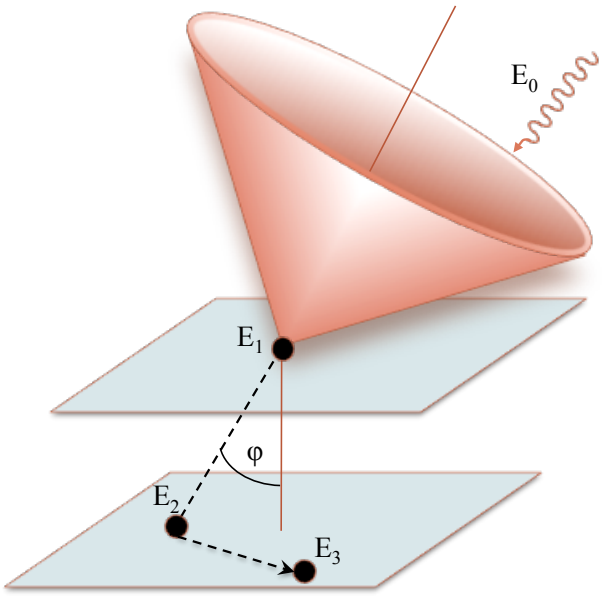

Figure 2.6: Illustration of the Compton imaging technique. Using energy deposit information, the incident scatter angle and initial photon energy are calculated. The direction of the incoming photon lies along the projected cone defined by the scatter angle. Overlapping cones reveal the most probable source location.

2.3.3 Wave Optics

Coherent scattering, such as Bragg diffraction (*Lund*, 2005) or Delbrück scattering (*Habs*, 2012), as well as refraction (*Skinner*, 2001) can be used to focus a beam of gamma rays onto a detection focal plane. In these cases the wave description of gamma rays is most applicable. Examples of wave optics instruments are Laue Lenses and Fresnel lenses. In wave optics instruments, the focusing plane can be decoupled from a much smaller collecting plane. This leads to a reduction of the intrinsic background, allowing for an improved signal-to-noise ratio and thus a greatly improved sensitivity.

In the case of coherent scattering via Laue lenses, the optical plane is made up of a large number of crystals in either an Archimedean spiral or in concentric rings to deviate the incoming beam and focus it onto a collecting area. The focal length depends on both the energy of the incoming beam and the diffractive properties of the optical plane. The bandwidth of the lens is roughly proportional to the number of crystals used. Although focusing much higher energies is theoretically possible, crystal studies are currently underway with the goal of developing a Laue lens for energies from 100 keV to 1 MeV at a focal length of 30 m (*Barrière*, 2014).

Because the refractive index of gamma-rays in matter is less than one, it is theoretically possible to use a conventional method, Fresnel lensing, to focus incoming beams of gamma radiation onto a detection plane. In this case, no special optics are required and an angular resolution of μarc seconds, very high efficiency, and true imaging are achievable. However for space applications, a very large collecting plane is needed to provide a reasonable field-of-view, and a long separation distance is required between the two planes (on the order of 10^9 m in the medium-energy band). This would require the launch and synchronization of two separate spacecraft. Despite the elegance of the method, the implementation of a Fresnel lensing telescope is very challenging.

2.4 Imaging Instrumentation

Because this work is motivated by both astrophysics and terrestrial applications, the most relevant examples in terms of history, detection and imaging goals, imaging techniques, and/or detector type in both domains are presented in this section.

2.4.1 Astrophysics Instruments

All but showers from the most energetic gamma rays are stopped in the Earth's atmosphere, therefore observations of astrophysical sources must be performed from balloon altitudes (40 km) or from space. In addition to the operational challenges and payload restrictions of space operation, the biggest challenges for gamma-ray telescopes is the presence of numerous components of background (e.g., cosmic rays, Earth's albedo emission,particles trapped in the Earth's radiation belts, activation within the detector and surrounding material,) as well as the scarcity of gamma rays from sources. This requires telescopes to have good

energy resolution to improve the signal to noise ratio, good angular resolution to locate sources, and the ability to discriminate against background to allow for high sensitivity in this energy regime. Three of several successful missions are described below.

2.4.1.1 COMPTEL

COMPTEL, launched aboard the Compton Gamma-Ray Observatory (CGRO) in 1991, was the first Compton telescope in space (*Schönfelder et al.*, 1993). COMPTEL consisted of two detection planes separated by a distance of 1.5 m: a top scatter plane of low Z liquid scintillator detectors and a back absorber plane of high Z sodium iodide detectors. The fast response of the scintillator detectors in combination with the separation distance between the two planes allowed for a time-of-flight measurement in order to group single detector hits into Compton events as well as allowing for rejection of upward-moving photons from the Earth's atmosphere. COMPTEL had an observable energy range from 0.8 to 30 MeV with an energy resolution of 5 - 10 % FWHM, and an angular resolution of 1.7° - 4.4° FWHM within its 1 steradian field-of-view. COMPTEL operated until 2000. Its successes include detection of several supernovae, e.g., SN 1991T, remnants from Cas A and Vela, and the generation of all-sky maps from 1 to 30 MeV. Most notably, the first all-sky map at 1.8 MeV (*Oberlack*, 1996) from COMPTEL illuminated the correlation between the ^{26}Al line at 1.8 MeV and the location of massive stars along the Galactic plane.

2.4.1.2 Integral/SPI

The SPI (SPectrometer on INTEGRAL) onboard the INTEGRAL (INTErnational Gamma-Ray Astrophysics Laboratory) spacecraft (*Vedrenne*, 2003) is a high spectral resolution telescope using spatial modulation to detect and localize sources within the energy range of 18 keV to 8 MeV. INTEGRAL launched in October 2002 and is currently (2014) still in operation. It uses a passive coded-mask imager in front of a plane of 19 high purity germanium detectors, providing an energy resolution of 2 to 8 keV FWHM (2.5 keV at 1.3 MeV FWHM) and an angular resolution of 2.5° over a fully coded field of view of 16° and a partially coded field-of-view of 31°. A bismuth germanate anti-coincidence shield reduces the germanium detector background by a factor of 20.

The science goals of SPI are to explore stellar nucleosynthesis using line spectroscopy and imaging, to study the physics of compact objects such as neutron stars, pulsars, or black holes in binary systems, Active Galactic Nuclei (AGN) and gamma-ray bursts. Highlighted results from SPI include a spectrum of the Crab nebula, image of the Galactic plane, observations of numerous GRBs, AGNs, and x-ray binaries, and Galactic all-sky map of the 511 keV positron annihilation line (*Bouchet*, 2010).

2.4.1.3 COSI/NCT

The Compton Spectrometer and Imager (COSI) instrument (an upgraded version of NCT, the Nuclear Compton Telescope) is a balloon-borne instrument that utilizes 12 high-purity

germanium (HPGe) double-sided strip detectors arranged as a compact Compton telescope to allow for 3D imaging [1]. The science goals of COSI include the study of astrophysical nuclear line sources and gamma-ray polarization. The instrument is sensitive to line emissions from 0.5 to 2 MeV, with an energy resolution of ∼.8% at 1173 keV, and to polarization from 0.2 to 0.5 MeV over a field-of-view of 25% of the sky. Compton imaging in combination with active shielding and new analysis techniques will very effectively reduce the background.

The 2009 flight of NCT resulted in the first gamma-ray image of the Crab Nebula using a compact Compton telescope. Following a 9 hour observation, the Crab nebula was detected at a significance level of 4σ (*Bandstra*, 2011).

2.4.2 Environmental and Nuclear Security Applications

2.4.2.1 TriModal Imager

The Standoff Radiation Detection System (SORDS) TriModal Imager (TMI) is a vehicle-mounted gamma-ray imager developed to identify and localize gamma-ray emitting threat sources at 100 m standoff distances from a ground-based, moving platform (*Wakeford*, 2009). The instrument consists of 2 arrays of sodium iodide (NaI) detectors that are arranged to allow for both Compton imaging and coded aperture imaging, with a front plane of 35 NaI detectors serving as both the Compton scatter plane and an active coded mask. The 30 position sensitive detectors in the back plane have an average position resolution of ∼3.8 cm. The average energy resolution for all 65 detectors is 6.75% FWHM at 662 keV. The third mode is shadow detection, a non-imaging diagnostic that can reveal the presence of a source by the shadow cast on the detectors within the moving field-of-view (*Hynes*, 2009). One of the main challenges of a system such as TMI is the detection of a source from a moving platform, thus detection and imaging sensitivity is subject to a natural and geographically variable incident background.

2.4.2.2 Astro-H Soft Gamma-ray Detector prototype

Following the Fukushima Daiichi nuclear accident, a scaled-down version of the Astro-H Soft Gamma-ray Detector (SGD) telescope (*Tajima*, 2010) was used to reveal concentrated areas of contamination within the Fukushima prefecture. The SGD is configured with a collimator above 32 layers of double-sided silicon strip detector scatter planes and 8 layers of ambient-temperature operation Cadmium Telluride (CdTe) detectors as absorber planes. The scaled-down version used 2 layers of a silicon double-sided strip detectors above 3 layers of CdTe detectors. In this version the collimators were removed, providing a 180° field-of-view. The instrument had a 2.2% FWHM energy resolution at 662 keV and an angular resolution of 3.8° FWHM at 662 keV [2]. Ground-based measurements with the uncollimated, scaled-down version of the Astro-H SGD prototype successfully demonstrated Compton backprojection

[1] http://hea.ssl.berkeley.edu/research/cosi/

[2] http://www.astro.isas.jaxa.jp/ takeda

imaging of a 30 μSv/hr ^{134}Cs plus ^{137}Cs hotspot above a 3 μSv/hr background at a significance of 3σ. Based on the successful demonstration of this instrument, a portable imager, the Astrocam-7000HS, has been developed and is being commercially produced.

2.4.2.3 The High Efficiency Multimode Imager

The High Efficiency Multimode Imager, HEMI, is a combined Compton and coded-mask imager that was developed in as a prototype for the purpose of nuclear threat detection. It utilizes large-volume Cadmium Zinc Telluride detectors as serving as both an active coded mask (32 detectors in an optimized random mask pattern) and a Compton scatter plane, and an array of 64 CdZnTe detectors as an absorbing backplane. The advantages of a HEMI design include a high efficiency as well as low mass, low power consumption, and simplified electronics because of the large volume (1 cm^3) CdZnTe detectors. As will be described in this work, the HEMI instrument has an energy resolution of 2.4% FWHM at 662 keV, a 9.5° angular resolution in Compton mode, and an 11° angular resolution in coded-mask mode. Imaging capabilities in both modes were demonstrated. After successful benchmarking, the HEMI detectors were simulated for use in an Advanced Compton Telescope design and showed a reasonable sensitivity for medium-energy gamma-ray astrophysics. Additionally, the low mass and low power consumption allowed for mounting and operation of the HEMI prototype instrument from an aerial platform. The instrument was successfully commissioned through field tests in the Fukushima prefecture at 10 - 20 meter altitudes in August of 2013.

2.5 Summary

Detection and imaging of gamma rays can be accomplished using technologies developed to exploit photoelectric absorption and Compton interactions within a medium. The evolution of detector technologies, for example from the large scintillation detectors used in COMPTEL to the finely pixelated semiconductor detectors of COSI/NCT, allowed for large improvements in energy resolution, position resolution, and therefore angular resolution, e.g., 1-2 orders of magnitude over just a few decades. The latest generation of imagers can be compact in design, have high efficiency, and are capable of achieving very good sensitivity. The applications of these instruments, e.g., nuclear security, astrophysics, environmental monitoring, medical imaging, etc., are complementary to one another, thus technological development can be mutually beneficial across fields.

Chapter 3

The High Efficiency Multimode Imager

The High Efficiency Multimode Imager, HEMI, was developed as a prototype instrument with the goal of demonstrating characterization and imaging of gamma-ray sources. The HEMI concept is illustrated in Fig. 3.1. It uses a two-planar configuration of detectors for both Compton imaging and coded aperture imaging. The top plane consists of active detectors and therefore serves as both the Compton scatter plane and the mask absorption plane, thus allowing for a higher geometric efficiency as compared to an imager with a passive mask. The HEMI detector arrays consist of cubic centimeter Cadmium Zinc Telluride (CdZnTe) semiconductor detectors with good energy resolution ($\sim$2% at 662 keV FWHM).

The HEMI program was initiated as a research and development project under the United States Department of Homeland Security and Domestic Nuclear Detection Office. A need exists for an instrument with enhanced abilities to detect and localize weak sources at a distance and to discriminate between threat and non-threat sources. The prototype was designed to be modular so that upon successful demonstration of its spectroscopic and imaging capabilities, the system can easily be scaled to larger areas as required for standoff detection of nuclear threat sources.

In order to build and test the capabilities of the prototype instrument it was necessary to fabricate CdZnTe detectors with good spectral performance (*Amman*, 2009). Additional hardware, software, and a data analysis pipeline were also developed specifically for the HEMI project (HEMI Final Report, *Amman, 2013* and *Zoglauer*, 2009). This chapter gives an overview of the HEMI instrument and describes the essential hardware components and data acquisition software developed for the HEMI prototype.

3.1 Instrument Overview

The HEMI prototype instrument is shown in Fig. 3.2. The detectors are arranged in two planes that are separated by 7.5 cm. The motherboard for each detector plane allows for

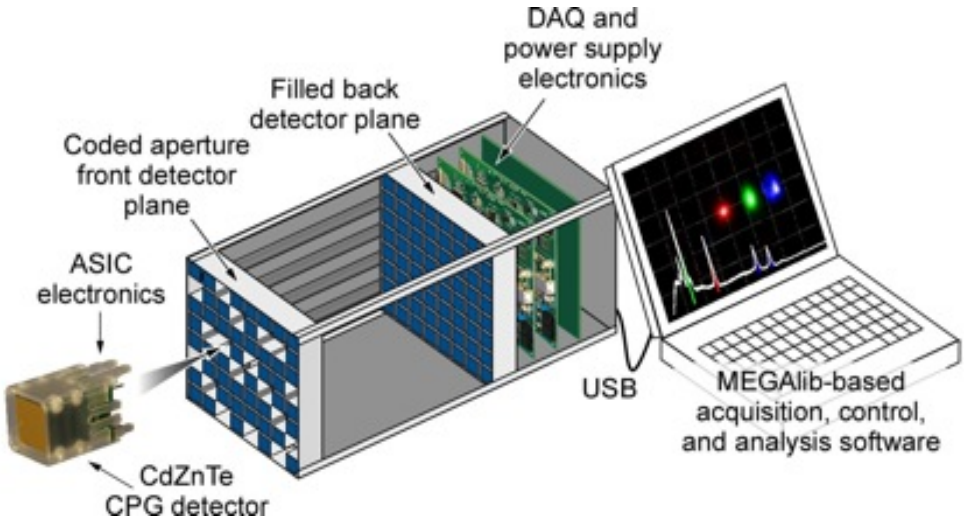

Figure 3.1: Concept of one possible configuration of a HEMI instrument. Two planes of CdZnTe detectors (blue) allow for both Compton imaging and coded aperture imaging using an active coded mask.

8 x 8 detector channels. The top plane consists of 32 detectors (50% filled) arranged in an optimized random mask pattern. The bottom plane is fully filled with (nominally) 64 detectors. The instrument hardware allows for adjustments to the separation distance between the two detection planes. The overall system is compact (15 cm x 15 cm x 20 cm) and lightweight (∼2 kg), thus allowing for portability and a relatively simple transition to the field for testing.

The detector elements are cubic centimeter CdZnTe semiconductor crystals. The large voxel size as compared to pixellated detectors, for example, is limiting in terms of position resolution but advantageous in that it greatly minimizes the required electronics. This allows for simplicity in design and operation as well as very low power consumption. The entire system consumes approximately 8 watts, which can easily be supported by battery power in portable applications.

Each individual detector element is packaged with an ASIC (described in Section 3.1) and mounted using silicone within a modular lexan container as shown in Fig. 3.2, left. The detector elements are installed in the motherboard via the flexible extensions on the bottom of the lexan casing. This fastener-free design is advantageous in that it limits the amount of scattering or absorbing material surrounding the sensitive detector volume as well as allowing for a compact configuration, ideal for a Compton imager. The containers snap into and out of the motherboard, providing ease in removing or replacing detectors and in reconfiguring the mask pattern while still providing secure electrical and mechanical connections.

The two detector array motherboards are connected via flexible cables to two data acquisition (DAQ) boards and a regulated high voltage and power supply (HVPS) board. The DAQ and HVPS boards are contained within the HEMI enclosure in a separate compartment

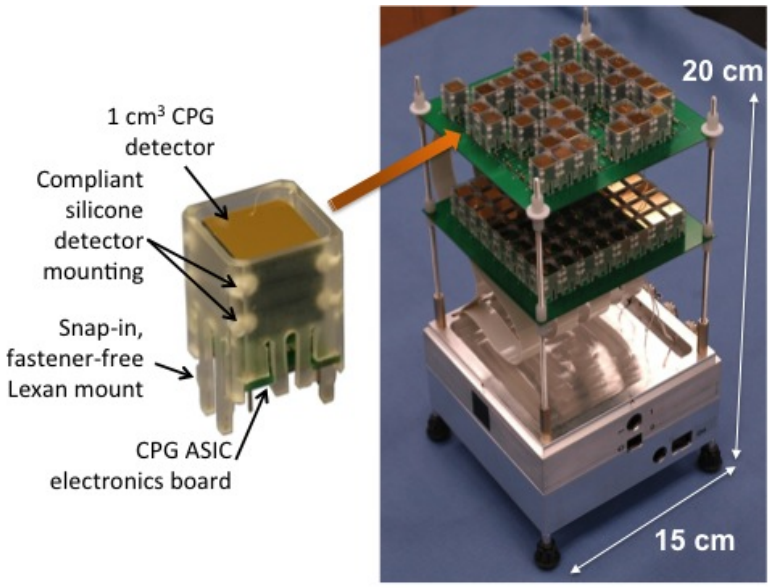

Figure 3.2: Left, the CdZnTe detector element with ASIC in Lexan housing. Right, the 96-detector HEMI prototype instrument.

below the array as illustrated in Fig. 3.1. The HVPS boards supply low-voltage power (2.5 V) to the CdZnTe ASIC and the high voltage for the grid (-80 V) and cathode (1000 V) biases. The DAQ boards take the analog shaped signals from each detector and convert it into digital data. After analog to digital conversion, the signals from the DAQ board are routed to a computer using quick USB connections.

The analysis software for HEMI consists of two main components: HEMI DAQ which handles instrument controls, data acquisition, storage, routing, and some initial data processing, and the Medium Energy Gamma-ray Astronomy library software package, MEGAlib, (*Zoglauer*, 2006) which allows for real-time or offline data analysis, event reconstruction, and imaging.

3.2 Cadmium Zinc Telluride Detectors

At the heart of the HEMI instrument are the 1 cubic centimeter coplanar-grid (CPG) Cadmium Zinc Telluride (CdZnTe) semiconductor detectors (*Luke*, 1995, 1996, 1997, *Amman and Luke*, 1999). CdZnTe detectors have the advantages of room temperature operation, good energy resolution, near full-volume efficiency, a wide band-gap, and commercial availability. Information regarding the growth and development of CdZnTe material can be found in *Amman* (2009). Details regarding the achievable energy resolutions and the long-term stability of the detectors can be found in *Luke* (2004) and *Amman* (2006).

Fabrication and testing of commercially produced CdZnTe detectors for HEMI was

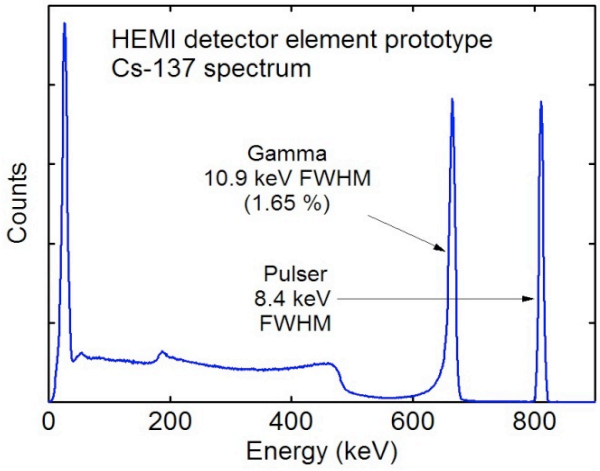

Figure 3.3: Energy spectrum of one of HEMI's highest quality CdZnTe detectors with respect to energy resolution: 1.65% FWHM at 662 keV.

established by Redlen Technologies in collaboration with Lawrence Berkeley National Laboratory. The target energy resolution for production was 2% FWHM at 662 keV. By adjusting the material selection procedures as well as the coplanar grid fabrication process, the Redlen detectors showed an improved spectral performance by the end of the production phase. Fig. 3.3 shows an energy spectrum from one of the better detectors with a 1.65% energy resolution at 662 keV.

3.2.1 Comparison with High Purity Germanium Detectors

Because high-purity germanium (HPGe) detectors are considered state-of-the-art for gamma-ray detection and spectroscopy, alternative detector technologies should have comparable performance (e.g., energy resolution, response time, efficiency, etc.) or other significant advantages in order to justify their development and implementation. To this effect, Table 3.1 shows a comparison between (HPGe) detectors and the HEMI CdZnTe detectors as fabricated by eV Products.

The primary advantage of CdZnTe as a detector material is its ambient-temperature operation therefore requiring only moderate or no cooling, whereas HPGE requires cooling to about 77 K. This is advantageous in that it simplifies detector design, reduces power requirements, and also minimizes the amount of surrounding material that can scatter or absorb and become activated by incident radiation. The latter is of particular concern for applications with high incident background, such as for space telescopes.

The need for cooling of HPGe is a result of its small bandgap, as seen in Table 3.1. The small bandgap leads to a significant number of charge carriers being thermally generated, thus creating leakage current and the need for cooling to 77 K. However, the small bandgap is advantageous in that for a deposited photon energy, more electron-hole pairs are generated

	HPGe (77 K)	CdZnTe
Average Atomic Number	32	49
Band Gap (eV)	0.74	1.50
W: Energy per electron-hole pair (eV)	2.96	4.4
Electron Mobility-Lifetime $\mu_e\tau_e$ (cm^2/V)	3.6x10^1	9.9x10^{-3}
Hole Mobility-Lifetime $\mu_h\tau_h$ (cm^2/V)	4.2x10^1	8.3x10^{-4}

Table 3.1: Comparison between high-purity germanium (HPGe) and Cadmium Zinc Telluride (CdZnTe). The values for CdZnTe are based on detectors fabricated by eV Products. (HPGe: *Bertolini*, 1968, CdZnTe: *Cho*, 2011)

in HPGe than in CdZnTe. This is reflected in the W-factor: the average energy required to generate an electron-hole pair. The increase in the number of charge carrier statistics per average deposited energy leads to less broadening in the photopeak, and thus the superior energy resolution of HPGe. From statistical broadening, the achievable energy resolution of a commercially-produced coaxial HPGe detector is, e.g., <0.2% FWHM at 1.33 MeV.[1]

Although the lower charge carrier statistics limit the achievable energy resolution of CdZnTe, the main drawback of CdZnTe as a detector material is its extremely low mobility-lifetime ($\mu\tau$) product of holes. As a result, the holes cannot be collected in any reasonable time frame. The incomplete charge collection of holes implies that the holes remain within the bulk of the detector over the collection time of the electrons and induce charge on the collecting anode, subsequently reducing the signal from the collected electrons. In contrast, the high $\mu\tau$ product for both electrons and holes in HPGe offers a significant advantage over CdZnTe, particularly in terms of spectroscopy. This eliminates the need to compensate for induced charges. Additionally, the collection of both charge carriers provides better statistics. To overcome the fundamental limitation of the low $\mu\tau$ product of holes in CdZnTe, the coplanar grid technique is applied (*Luke*, 1995) as described in the following section.

3.2.2 Coplanar Grid Technique

In order to obtain good spectroscopy with a gamma-ray detector, it is necessary to preserve the proportional relationship between the energy deposited from an incoming photon interaction within the detector material and the total collected charge resulting in a measured signal from this interaction. To collect the charge carriers a bias voltage is applied across the detector, causing electrons and holes to separate and drift to their respective electrodes. In the case of perfect charge collection, the final induced charge at the electrodes is equal to the generated charge, and therefore the original deposited photon energy can be deduced and good spectroscopy can be achieved.

[1] http://www.ortec-online.com

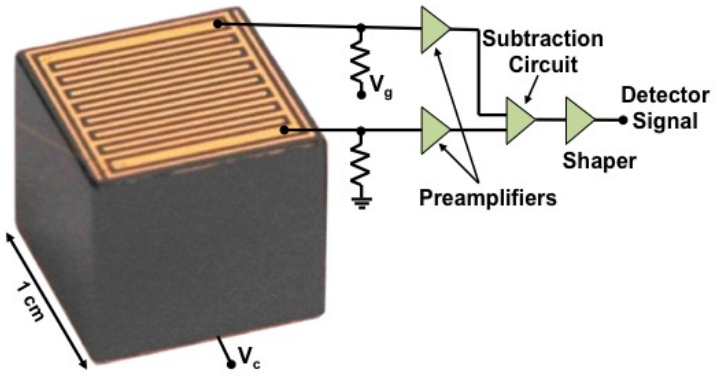

Figure 3.4: Coplanar grid detector showing the interdigitated grid electrodes and the front-end electronics schematic.

However, in the case where the holes drift significantly more slowly than the electrons, the total induced charge on the anode after electron collection is reduced by the induced charge from holes that remain within the bulk of the detector material. The induced charge on the anode is proportional to the distance from the anode to stationary holes. Because the holes are effectively stationary throughout the collection time of the electrons, the final induced charge, to first order, maps linearly to the distance of interaction from the collecting electrode. Consequently, the induced charge is no longer proportional to the deposited photon energy and is dependent upon the depth of interaction, resulting in degraded spectroscopy. This is particularly true for large-volume CdZnTe detectors.

In order to compensate for the depth-dependent induced charge of the uncollected holes, the coplanar grid technique was developed and optimized for CdZnTe detectors (*Luke*, 1994, 1995, 1996, *Amman and Luke*, 1999). Fig. 3.4 shows the two interdigitated grid electrodes of the CdZnTe detector: a collecting and a non-collecting grid. A bias voltage (nominally -80 V) is applied between these electrodes to force the electron collection to only the collecting grid. Because the hole motion is minimal within the collection time of the electrons, the holes remain within the bulk of the detector at the time of electron collection and induce approximately the same amount of depth-dependent charge on both of the grid anodes. Having two grid electrodes that equally share the hole charge allows for a differential measurement. By subtracting the charge of the non-collecting grid from the collecting grid, the induced hole charge is eliminated and the final induced charge maintains a consistent, proportional relationship to the number of generated charge carriers, assuming the case where there is no electron trapping. This is shown in Eq. 3.1, where Q_{cg} and Q_{ncg} are the total induced charges on the collecting grid and non-collecting grid, respectively, and Q_e is the total collected electron charge after subtraction.

$$Q_e = Q_{cg} - Q_{ncg} \tag{3.1}$$

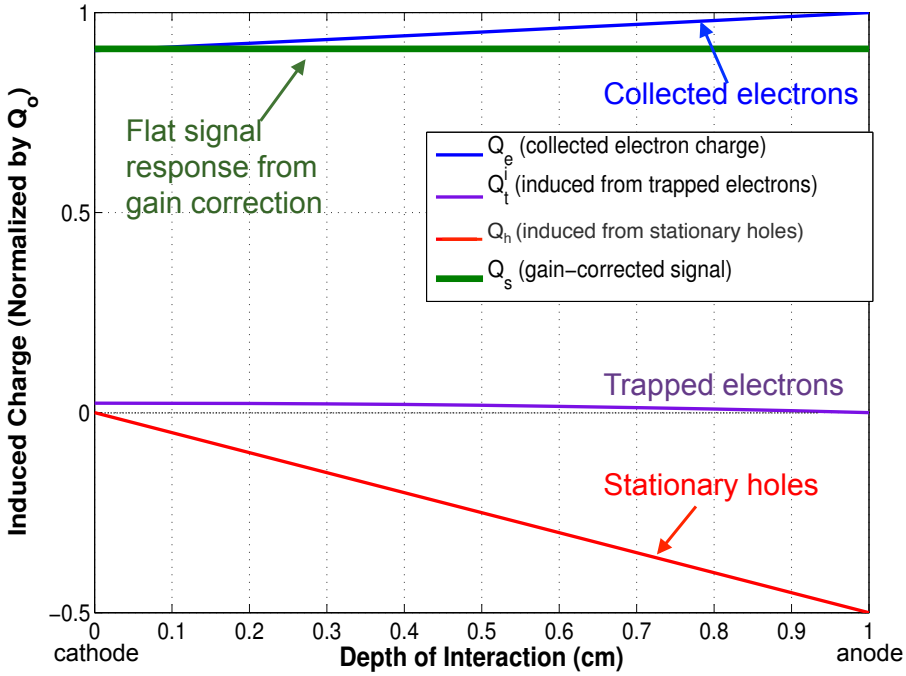

Figure 3.5: The induced charge as a function of depth of interaction within the detector. The green line represents the gain-corrected, depth-independent measured signal.

3.2.3 Differential Gain Adjustment

In addition to low hole mobility, the other main drawback of CdZnTe is charge trapping within the bulk of the detector due to material defects and impurities. The amount of charge carrier trapping is dependent upon the depth of interaction, as the farther the charges need to travel to reach the anode or cathode, the more likely that the charge carriers will become trapped between the interaction site and the electrodes. The holes are relatively immobile, and their induced charge is accounted for using CPG electrodes. However, the depth-dependent charge loss from electron trapping requires a different method. Electron trapping can be compensated for by using a depth of interaction method (*He*, 1996) or by applying an optimized differential gain adjustment to the non-collecting grid electrode (*Amman, private conversation*). The latter technique is used for the HEMI CdZnTe detectors.

The induced charge on the anodes as a function of depth of interaction is shown in Fig 3.5 for trapped electrons, Q_t^i, and trapped holes, Q_h. After correcting for trapped holes through the CPG method, one can still see the effect of charge induction from trapped electrons on the collected electron charge, i.e. Q_e, which varies as a function of depth of interaction. A total induced charge of Q_o implies complete collection of the free charge carriers created from the initial photon interaction.

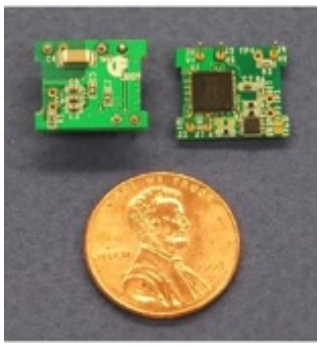

Figure 3.6: Individual detector circuit board containing the front-end electronics including the coplanar grid ASIC.

In order to compensate for the trapped electron charge, the differential gain method reintroduces some of the depth-dependent induced charge of the stationary holes. This is done by applying a gain value, G < 1, to the induced charge of the non-collecting grid, effectively altering the slope of the collected electron charge. This is described by Eq. 3.2, where Q_s is the measured charge after gain correction.

$$Q_s = Q_{cg} - GQ_{ncg} \tag{3.2}$$

One can see from Fig 3.5 that the gain-corrected signal, Q_s, is no longer a function of the depth of interaction, albeit at a value slightly less than complete charge collection, i.e. $Q_o = 1$. This method is effective under the assumption that there are no significant spatial non-uniformities in the detector material.

For each of the HEMI CPG detector elements the gain is applied empirically by adjusting a digital potentiometer to optimize the FWHM, nominally at 662 keV. The optimal resistance setting is written to a non-volatile memory, allowing for a one-time setting of the gain value.

3.3 Electronics and Data Acquisition

3.3.1 Readout Electronics

The CdZnTe detector element with the interdigitated grid anodes and a schematic of the front-end and shaping electronics are shown in Fig. 3.4. The individual electronics boards that are mounted with each detector, shown in Fig. 3.6, include the coplanar grid ASIC (*De Geronimo*, 2006) and related components, a compact digital potentiometer to adjust the differential gain, and passive high-voltage filters for the cathode and grid applied bias voltages. The CPG subtraction circuit, preamplifier, and shaping electronics are contained on each CPG ASIC and were developed by Lawrence Berkeley National Laboratory.

The shaped signals from each detector are routed to the main data acquisition boards. A block diagram of the data acquisition board and readout electronics is shown in 3.7.

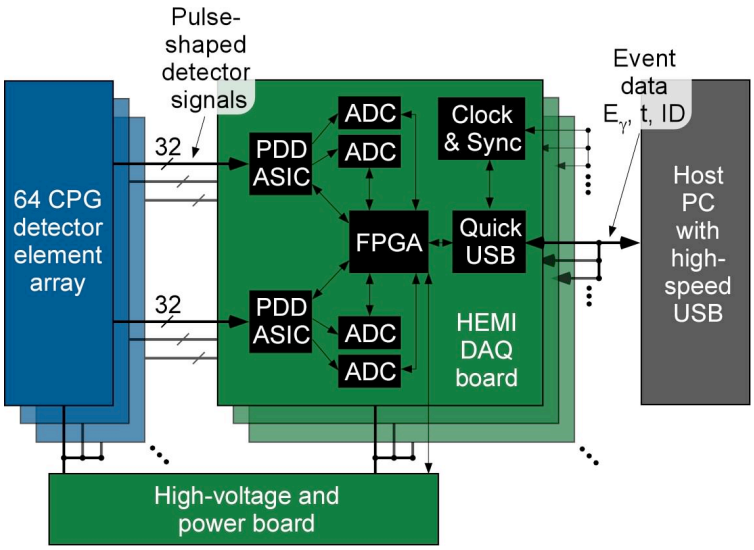

Figure 3.7: Block diagram of the data acquisition and signal readout electronics. Pre-shaped pulses from each detector are readout by the PDD ASIC and converted to a digital signal. The signals are buffered and timestamped, then the event data is routed to a host PC via Quick USB.

Each data acquisition board is capable of reading out 64 detectors. The boards include a peak detect derandomizer (PDD) ASIC (*O' Conner*, 2003), a 16-bit ADC, an FPGA, and a QuickUSB module. The PDD ASIC and ADC convert the analog pre-shaped pulses into digital event data, namely detector ID, time, and ADC channel. The FPGA timestamps and buffers the data. The events are then routed via USB to the HEMI DAQ software application, described in the analysis software section of this chapter.

The DAQ board has a low power consumption (about 1.3 Watts) and has an approximate event handling rate of 500,000 events/s, although this limit has never been tested. The board is capable of making high resolution spectroscopic measurements, as demonstrated with a ^{133}Ba source measured by a single strip on a Germanium detector, shown in Fig. 3.8. However, the DAQ has a few drawbacks for the HEMI application. The board does not perform baseline restoration, as a consequence the energy resolution becomes degraded at high count rates. Additionally, issues regarding the noise threshold are described in the following section.

3.3.1.1 Noise Threshold

The PDD ASIC (*De Geronimo*, 2006) that is used with the HEMI detectors are non-ideal for this application as they were originally designed for fast signals. A typical CPG detector has a shaping time on the order of a few microseconds, creating pre-shaped pulses with more of a Gaussian shape rather than a fast pulse which has a very steep leading edge. As a

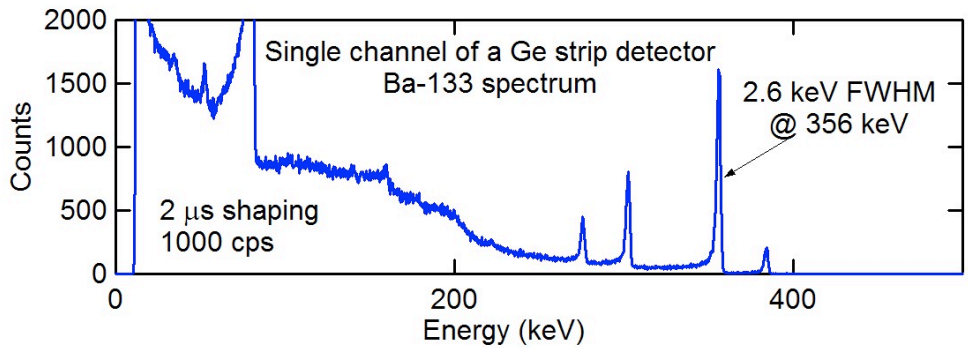

Figure 3.8: Spectra acquired with the HEMI DAQ board measured by a single strip on a Germanium detector. An energy resolution of 0.73% FWHM at 356 keV was achieved (*courtesy of Amman*, 2014).

result, noise fluctuations in the shaped pulses of the HEMI detectors can oscillate around the threshold energy, signaling to the ASIC that the maximum amplitude of the pulse has already been acquired. As a result, the readout of the full pulse height is interrupted and the initial triggered hit is interpreted by the DAQ as a very low amplitude pulse, i.e., a hit near the threshold energy. After AD conversion, these falsely triggered events accumulate and create a peak in the lowest bins of the ADC spectrum.

In addition to this effect, the threshold setting in the ASIC can only be tuned in discrete, coarse steps (on the order of 15 keV). As a result, photons with energies between the allowable set threshold energies and the true noise floor of the detector are not detected, ultimately limiting the energy range and particularly the Compton efficiency of the instrument. For these reasons, depending upon the application a more appropriate ASIC design will be needed for future CPG-based, HEMI-like instruments.

3.3.1.2 Saturation Endpoint

Upon extending the measured energy range up to 4 MeV, one can see many sharp, high-energy peaks appear in the datasets. This effect can be attributed to signal saturation in the individual detectors. A high-energy charged particle, such as a cosmic-ray muon, can deposit an energy that saturates the ASIC. Because the gain settings vary from detector to detector, the saturated bin corresponds to different ADC values in the combined spectrum, resulting in an accumulation of counts at energies between 2.5 to 4 MeV. Therefore, a cutoff energy is approximated for each individual detector to eliminate the saturated bin. All energies greater than this cutoff value are removed from the measured datasets.

3.4 Data Acquisition Software

HEMI DAQ is a multithreaded LabWindows CVI based application that was developed for use with the HEMI prototype (HEMI final report, *Amman*, 2013). It serves as an interface to the instrument controls and handles the data acquisition tasks. The HEMI DAQ software also allows for real-time monitoring of detector functionality, an initial energy calibration, spectroscopy, and many other features.

HEMI DAQ stores the data in binary or ASCII form for offline processing using the Medium Energy Gamma-ray Astronomy library software package, MEGAlib. It is also capable of routing the data through a TCP/IP interface to the real-time imaging analysis package, Realta, contained in MEGAlib. MEGAlib and the additional data analysis software that was used by and developed for HEMI are described in the next chapter.

Chapter 4

Analysis Software

The Medium-Energy Gamma-ray Astronomy library, MEGAlib (*Zoglauer*, 2006), is the software package used for HEMI data analysis. MEGAlib is written in C++ and based on ROOT (*Brun et al.*, 1997). It is open source software that was designed for use with gamma-ray detectors and especially for imaging with Compton telescopes. The software tools in MEGAlib comprise the complete data analysis chain including data acquisition from measurement or simulation, calibration, application of measurement uncertainties to simulations, event reconstruction, and high level analysis such as image reconstruction, sensitivity calculations, and polarization analysis. It is adaptable to different instrument designs and detector types that operate within the hard X-ray to medium energy gamma-ray band (a few keV to hundreds of MeV).

For the HEMI project, MEGAlib was used primarily for characterizing the spectral response and angular resolution of the instrument as well as for performing both offline and real-time event reconstruction and imaging. Its SensitivityOptimizer and BackgroundMixer programs were used for the HEMI-based gamma-ray telescope described in Chapter 7. The simulation package contained in MEGAlib, Cosima, was used for all of the HEMI simulations. Additionally, spectral analysis and coded-aperture optimization and reconstruction tools were developed specifically for the HEMI project. An overview of the simulator and the relevant components of the MEGAlib package are described in this chapter. The spectral analyzer is described in more detail as it was developed specifically for the HEMI project. Additionally, a brief summary of the Compton and coded-mask event reconstruction and imaging as used in the HEMI project is given. Details on the application of these programs and specific methods used for the HEMI prototype instrument are described in the next chapter.

4.1 MEGAlib Software

The following programs are contained in the MEGAlib data analysis package and were used for the characterization, simulation, Compton event reconstruction, and Compton imaging.

The application of each of these programs to the HEMI prototype is explained in more detail in the next chapter.

4.1.1 Simulation Tool (Cosima)

Monte Carlo simulations are performed using Cosima (*Zoglauer*, 2009), the simulation toolkit contained in MEGAlib. An illustration of the simulation pipeline is shown in Fig. 4.1. First a realistic geometry is created using the Geomega package in MEGAlib. The geometry specifies the dimensions of each volume, the elemental composition, and density of all passive and active volumes within the detector and surrounding environment. The simulator imports the Geomega geometry and converts it into a Geant4 (*Agostinelli*, 2003) format. Cosima then uses the Geant4 geometry and source information in order to simulate the propagation of individual photons from the source followed by the interactions, e.g., photoabsorption, scattering, etc., that take place as the photons propagate through the materials as described in the geometric mass model. The resulting Cosima output file contains the simulated interaction information including the time, type, position, and energy deposition of each interaction.

4.1.2 Detector Effects Engine

The initial simulated event list is idealized, as it does not include information about the measurement uncertainties such as energy and position resolution, time noising, threshold cuts, etc. These uncertainties can be determined directly from the measurements through fitting methods and then added to the detector response parameters in the Geomega detector description. The idealized simulated data is then convolved with the response parameters using the MEGAlib detector effects engine to get an event list of time, energies, and positions that more accurately reflects the measured data. Through benchmarking the convolved simulation with measurements one can iteratively refine the detector response parameters until achieving an agreement between the two. This is a primary aspect of detector calibration and characterization.

4.1.3 Event Reconstruction (Revan)

Following the generation of simulated data or after acquiring and calibrating measured data, the individual detector hits are grouped by coincidence timing into Compton events using revan, the event reconstruction package in MEGAlib. The Revan tool uses Compton Sequence Reconstruction, CSR, (*Zoglauer*, 2005) in order to determine the sequence of each event, thus finding the initial photon energy and the most likely scattering angle of the incoming photon. In addition to CSR, revan also refines the likelihood of a particular sequence of events using photoabsorption and Klein-Nishina probabilities in conjunction with the materials as defined in the Geomega mass model.

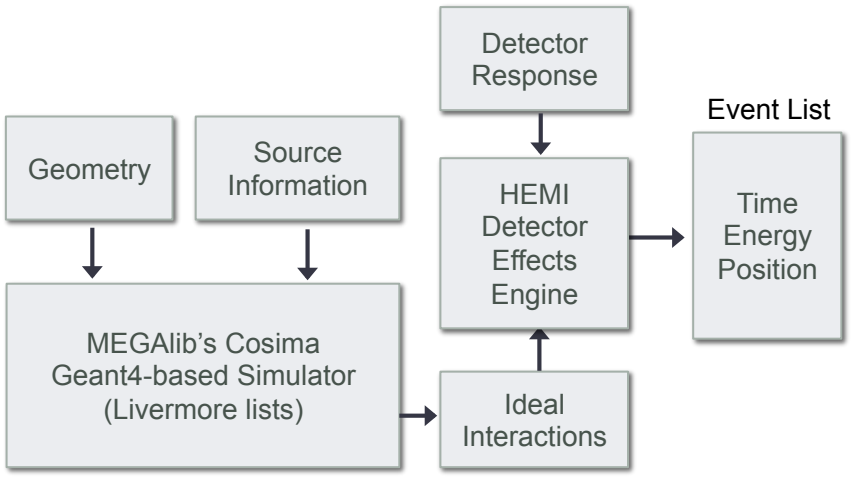

Figure 4.1: Diagram indicating the necessary components and processes that lead to the creation of simulated datasets.

4.1.4 Image Reconstruction (Mimrec)

This list of reconstructed events then undergo imaging and other high-level analysis (e.g., application of event cuts, estimation of angular resolution measurement (ARM), assessment of photon interaction locations and energies) using the Mimrec tool in MEGAlib (*Zoglauer*, 2011). Imaging algorithms are used to generate a Compton backprojected image within a user-specified coordinate system. Additionally, a List-Mode Maximum Likelihood Expectation Maximization (ML-EM) algorithm can be applied to further refine the image (*Wilderman*, 1998).

4.1.5 Real-time Imaging (Realta)

Realta, a real-time imaging analysis tool in MEGAlib, was modified and refined for use with the HEMI project (*Zoglauer*, 2011). Calibrated data is sent via a TCP/IP interface from the HEMI DAQ Windows-based operating system to Realta, which requires a Linux or Unix based system. Realta handles the complete data-analysis chain including reconstruction of Compton events based upon a predetermined coincidence time, event selections, image reconstruction, and isotope identification. The accumulation time, energy gate, and number of iterations of the image reconstruction MLEM algorithm are user-specified and can be adjusted in real time while imaging.

Fig 4.2 shows the graphic user interface for realta. The spectral analyzer (next section) was integrated into realta. The GUI shows the single detector hit summed spectrum in the top half with identified isotopes listed (in this case, the ^{133}Ba and ^{137}Cs lines). In general, once the isotopes of interest are determined from the spectra, an energy gate can be selected

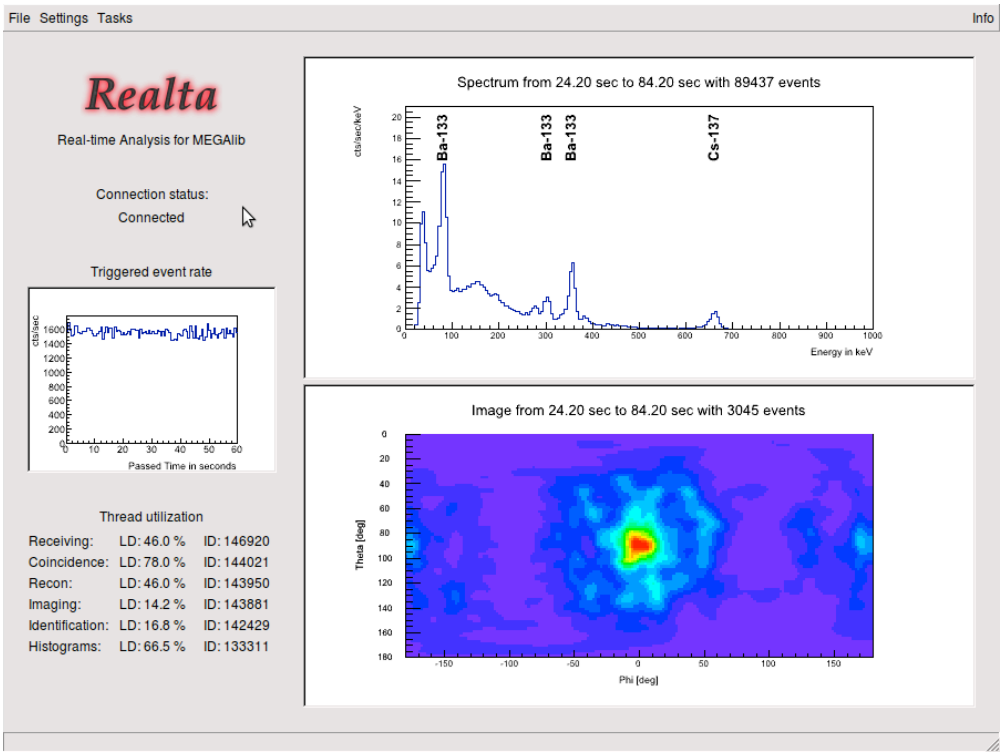

Figure 4.2: The graphical user interface of Realta showing an energy histogram of single detector hits with identified isotopes and a backprojected image produced in real time.

for imaging. The bottom half of the GUI shows a backprojected image of the isotopes after an accumulation time of 60 seconds (no energy gate was applied in this case).

4.2 Additional Software

4.2.1 Spectral Analyzer

A spectral analysis program was written specifically for the HEMI analysis (*Galloway*, 2010). The spectrum analyzer (referred to as "Spectralyzer" in MEGAlib) is used for peak searching, background estimation, peak characterization, and isotope matching to satisfy the spectroscopic analysis requirements of the original HEMI proposal for nuclear security measures. Spectralyzer-based programs are also used in several aspects of the calibration, namely, to look for gain shifts or obvious miscalibrations in measurements, to determine the value of and remove the noise floor and saturation bins from measurements, and to characterize the measured peaks. The deduced threshold, saturation, and peak shape parameters are then specified in the detector response and applied to simulations.

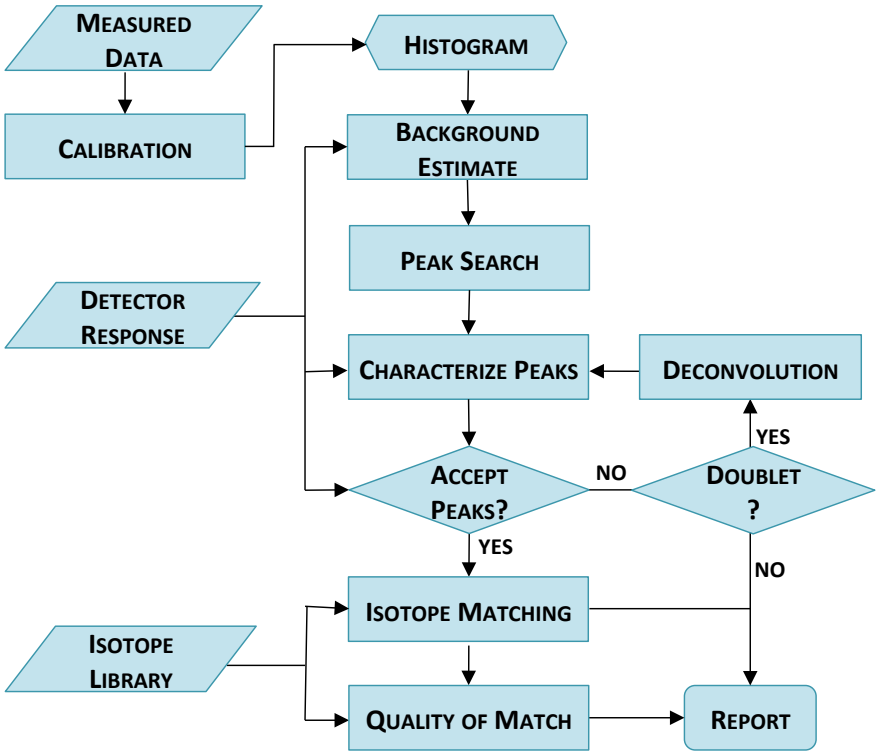

Figure 4.3: Spectral Analyzer flow chart.

The data-flow of the applied spectral analysis approach is shown in Fig 4.3. The background estimate and peak-based search algorithm are implemented using the class TSpectrum of the ROOT analysis package (*Morháč*, 2009). ROOT was used since it is freely available and allows for easy integration into MEGAlib. The spectral analyzer was written in C++ and has an object-oriented design. As described below, the algorithms incorporated in TSpectrum provide the basic functionality and accuracy required for the HEMI detection system.

The general data flow of the spectral analysis method is as follows: The measured (or simulated) data is first histogrammed, then a peak search algorithm is applied. For each identified peak, the energy-specific detector response parameters are used to inform the background fit parameters. After estimating and subtracting the background, the found peaks are characterized and evaluated as legitimate peaks or as potential multiplets. This step also utilizes the known detector response parameters that have previously been verified through benchmarked simulations. Potential multiplets can then be routed through a deconvolution process and reevaluated. Peak energies that pass the selection criteria either initially or after deconvolution are then matched to a list of candidate radioisotopes and assigned a confidence factor to indicate the likelihood that each match is correct.

4.2.1.1 Peak Search

The Mariscotti second differencing method in class TSpectrum is a peak search algorithm that is commonly used to identify statistically significant peak regions above a continuous background (*Mariscotti*, 1967). Over short intervals in energy, e.g., an energy range of several times the peak width, it is assumed that the background can be approximated as a linear function and that the peak shapes can be described by a Gaussian distribution. In such an interval, the number of counts as a function of energy, *N(x)*, can be described by equation 4.1, where the peak region is represented by the Gaussian function, *G(x)*, and the linear background is approximated as $Cx + B$.

$$N(x) = G(x) + Cx + B \tag{4.1}$$

In principle, for a continuous function the second derivative of Eq. 4.1 goes to zero in regions containing only a linear background. If a peak is present, the second derivative of the Gaussian function will not go to zero, and the maximum of the peak is given by the zero-crossing of the first derivative of *N(x)*. In reality, however, the data is represented by a discrete function, Eq. 4.2, where i is the energy, i_0 is the center of the peak, and A and σ are the intensity and Gaussian width of the peak, respectively.

$$N_i = Aexp[-(i - i_0)^2/(2\sigma^2)] + Cx + B \tag{4.2}$$

In the discrete case, the second difference, S_i, is used in place of the second derivative, Eq. 4.3, which also goes to zero except in the vicinity of a peak.

$$S_i = N_{i+1} - 2N_i + N_{i-1} \tag{4.3}$$

The spectrum is first smoothed prior to applying the peak search algorithm, thus reducing the false detection rate particularly for low statistics measurements. The smoothing function in ROOT is based upon a 353QH smoothing algorithm (*Friedman*, 1974). After several iterations of the smoothing algorithm, the second differencing method is used to find peaks. A threshold is then applied to the found peaks, whereby all peaks with amplitudes less than the threshold value multiplied by the amplitude of the highest peak are discarded. Increasing the threshold for peak detection will minimize the detection of false peaks, albeit as a trade-off for true but undetected peaks. Through a simulation using many sources at varying intensities, an optimum threshold value of 0.003 allowed for finding all relevant peaks including those from weak sources, backscatter peaks, and Compton edges in the case where they were not obscured by other peaks. False peaks from this set were easily eliminated based upon their statistical significance. Both the smoothing window and the peak detection threshold can be tuned prior to applying the peak search algorithm based upon the total counts in each accumulated dataset as well as the detected presence of strong sources.

Fig. 4.4 shows found peaks in a measured spectrum of ^{241}Am and ^{133}Ba sources incident upon a 42-detector planar array. Each of the expected peaks was found in addition to the noise floor at ∼35 keV and a broadened backscatter peak at ∼150 keV.

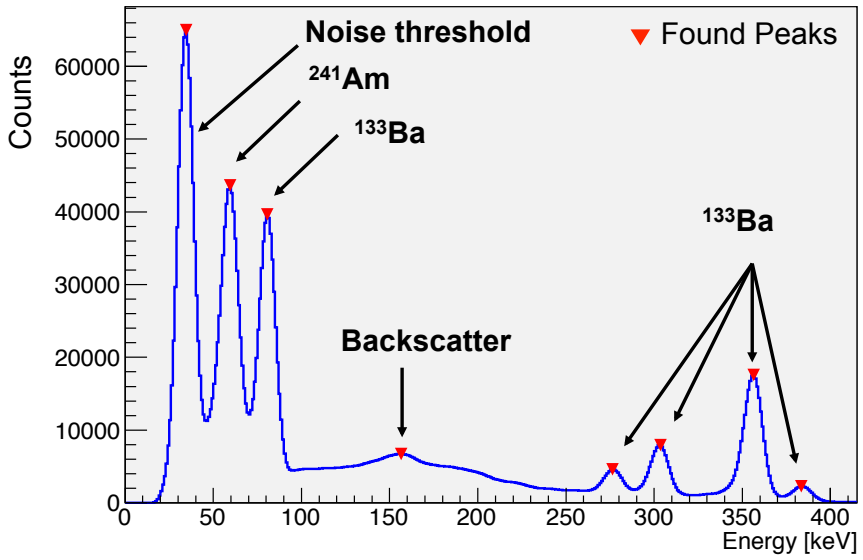

Figure 4.4: Peak finding algorithm applied to a HEMI measurement of ^{241}Am and ^{133}Ba sources.

4.2.1.2 Background Estimate

Prior to determining the peak area, amplitude, and fit parameters, it is necessary to estimate and subtract the background from the spectrum. The background estimation method in class TSpectrum is based on an optimized version of the Statistics-sensitive Nonlinear Iterative Peak-clipping algorithm, SNIP (*Ryan*, 1988). For low-statistics measurements, a smoothing function is first applied to the spectrum to reduce fluctuations. Then a zero-area digital filter is used to approximate the background continuum underneath peak regions. The filter operates as follows: Once the peaks are found in the previous step, the expected energy resolution for each peak energy is called from the detector response parameters and used to set a peak-clipping window width, w. For each region of width w, the background value is estimated as the lesser of two values: 1. $N(x)$, i.e. the number of counts at the peak energy x, or 2. the average value of $N(x)$ over the clipping interval, as shown in Eq. 4.4.

$$[N(x-w)+N(x+w)]/2 \tag{4.4}$$

In testing the parameters for the background estimate, it was found that a peak-clipping window of 3σ from a Gaussian peak fit is an accurate localized approximation and is predominantly effective within the higher energy end of the spectrum (above ~500 keV for a typical HEMI measurement). However, in measurements where the low-energy background is significant, a narrower window is needed to accurately approximate the background. Fig. 4.5 shows the effect of the clipping window size on the background estimate under a given peak.

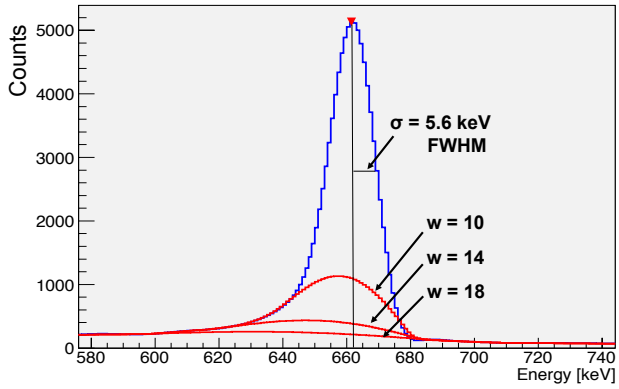

Figure 4.5: The effect of the clipping window width, w, on the background estimate underneath a 662 keV peak. The background estimation algorithm is applied over a region corresponding to $2w$. As w approaches 3σ of the peak width, the algorithm accurately approximates the linear background. For widths less than this, the background under a peak is overestimated, leading to an underestimation of the total peak area.

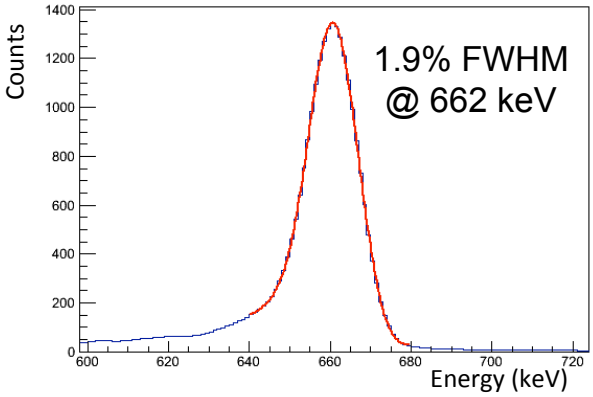

Figure 4.6: Measurement of a 662 keV line using a CdZnTe detector element with good performance. The applied fit function (red), a Gaussian convolved with a Landau distribution on the low energy tail, yields an accurate approximation of the peak shape.

4.2.1.3 Peak Evaluation

After background subtraction, each peak shape is fit with a Gaussian distribution on the main peak region convolved with a Landau fit on the low energy tail of the peak, the tail is a result of imperfect charge collection in the CdZnTe detectors. This fit shows good agreement with the peak shape of a typical HEMI CdZnTe detector element, as seen in Fig. 4.6. The convolved fit allows for a more accurate estimation of the total peak area.

After applying the peak fitting algorithm, the mean energy, total counts (less subtracted

background), and peak width are determined for each peak. The peak width from the Gaussian fit is compared to the expected FWHM for a HEMI CdZnTe detector element at the corresponding peak energy. If the found FWHM from the fit exceeds the expected width, the peak can be routed through a deconvolution process (section 4.2.1.4) as a potential multiplet. A factor of 1.5 times the expected FWHM was chosen as an acceptable limit on the width, as this allows for some variation in detector performance, and peaks with widths less than this value cannot be deconvolved. The mean energies from accepted peaks are matched to candidate isotopes (section 4.2.1.5). At this point, peaks can also be eliminated as statistically insignificant.

4.2.1.4 Deconvolution

It is sometimes the case that a single isotope or two different isotopes that are present within the detection environment may emit gamma rays that are very close in energy. Depending upon the separation between the lines and the energy resolution of the detector, the lines may not be able to be resolved, and instead appear as a broadened peak relative to the expected detector response. The misclassification of such a peak has several consequences: The mean energy becomes a weighted average of the combined peaks, leading to incorrect isotope identification while the true isotopes are not detected. Additionally, the peak activity of the identified peak is overestimated. Therefore, a method to separate and correctly identify peaks that are unable to be resolved by the detector energy resolution alone is highly desirable.

The Gold algorithm (*Gold*, 1964), one of the deconvolution algorithms available in class TSpectrum, can be used to deconvolve overlapping peaks in a spectrum. Because it is an iterative method that positively constrains the solution, it allows for the generation of a stable solution that is appropriate for a physical system. Parameters specific to the HEMI system, such as detector energy resolution and thresholds, can be used to further constrain the solution and minimize the number of iterations needed for an accurate deconvolution. Simulations of doublets centered around 662 keV were performed to test the effectiveness of this algorithm. Fig. 4.7, left, shows the limits of the deconvolution as a function of detector energy resolution, i.e., the minimum separation between two convolved peaks that are able to be accurately resolved with HEMI. Each of the single peak energies convolved in a doublet is resolved to within an accuracy of 1 keV after 100 iterations of the Gold deconvolution. On average, a minimum energy spread of approximately the FWHM between single peak energies is needed to resolve doublets. To resolve convolved peaks closer than the FWHM in the future, model fitting approaches could be used. A result of the deconvolution algorithm applied to two peaks separated by the FWHM at 662 keV is shown in Fig. 4.7, right. Although at the separation distance the peak areas may be slightly underestimated, deconvolution is able to reveal the presence of two distinct peaks.

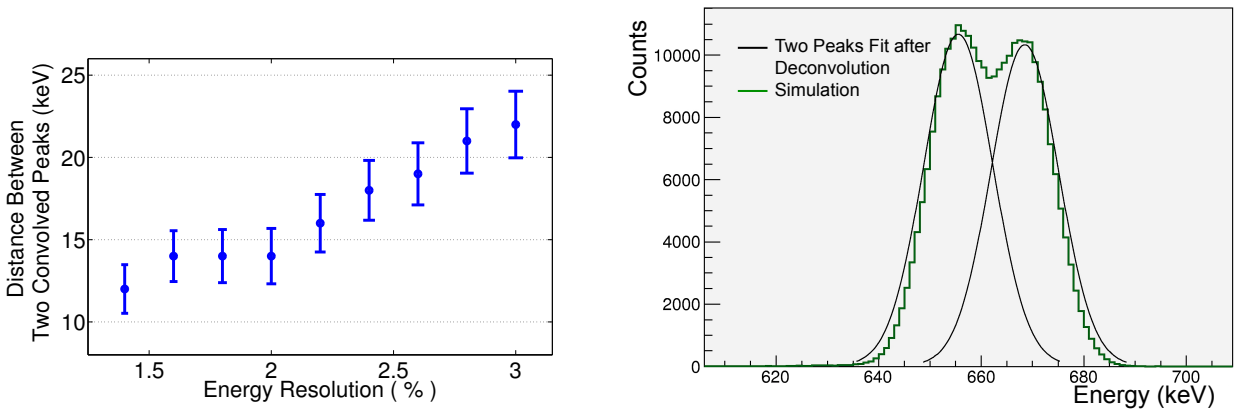

Figure 4.7: Left, deconvolution limit of simulated double peaks centered at 662 keV as a function of detector energy resolution using 100 iterations. Each single peak is deconvolved to within an accuracy of 1 keV. Right, result of deconvolution of two peaks centered at 662 keV and separated by the FWHM.

4.2.1.5 Isotope Matching

The found peak energies from the initial peak search or following deconvolution are then matched to gamma-ray energies from a library consisting of expected background radioisotopes (naturally occurring radioactive materials and daughter isotopes), medical and industrial isotopes, special nuclear materials, and their respective branching ratios (*Bossew*, 2004, *Firestone*, 1999, *nrc.gov*, *nti.org*). It was found through trial and error that the estimate of the peak mean can oscillate to approximately ± 1 keV, therefore isotopes that emit gamma-ray energies within 1 keV of the found energy are selected as candidates.

Once a list of candidate radioisotopes is generated, a quality factor can be assigned to each isotope to indicate the probability that it is a correct match. Several factors contribute to the confidence of the match. Using the known branching ratio information of the candidate isotopes, identified peaks can be verified or eliminated by cross-checking the presence and relative intensities of expected gamma-ray emissions at other energies. For an accurate comparison, the measured intensities must first be corrected for detector efficiency as a function of energy. If the distance to the source is known, a correction for attenuation in the environment can also be applied. In addition to evaluation of the line intensities, the presence of expected backscatter peaks in the spectrum and the locations of the Compton edges can also be used as additional verification measures. In addition to these factors, the statistical significance of the identified peak energy as well as the likelihood that the candidate isotope is present within the detection environment can also aid in assessing the quality of the match.

4.2.2 Coded-Aperture Analysis

The coded-aperture programs for HEMI serve two primary functions: A mask optimization program selects a detector configuration with a unique pattern and good signal to noise ratio, and an image reconstruction program uses a cross-correlation method to determine the most likely source position from the measured shadowgram.

For the mask optimization, various geometrical configurations of a 50%-filled random mask were generated. A cross-correlation method was used to determine the quality of the mask. Essentially, an optimal mask has the best point spread function (PSF) with the least amount of artifacts at the tails of the PSF.

For an optimized mask, each point source location on the sky results in a unique shadow pattern on the back detection plane of the instrument. To determine the location of a source for any given measurement, sources of various energies and incident angles are simulated for the HEMI instrument. This library of patterns is then compared to the measured pattern using a cross-correlation method to find the best fit, thus deducing the source position from the known position of the matched simulation.

The coded-mask algorithms developed for the HEMI prototype are being incorporated into MEGAlib. A detailed description of the coded-mask methods and its application to HEMI is described in detail in the following chapter.

Chapter 5

Characterization

This chapter describes the data analysis pipeline for HEMI as well as the methods used for benchmarking measurements with simulations. The characterization of the 96-detector (HEMI-96) prototype instrument is given in terms of energy, time, and angular resolution. Additionally, imaging methods are described and source localization demonstrated for both Compton and coded-aperture modes. The method used for determining point source sensitivities is described, and the resulting minimum detectable activities are given for the HEMI 96-detector prototype instrument.

5.1 Analysis Pipeline Overview

The data analysis pipeline for HEMI begins with the raw list-mode data acquired with the HEMI DAQ. The event list contains information regarding the detector ID, ADCs (analog-to-digital converter units), and a timestamp for each individual detector hit. An offline calibration is performed to convert ADCs to energies and the detector IDs to detector locations in cartesian coordinates. Detector hits below the trigger threshold and at the saturation limit are identified and eliminated from the measured data. From the calibrated measurement data, characterization parameters such as the energy resolution, time resolution, and coincidence time window can be determined and benchmarked.

For Compton mode, the next analysis step is to group individual coincident detector hits into Compton events. Following reconstruction and after applying appropriate event cuts, the efficiency and angular resolution measurement (ARM) is determined. A backprojected image is then created and can be refined through iterations of a maximum likelihood reconstruction algorithm.

For coded-aperture imaging, simulations of the calibration sources at various incident angles are first performed. The calibrated data is compared with simulated data using a cross-correlation method to determine the most likely incident direction of the source. This information is then converted to imaging space to arrive at source localization in coded-aperture mode.

Measurements can only access a limited sample of the full phase space of the instrument response (i.e. a few angles and energies), therefore the detector system can only be fully characterized using benchmarked simulations. Thus simulations are used to characterize the angular resolution in Compton mode, the effective area for both spectral and Compton modes, and the instrument sensitivity in spectral and Compton modes.

5.2 Calibration

The calibration of the HEMI CdZnTe detectors consists of 3 steps: converting the ADCs into an energy value, converting the detector ID into a position, and determining and removing both the noise floor and the saturation limit of each detector.

5.2.1 ADC to Energy

The online calibration implemented by the data acquisition software can be used to convert ADCs to energies for each detector. However, in order to get an accurate calibration and subsequently optimal characterization parameters for the HEMI instrument, an offline detector calibration is applied to each measured dataset. Because the gain may vary slightly from detector to detector, the ADC to energy conversion is assessed for each individual detector through periodic measurements with calibration sources. The ADC to energy conversion function is determined by fitting the resulting calibration data and was found to be linear with respect to energy.

Fig. 5.1 shows an example calibration, top, and residuals from the linear fit, below, for one of the detectors in the HEMI array. The error in determining the energy is less than ± 1 keV for each point. The resulting slope and offset from the fit are recorded for each detector. This information along with the detector ID to position conversion are then applied to the individual detector hits within the measured datasets. Additionally, the active and inactive detector volumes are automatically assessed and defined in the mass model (section 5.3.1) for each measurement during the pre-calibration stage of data analysis.

5.2.2 Thresholds

The high and low energy limits that are defined by the ASIC capabilities of each CdZnTe detector element are found through spectral analysis and removed from the measured datasets. These limits, namely the noise threshold and the saturation endpoint, are specified for each detector in the detector response parameters for simulations, as they are required for accurate modeling of the high and low energy response.

The low energy threshold settings in the HEMI instrument are optimized in order to operate each detector above its noise threshold without unnecessarily limiting the detection range in the low energy regime. Because the behavior of a few detectors or channels will

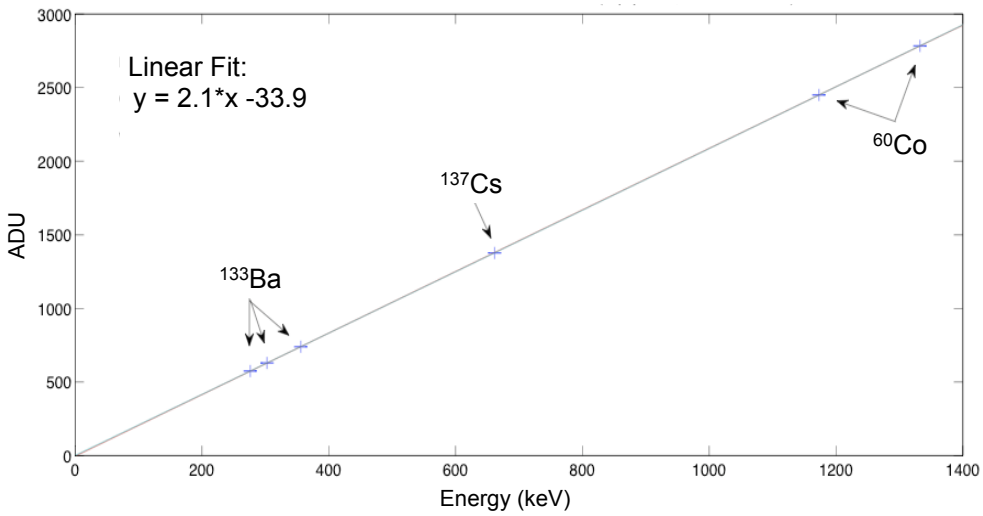

Figure 5.1: Example of ADC to energy calibration using detector 2 from the HEMI array. A linear fit showed good agreement for individual detector calibrations.

change over time in terms of varying noise thresholds, slight shifts in gain, or channel loss for unknown reasons, the threshold values are set prior to each measurement.

In the offline analysis, the spectral analyzer is used to locate and determine the value of the low energy threshold for each detector. To exclude the noise floor from the spectra, a low energy threshold of $+3\sigma$ above the maximum height of the noise is specified for the low-energy threshold value. All single-detector hits below this threshold are removed from the measured datasets. The threshold values are then included in the simulated detector response.

Fig. 5.2 shows the distribution of typical threshold settings based on a background measurement made with a HEMI-88 instrument. The settings range from 31 keV to 81 keV, with an average threshold setting of approximately 52 keV. Because the noise floor extends from the hard X-ray to soft gamma-ray regime, the detection sensitivity at these energies is limited. Therefore sources that emit low energy gamma rays, such as the 59 keV line from ^{241}Am, are more difficult to detect because in many of the detectors the line energy is either below the threshold or cannot easily be resolved from the noise peak.

Without inclusion of threshold settings in the detector response parameters, the threshold cutoff imposed by the data acquisition hardware results in fewer low energy hits in the measured data as compared to simulations. It is expected that Compton scattered events strongly contribute to these counts and therefore have a coincident Compton scattered counterpart at higher energies. Without setting a lower bound in the simulated performance, the additional lower-energy hits in simulation result in more Compton reconstructed events, and therefore a noticeable difference in the benchmarked efficiencies of the reconstructed photopeak. Prior to removing all simulated hits with energies below the measured threshold values,

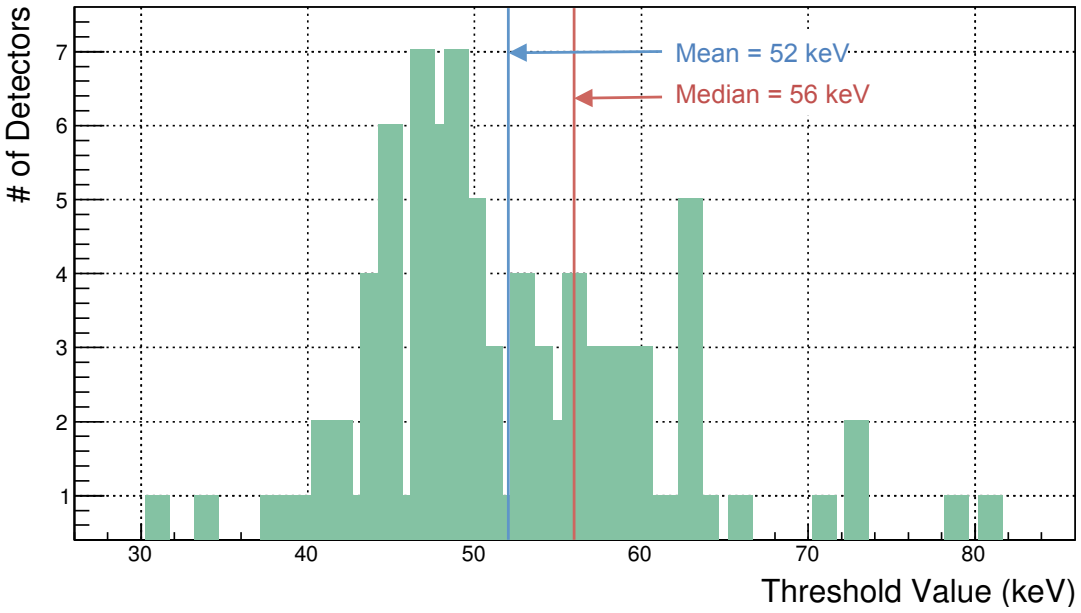

Figure 5.2: Distribution of threshold energies for each detector in a HEMI-88 instrument. The average threshold energy is approximately 52 keV.

a difference of efficiency in the reconstructed ^{137}Cs photopeak was approximately 14%. After specifying the threshold values in the simulated response, the benchmarked difference in efficiency for reconstructed events decreased to 6%. This implies that the PDD ASIC threshold limitation, as described in Chapter 3.3.1, is attributable to a marked decrease in the Compton imaging efficiency of the instrument.

Although the high energy saturation bins in the measurement do not necessarily affect the Compton reconstructed efficiencies, they do affect the benchmarked single-detector hit efficiencies and the detection sensitivity for sources above ~2.5 MeV. The peaks resulting from bin saturation are found using the same spectral analysis method as the estimation of the noise peak and are removed from the measured datasets. For simulations, the high energy cutoff values corresponding to the saturation limits of each detector are added to the response parameters.

5.3 Simulations

In order to predict the performance of the HEMI prototype and large-scale HEMI configurations, it is necessary to understand the detector response parameters. Comparisons between laboratory measurements and simulations provide a means to understand and fine-tune these parameters. Once the simulated detector performance is carefully matched with the actual instrument performance, simulations can be used to quantify several aspects of

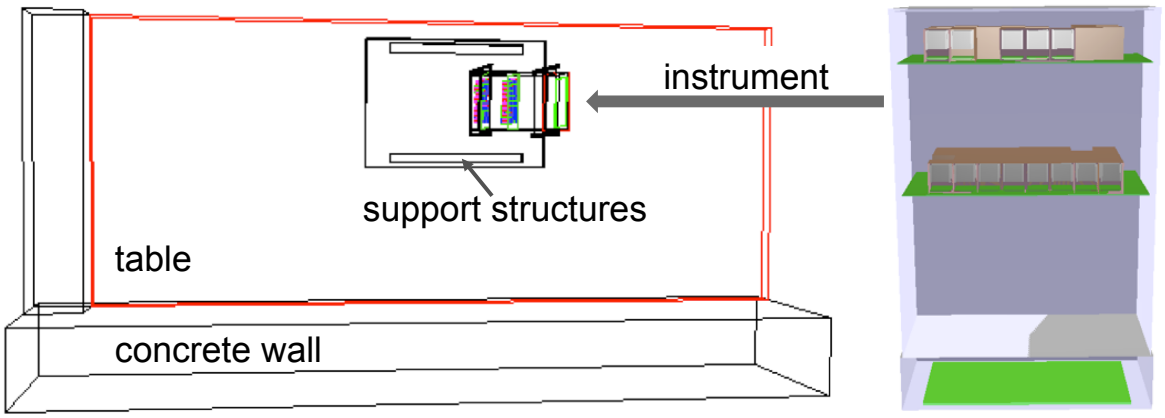

Figure 5.3: Geomega mass model of laboratory environment, left, and HEMI-96 prototype, right.

the instrument, such as what limits the angular resolution in Compton mode (energy or position resolution or Doppler broadening), an estimate of the effective area, and the sensitivity under different detection scenarios. Additionally, an accurate representation of the CdZnTe detector response allows for performance predictions of scaled versions and performance evaluations of different configurations of a HEMI-based instrument. This section describes the simulated models, the detector performance parameters, and the resulting characterization of the HEMI prototype instrument.

5.3.1 Mass Model

The first step in the simulation process is the construction of a detailed mass model of the HEMI detector assembly using Geomega (Chapter 4.1.1). This requires an accurate representation of all relevant passive and active materials of the detector system as well as objects in the nearby environment. Precisely defining the shape, volume, location, and material properties of each component is essential for a reliable reproduction of Compton scattering effects, pair creation, and photoelectric absorptions that take place within the actual HEMI system.

The mass model of the laboratory with the HEMI instrument is shown in Fig. 5.3, left, with the detailed 96-detector HEMI instrument model, right. The mass model was refined during the process of benchmarking the measurements to better match efficiencies and peak shapes in simulated energy spectra as compared to measured spectra. For example, a difference in the intensity and shape of the backscatter peak can indicate the presence of materials or structures that are unaccounted for in the mass model.

In addition to the detector and environment geometry, models for the calibration sources are included in the simulation. Each calibration source used for measurements was modeled

in detail according to the manufacturer's specifications for the source isotopic abundances, encasement materials, dimensions, as well as the decay-corrected activity. Correct specification for the Cosima simulator of the source location and the surrounding sphere radius (*Zoglauer*, 2009) allows for an appropriate simulation of the measured solid angle and subsequently an accurate representation of the number of incident photons.

5.3.2 Detector Response

The next step in creating accurate simulations is to determine the detector response parameters. These parameters include the time resolution, energy resolution with specified peak shape parameters, and a charge collection loss map for the detectors. With the exception of the charge collection loss map which is calculated using charge transport simulations, the remaining parameters are determined through a direct comparison of spectral features and countrates between the measured and simulated datasets. Refinement of these parameters allows for confident predictions of various configurations and scaled versions of HEMI.

5.3.2.1 Charge Loss Map

Proper modeling of the electronic energy resolution for the CdZnTe detectors requires the generation of a charge loss map to compensate for nonlinearities in charge collection as a function of the gamma-ray interaction position inside the detectors. To obtain an accurate model of the CPG detector response, it is necessary to normalize the signal pulse height as a function of the 3-D interaction location. For the HEMI CdZnTe detectors, the response normalization factor was determined first through calculations of the electrostatic potentials within the detector and the weighting potential distributions of the grid electrodes using the commercial software Maxwell (HEMI final report, *Amman*, 2013). Next the three-dimensional charge trajectories of each interaction position within the detector were calculated, yielding respective values of the signal induction on the electrodes. From this, the overall detector response map was derived by calculating the collecting and non-collecting grid electrode signals, then subtracting the two electrode signals as described in Eq. 3.2. The individual responses of the two grid electrodes were based upon typical detector biases, and the charge carrier mobility and lifetime product values were found by extraction from a set of sample detectors and taking the average. The overall detector response was optimized in the calculation by minimizing the resulting peak widths through the adjustment of the differential gain setting.

The resulting detector response model is shown in Fig. 5.4. The schematic, left, shows the calculation plane used to derive the response map, right. Typical grid bias, $V_g \sim$ -80 V, and detector bias, $V_d \sim 1$ kV, voltages were used in the calculation. For the plane of interaction shown in the schematic, one can see from the normalized pulse height that the response is uniform for all interaction locations except those that occur very near the grid electrodes (Z = 1 cm). The resulting charge loss map is included in the detector response parameters for simulation.

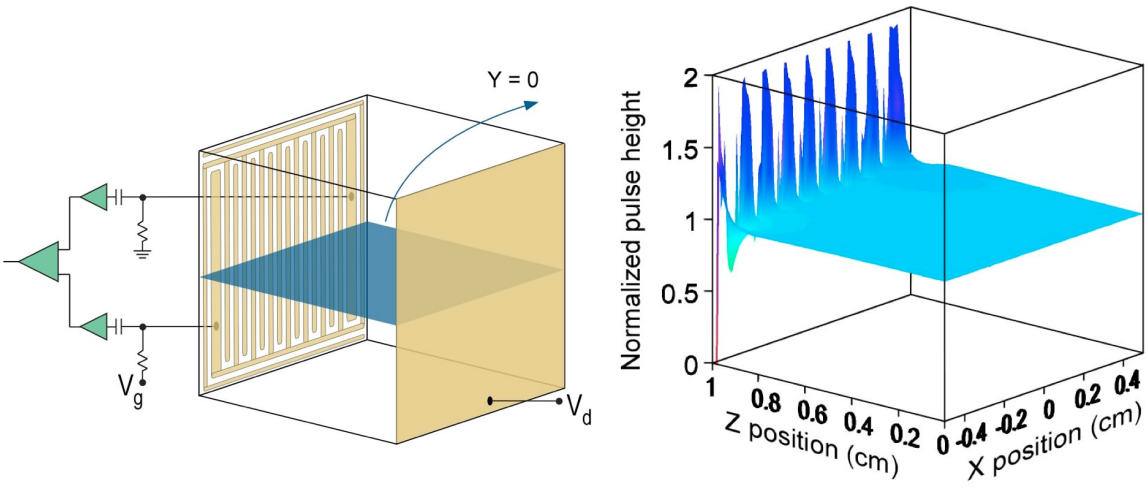

Figure 5.4: A schematic of the calculation plane used to obtain the charge loss map (at Y = 0, for example), left, and the resulting detector response as a function of interaction location at Y = 0, right (*courtesy M. Amman*).

5.3.2.2 Energy Resolution

Ideally, the charge collection loss map as described in the previous section would dictate the dominant contribution to the intrinsic energy resolution of the detectors. However, non-ideal detector effects such as electronic noise, non-uniform electric fields, and non-uniform charge trapping affect the peak width and shape in the measured spectra. Therefore an additional correction is required to accurately simulate the spectral performance of the detectors.

The measured energy resolutions of the installed individual detectors in HEMI-96 varied from about 1.4% to 2.9% FWHM at 662 keV. This variation required characterization of each individual detector, as the average performance parameters over the whole detector array did not give a good agreement between the simulated and measured performance of the 96-detector instrument, particularly for coded-aperture imaging (see last section).

Fig. 5.5 exemplifies the method used to determine the performance parameters of each detector. From the energy as a function of single detector hits histogram, top, the spectral analysis program was applied to find the peak energy within the region of interest and to estimate the local background under the peak, as seen in the middle histogram. The background subtracted peak is then fit with a Gaussian distribution over the mean peak energy, convolved with a Landau distribution on the low energy tail of the peak. This convolved fit shows a good agreement with the CdZnTe detector response (bottom histogram).

The resulting detector response parameters from the fit, i.e. the mean peak energy, a one sigma value for both the Gaussian and Landau components, and the ratio between the

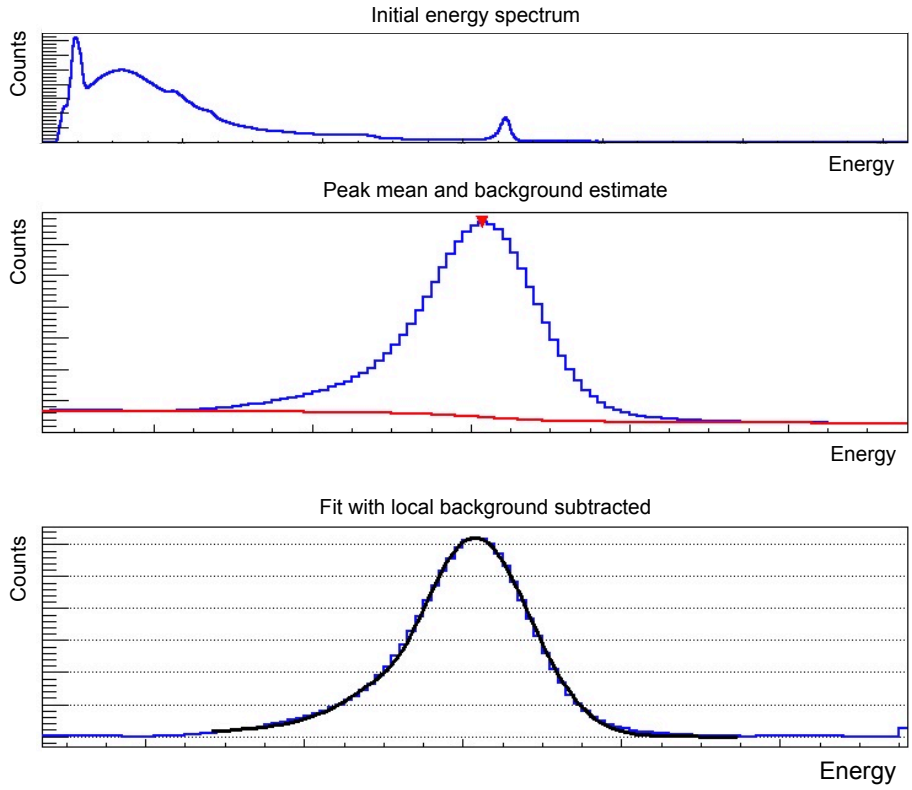

Figure 5.5: Example of the spectralyzer algorithm used to determine individual detector response using the 662 keV line from a HEMI-96 measurement with a ^{137}Cs source. First the number of counts as a function of energy histogram is generated (top). The peak in the region of interest is found, and the background is estimated (middle). After background subtraction, a Gaussian convolved with a Landau fit is then applied to the peak to estimate the energy resolution parameters (bottom).

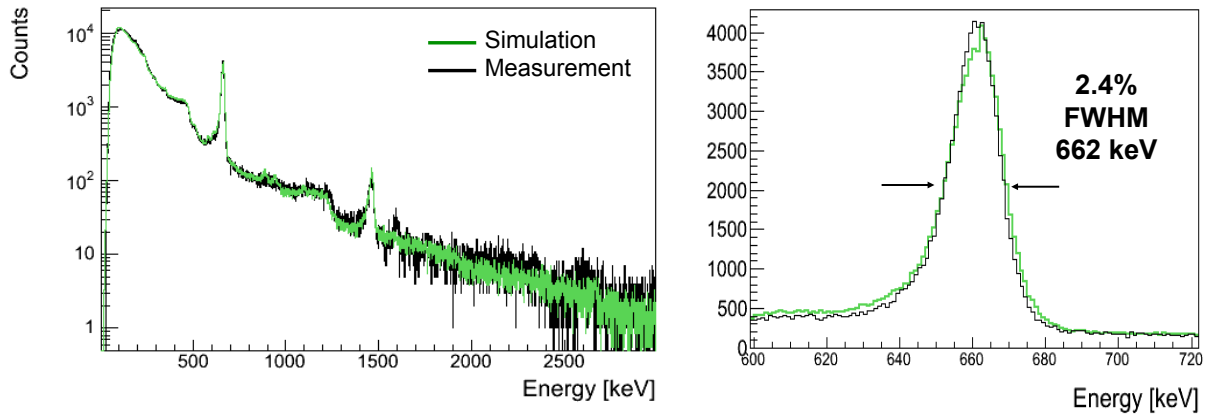

Figure 5.6: Benchmarked energy spectra scaled by time for a ^{137}Cs source measurement, black, compared with simulation including background (see 5.3.3), green, for single detector hits up to 3 MeV, left, and in the 662 keV photopeak, right.

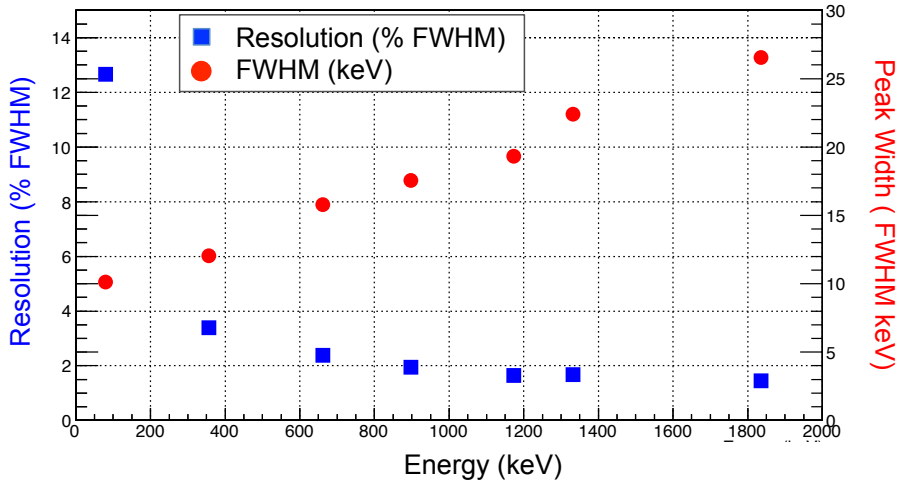

Figure 5.7: Energy resolution as a function of energy for HEMI-96.

two components, are stored for each individual detector and used as input into the detector effects engine for simulations. The detector effects engine convolves the ideal simulated hits with these noising effects, applying a linear interpolation between calibration points. The resulting simulated peak shape of the whole HEMI array is then matched to the measured peak shape. A visual check, a countrate comparison, and a χ^2-test of the peak match are used to verify that the energy resolution parameters accurately reflect the true response of the instrument.

This method was performed throughout the assembly and incremental growth of the

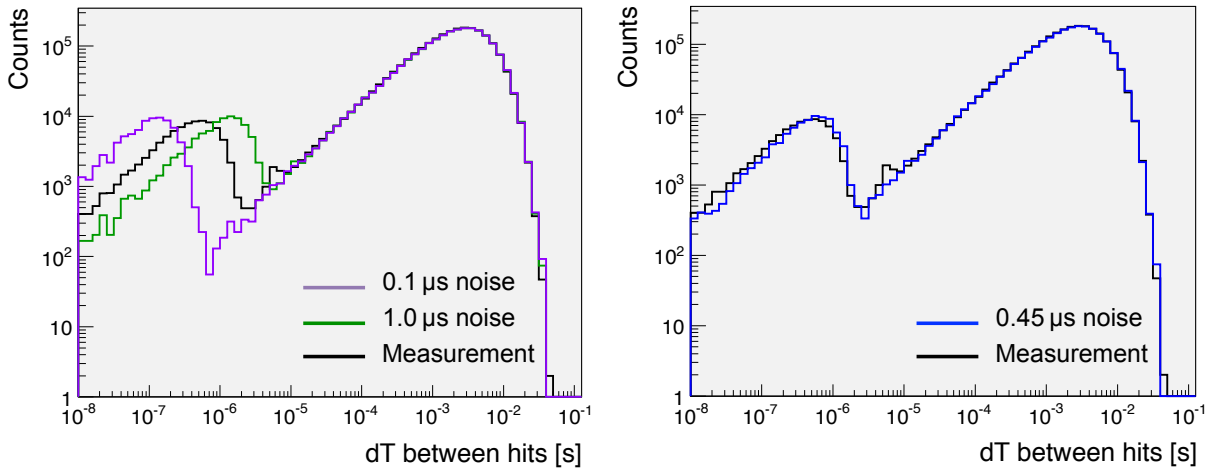

Figure 5.8: Difference in time between two adjacent detector hits for measurement, black, and simulation using various time noising values: 0.1 μs, purple, 1.0 μs, green, in the left histogram, and the benchmarked time resolution parameter, right histogram, using a noising value of 0.45 μs, blue, in the simulation.

prototype array (from only 1 detector up to 96 detectors). Fig. 5.6 shows the benchmarked energy spectrum of a ^{137}Cs source laboratory measurement up to 3 MeV, left, and for the 662 keV photopeak, right, scaled by time for single detector hits in the HEMI-96 array. The average energy resolution is 2.4% FWHM at 662 keV with a difference in efficiency of <2% in both the photopeak and in the range from 30 keV to 3 MeV (after folding in the background model, see section 5.3.3). Fig. 5.7 shows the resulting energy resolutions as a function of energy for an on-axis source at 1 m distance as measured with HEMI-96.

5.3.2.3 Time Resolution

The relatively long electron drift time in the CdZnTe detectors as well as inaccurate extraction of detector hit times due to the slow shaped detector signal leads to inaccuracy in the time resolution of the HEMI system. In order to accurately benchmark the measurements it is necessary to quantify a time noising parameter and add it to the simulated detector response. The time noising parameter is specified as a Gaussian distribution centered about the average response time. For each detector hit, the detector effects engine noises the timing with a randomly chosen value that lies within this distribution.

A histogram of the difference in time between two adjacent detector hits allows for characterization of the time resolution of the detectors, Fig. 5.11. Comparisons between measurement and simulations with various time noising parameters for a ^{137}Cs source incident upon a 96-detector HEMI array are shown. The simulations include a scaled-by-time background model, as described in the next section. The change in the time resolution of the

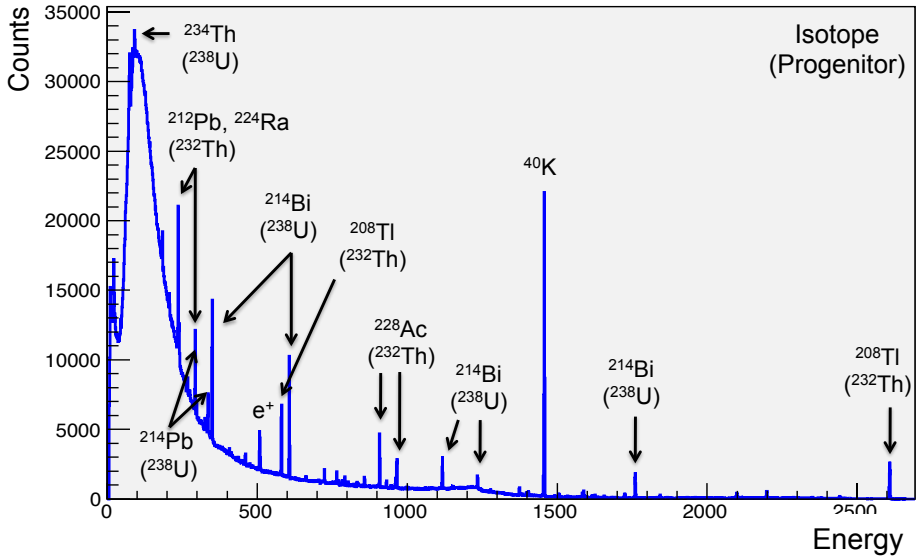

Figure 5.9: Measurement of the HEMI laboratory background using a Germanium detector. Identified isotopes and progenitors of the most prominent lines are shown.

HEMI system essentially shifts the distribution of counts along the abscissa of the histogram (dT). The average time resolution was determined by iterating through noising values until the simulated distribution aligned with the measured distribution as a function of separation time. The left histogram shows inaccurate matches using time response parameters of 1 μs, green, and 0.1 μs, purple. A close match was obtained using a Gaussian distribution with a 1σ value of 0.45 μs. As seen in Fig. 5.8, right, this yielded the best fit of simulations, blue, to the measured time resolution, black.

Also seen in the histogram is a small peak in the measured spectrum at a time interval of approximately 8 μs. This peak is most likely a result of crosstalk between two neighboring detectors. As it is outside of the Compton coincidence window (described in section 5.4.1), it does not interfere with the Compton reconstruction. Since these hits represent less than 1% of the photoabsorbed hits, they are considered to have a negligible effect on the coded-mask reconstruction. Therefore this feature does not need to be reproduced in simulations.

5.3.3 Background Model

In order to properly benchmark the laboratory measurements, the laboratory background must be included in the simulation. An accurate background model is important for estimating the sensitivity of an instrument, or in the case of nuclear security applications, the minimum detectable activity of a radioactive source.

In the HEMI laboratory environment, the background continuum is primarily a result of downscattered natural radioactivity from the concrete walls, floor and other materials

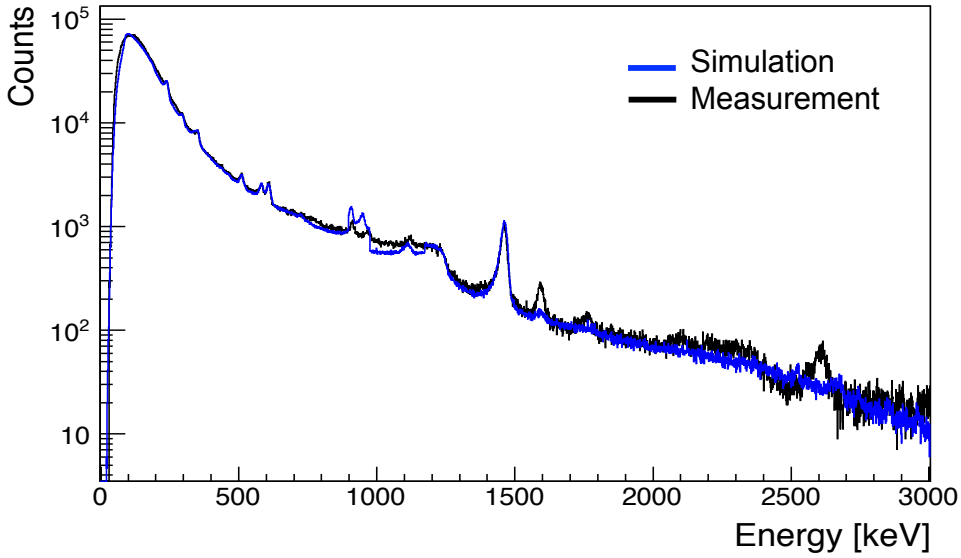

Figure 5.10: Comparison between background simulation, blue, and measurement, black for the HEMI-96 instrument within the laboratory. The missing peaks in the simulation above ~1.5 MeV are due to a difference in photoabsorption efficiency between the germanium detector, from which the model was derived, and the spectra as measured with the CdZnTe detectors.

surrounding the instrument. This activity can be simulated by embedding source terms for ^{40}K and the expected isotopes from the decay chains of thorium and uranium into the geometric model of the environment. The simulator then propagates the decay gamma-ray photons throughout the encasing volumes, typically concrete, and through air, resulting in a downscattered spectrum. However, such a simulation would be very time consuming, and many iterations would be needed in order to approximate the activities of the simulated sources in order to match the shape of the background continuum. Instead, it was found that a broken power law distribution provided a good fit to the shape of the observed background continuum.

For discrete emissions, a high purity germanium detector was used to obtain high resolution spectroscopy of the nuclear lines present in the laboratory, as shown in Fig. 5.9. The line energies and intensities were characterized using the spectral analyzer (see Chapter 4.2.1) and verified with literature characterizing typical laboratory backgrounds obtained through long-term measurements (*Bossew*, 2004 and *Novikova*, 2007). The nuclear line model was then scaled and added to the continuum model to arrive at a complete source term for the HEMI laboratory background. The relative activities of the line source and continuum mod-

els were adjusted iteratively through benchmarking with measurement until a close match between the two was achieved. The benchmarked background model shows a good agreement with the measured background to within 6%, as shown in Fig. 5.10.

Because the ^{40}K peak is prominent in the spectrum, care was taken to accurately model this line and benchmark the line shape. However, one can see from Fig. 5.10 that several lines at energies above ∼1.5 MeV appear in the HEMI measurement but have not been accurately modeled in the simulation. Referring to Fig. 5.9, these lines (e.g., ∼1.6 MeV, 1.76 MeV, and most of the lines above 2 MeV) are not as prominent in the spectrum obtained with the germanium detector, and therefore were not included in the model. The absence of these lines in the germanium spectrum could be due to a difference in the photoabsorption efficiency at higher energies of Ge as compared to CdZnTe (Z = 32 and Z = 49, respectively). However, given the relative intensity of the 1461 keV ^{40}K line as compared to the diminished lines at higher energies in the Ge spectrum, e.g., the 1.6 MeV line, it seems likely that these lines in the CdZnTe spectrum originate from either within the detectors or elsewhere within the HEMI instrument and associated electronics. As the HEMI project is predominately concerned with energies up to 2 MeV, the benchmarked model is a good representation of the measured background at all relevant energies.

Once the model was established, the resulting simulations are scaled by acquisition time and folded into each calibration source simulation. The combined dataset is then sorted by time to allow for chance coincidences between source and background photons.

Frequent measurements proved the laboratory background to be quite stable, therefore a one-time background model was simulated for HEMI-96. For more accurate modeling, controls to the laboratory environment such as shielding could be added. The model could also be informed and refined through continuous monitoring of fluctuations in the environment using a second detector, such as a high purity germanium detector. The intended real-world application of a HEMI-type instrument, however, would require operation under unknown and fluctuating backgrounds. Therefore a background model benchmarked to 6% is adequate for characterization of the instrument within the laboratory.

5.4 Compton Mode Analysis

Determining the source location in Compton mode consists of multiple steps, as described in the following sections. Coincidence timing (section 5.4.1) is used to determine which individual detector hits came from a single Compton scattered photon (coincident hits). An appropriate coincident time window is determined empirically, then a coincidence search is performed such that all subsequent hits that fall within a specified time duration of one another are grouped together as a single Compton event. Each Compton event is then reconstructed (section 5.4.2) to determine the energy of the incoming photon, the sequence of hits within an event, and the scattering angle via the Compton formula (Eq. 5.2). From the reconstructed events, one can benchmark the energy spectra and the angular resolution

of the instrument (section 5.4.3). Compton imaging methods (section 5.4.4) can then be applied to deduce the location and morphology of a source.

5.4.1 Compton coincidence timing

Historically, as in the case of COMPTEL, the time of flight between a detector hit on the top plane and a hit on the back plane of the telescope could be used to determine coincident hits and the sequencing of hits within a Compton event. This was possible due to the separation distance between detection planes and the nanosecond time resolution of the scintillators. However, in the case of compact Compton cameras such as HEMI, the distance between detection planes (7.5 cm for HEMI) is too small to see an appreciable difference in detector hit times based on the light travel time. Furthermore, rather than registering a hit through scintillation light, the upper limit on the coincidence window for the HEMI CdZnTe detectors is given by the electron drift time: $\sim$1 μs across the 1 cm detector length. The maximum time difference occurs when the photon interactions take place near the cathode of the detectors, as the electrons traverse the 1 cm length of the detector before arriving at the grid anode. Additionally, the detector signals have a relatively slow shaping time, $\sim$2 μs, leading to an inaccuracy in extracting the exact detector hit times. Because of these limits, the time between successive detector hits from a single Compton scattered photon can be on the order of a few microseconds.

A logarithmic plot of the time duration between two adjacent detector hits provides a useful visualization for experimentally determining the Compton coincidence window. Fig. 5.11 shows a time between subsequent detector hits histogram for a laboratory measurement of a $\sim$10 μCi ^{137}Cs source at 1 meter distance from the HEMI-96 front plane. The prominent feature at large separation times in the histogram is a result of uncorrelated, single-detector hits from the source and from the laboratory background. The single-detector hit peak falls off exponentially at shorter time durations, essentially reflecting the Poisson nature of radioactive decay.

An additional feature is seen that is peaked at about 0.6 μs. These hits, residing on top of the exponential decrease in single-detector hits, represent true coincident hits arising primarily from the $\sim$10 μCi calibration source, but also from true coincident hits from the background. To separate the majority of the non-coincident hits from true coincidences, a time window of 2.5 μs is selected, corresponding to the time difference at which the true coincident peak appears. The 2.5 μs time difference between two subsequent hits is consistent with the average time it takes for electrons to drift across the length of the detector in addition to the shaping time limitation as described above. All single detector hits that occur within 2.5 μs of each other are assumed to be Compton scattered photons that originated from a single incoming gamma ray. These coincident hits are grouped into Compton events, each event containing two or more coincident photons. Hits with larger separation times are assumed to have come from uncorrelated, single-interaction gamma rays and are processed as single-site events.

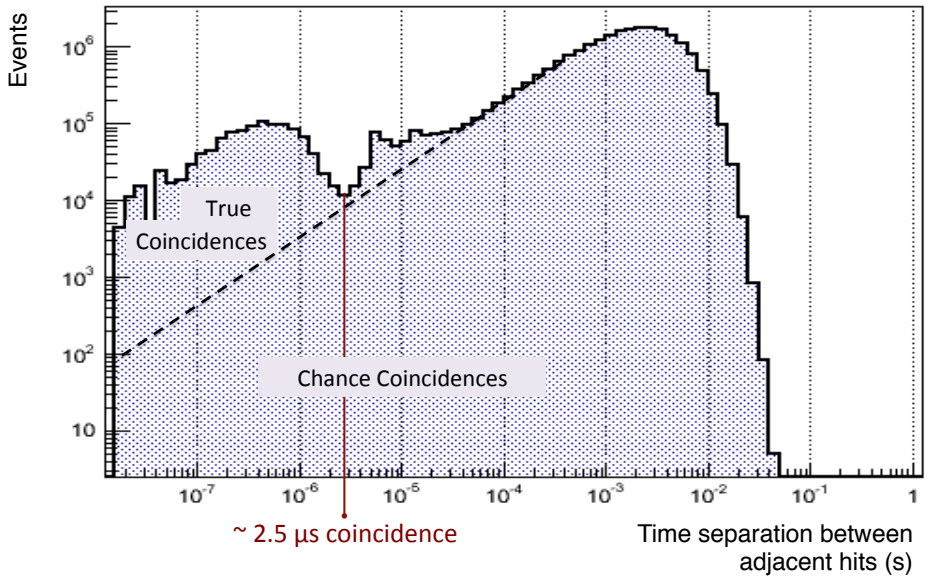

Figure 5.11: Time difference between temporally adjacent single-detector hits for an on-axis far-field ^{137}Cs source. The appearance of true coincident events from the source appears at a time window of ∼2.5 μs. The true to chance coincidence ratio in the laboratory is approximately 10:1.

One can see from Fig. 5.11 that the true coincidence peak forms on top of the chance coincidences of single-detector hits. In the case of HEMI laboratory measurements, i.e. a background activity on the order of 200 Hz, a small number of these chance coincidences also become grouped as Compton events. The true coincidence to chance coindence ratio for HEMI-96 in the laboratory is approximately 10:1. Many of these misreconstructed events can be eliminated prior to imaging by applying energy cuts to the Compton reconstructed data.

5.4.2 Compton Event Reconstruction

After grouping individual hits into Compton events using coincidence timing, the next step is to calculate the initial energy of the incoming photon and to determine the most likely sequence of hits within a given event. Benchmarking the reconstructed energy spectra provides a further check on the accuracy of the simulated model and the detector response parameters.

5.4.2.1 Energy Reconstruction

The total incoming photon energy, E_i, is the sum of the recoil electron energy, E_e, and the scattered gamma-ray photon energy, E_γ, as shown in Eq. 5.1. In practice, this energy is

reconstructed by summing the deposited energies from each hit within a Compton event.

$$E_i = E_e + E_\gamma \tag{5.1}$$

The total incoming photon energy is calculated assuming that the initial photon deposits all of its energy in one or more scatters within the sensitive volume of the instrument, therefore the sum of hits reflects the total energy of the initial incoming photon. However for each event there is a possibility that a scattered photon escapes the sensitive volume rather than being completely photoabsorbed in the detectors. For events that contain multiple scatters the chance of an escape photon is less likely.

Table 5.1 shows a comparison between of event types based on a measurement of a ^{137}Cs source on-axis at 1 m distance from the HEMI-96 prototype. A single-site event refers to hits that occur within only one detector, i.e. no corresponding Compton scattered photon is found within the coincidence window. Multiple hits that occur within one detector cannot be distinguished from one another in the measured data, and therefore are counted as single-site events in both measurements and simulations. One can see from the table that for 3-site events the reconstructed photopeak to total ratio increases significantly as compared to single-site and 2-site events. This is shown in a spectral comparison between 2-site and 3-site Compton events for the same measurement, Fig. 5.12.

	All Events	Peak/Total
Single-site	92%	0.03
2-site	8%	0.12
3-site	0.03%	0.17
4-site	0.001%	——

Table 5.1: HEMI-96 Compton reconstructed event distribution at 662 keV using measurements of an on-axis Cs-137 source at 1 m.

5.4.2.2 Reconstruction and Energy Spectra

The benchmarked efficiency for Compton ^{137}Cs events at a 1 m distance from HEMI-96 is shown in Fig. 5.13. The background-only measurement and simulation were first reconstructed and benchmarked to within 5% in imaging mode. This established accuracy in the background model in terms of Compton reconstruction, in addition to the previous benchmarking (within 6%) in spectral mode. The background simulation of single-detector hits was then folded into the source simulation prior to Compton reconstruction. For the combined ^{137}Cs source and background simulation, a difference in countrate of approximately 5% was seen in Compton imaging mode within the 662 keV energy region. This verifies that the model closely represents the detector response in terms of the coincidence search and summed energies.

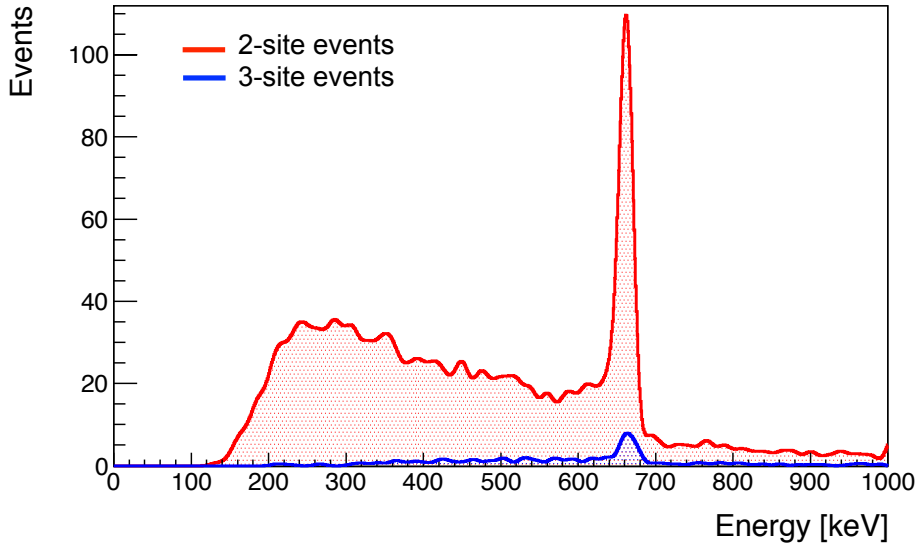

Figure 5.12: HEMI-96 comparison between 2-site (red) and 3-site (blue) Compton reconstructed measured events.

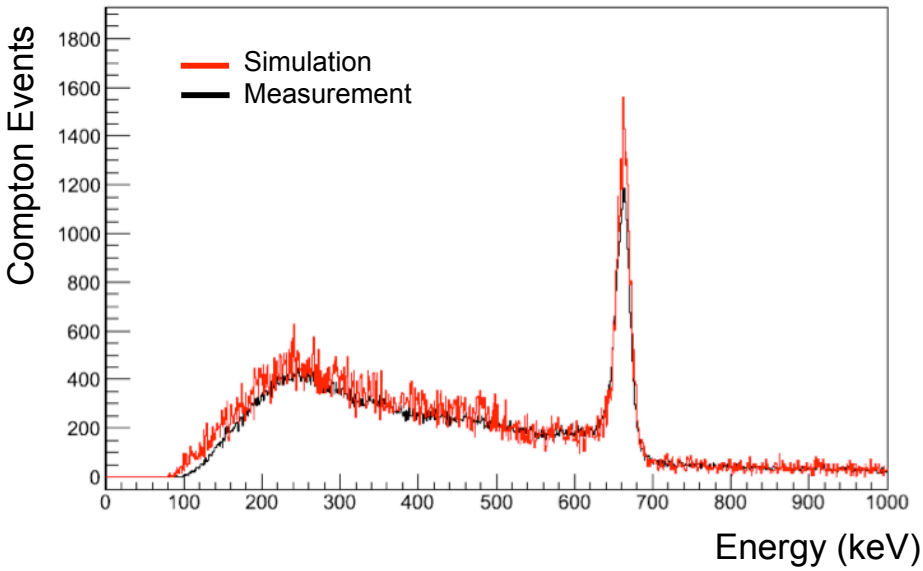

Figure 5.13: Simulated (red) and measured (black) summed energy spectra, scaled by time, are shown for Compton events from an on-axis ^{137}Cs source.

5.4.2.3 Scatter Angle Reconstruction

The scattering angle is calculated based upon the incoming photon energy and the energy of the scattered gamma ray as shown in Eq. 5.2 (*Compton*, 1923). If the first hit is misidentified, the designated energy values of E_γ and E_e are reversed, leading to an inaccurate scattering angle. Therefore, finding the correct sequence of hits is necessary for proper Compton reconstruction.

$$cos\phi = 1 - m_e c^2 (\frac{1}{E_\gamma} - \frac{1}{E_e + E_\gamma}) \tag{5.2}$$

To determine the proper event sequence, CSR (see Chapter 4.1) is used to find the most likely sequence of events. CSR analyzes all possible sequences of hits and assigns a Compton quality factor to each permutation based on the probability that each sequence is correct. To assess the accuracy of the reconstructed sequence, photoabsorption probabilities are used to evaluate the likelihood that the endpoint energies were fully absorbed in the detector material. At the central point of interaction, the Klein-Nishina probability can evaluate the likelihood that the incident photon energy resulted in the calculated scatter angle.

Compton kinematics are then used to eliminate physically improbable scatter angles. Since arccos has the domain [-1; 1], it follows from Eq. 5.2 that the allowable energies for the scattered gamma-ray energy and the electron recoil energy, E_γ and E_e, respectively, are constrained by the statements 5.3 and 5.4.

$$\frac{m_e c^2 E_i}{2E_i + m_e c^2} < (E_\gamma) < E_i \tag{5.3}$$

$$0 < E_e < \frac{2E_i^2}{2E_i + m_e c^2} \tag{5.4}$$

Kinematically, the minimum angle corresponds to no scattering at all ($E_\gamma = E_i$ and $E_e = 0$) and the maximum angle corresponds to a 180° backscattered photon.

5.4.3 Angular Resolution Measurement (ARM)

The ARM is a metric that describes the angular resolution of a Compton telescope (*Schönfelder*, 1993). Given a known source position, the ARM, $\Delta\phi$, is a measure of the difference between the true source position and the reconstructed source position projected by the Compton event circle as illustrated in Fig. 5.14. If the true origin of the photon lies inside of the event circle, from the Compton formula, Eq. 5.2, one can see that the scatter angle was overestimated, most likely implying that the scattered gamma ray was incompletely absorbed, i.e. the reconstructed energy is less than the true energy. This corresponds to a negative $\Delta\phi$ value. In the case of underestimation of the scattered angle, a photon origin outside of the event circle, $\Delta\phi$ has a positive value, and Eq. 5.2 implies an incompletely absorbed recoil electron. The width of the Compton circle corresponds to the angular resolution of each Compton event, $\delta\phi$.

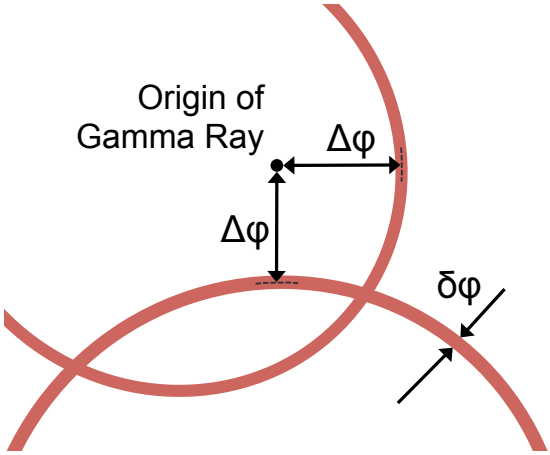

Figure 5.14: The angular resolution measurement, $\Delta\phi$, is defined as the smallest angular distance between the known gamma-ray origin and the reconstructed source location, as indicated by the Compton circles. The uncertainty, $\delta\phi$, corresponds to the FWHM width of each cone.

The FWHM of the ARM distribution is a combination of the achievable energy resolution, position resolution, and Doppler broadening. In the Compton interaction process, the recoil electrons in reality are not stationary but have some indeterminable momentum that leads to an uncertainty in the momentum transferred to the electron. This uncertainty adds a finite width to the angular resolution known as Doppler broadening. The effect is most pronounced for low gamma-ray energies, large scatter angles, and high Z detector materials. Doppler broadening is the fundamental limit to the angular resolution of Compton telescopes below a few hundred keV (*Zoglauer*, 2003).

The benchmarked angular resolution for HEMI-96 corresponds to approximately 9.5° FWHM at 662 keV, as shown in Fig. 5.14. Following benchmarking, simulations can be used to quantify each of the three components for the HEMI instrument. The results, shown in Table 5.2, reflect that the ARM for HEMI is primarily limited by position resolution. This is due to the large cubic centimeter voxel size of the CdZnTe detectors. The on-axis angular resolution as a function of energy is shown in Fig. 5.16, as determined through measurements of various calibration sources with HEMI-96.

Component	Contribution
Doppler Broadening	$1.17° \pm 0.06°$
Plus Position Resolution	$8.8° \pm 0.4°$
Plus Energy Resolution	$9.5° \pm 0.5°$

Table 5.2: The three components and their contributions to the broadening of the ARM distribution.

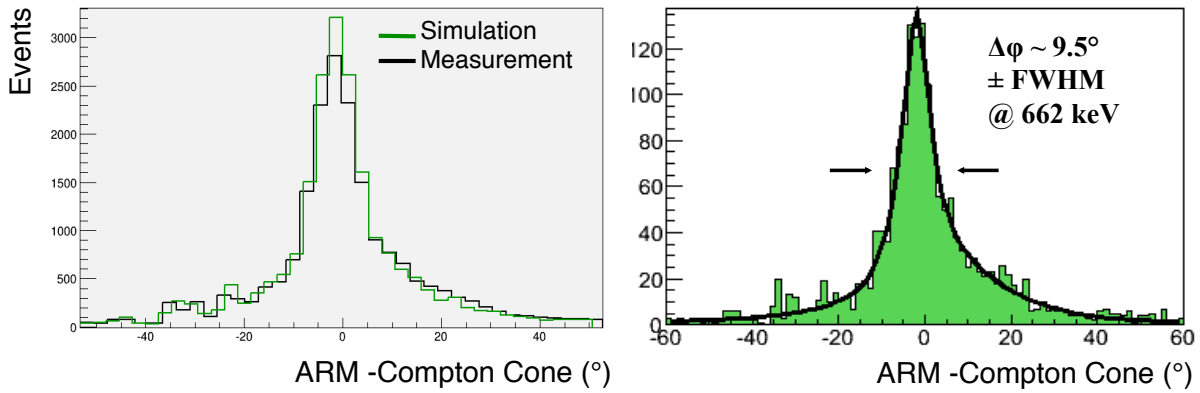

Figure 5.15: Benchmarked, left, and characterized, right, Angular Resolution Measurement distribution for an on-axis ^{137}Cs source.

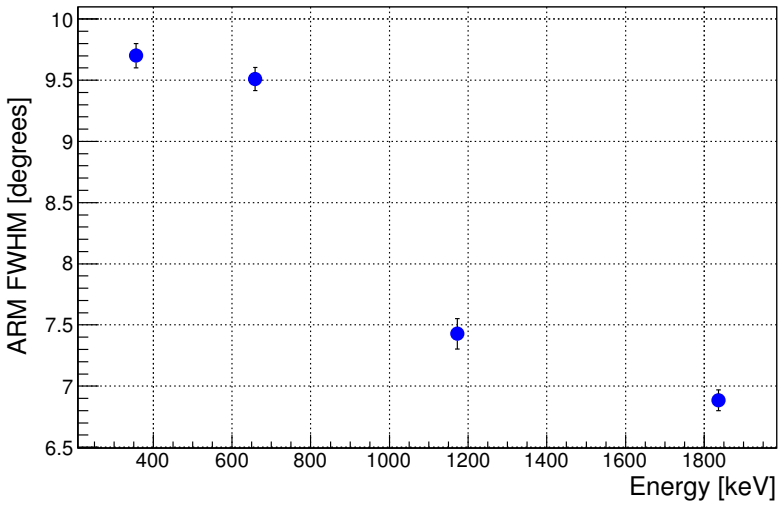

Figure 5.16: Angular resolution (ARM FWHM) as a function of energy.

5.4.4 Compton Imaging

Imaging of gamma rays allows for deducing the source location and distribution based upon the reconstructed event data. Using the Mimrec package in MEGAlib (*Zoglauer*, 2011), this is done either through a backprojection of the selected reconstructed Compton event circles into imaging space or through a list-mode maximum likelihood expectation-maximization (LM-MLEM) algorithm (*Wilderman*, 1998). The key to turning the event list data into an image through MLEM is an inversion of the measurement process to arrive at a deconvolved

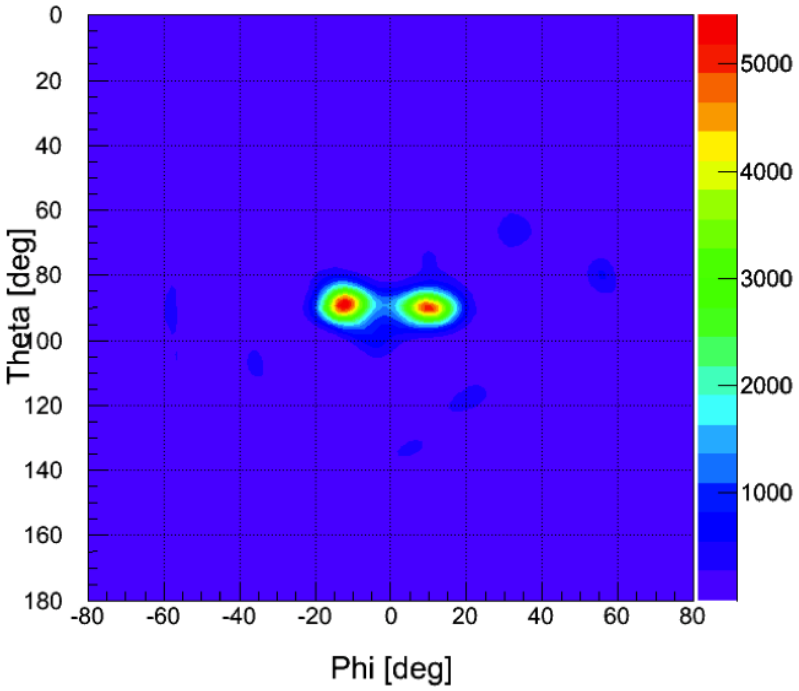

Figure 5.17: Compton reconstructed image of emission lines from two far-field sources, the 511 keV line from ^{22}Na (left) and the 662 keV line from ^{137}Cs (right), separated by 20 degrees, as measured with HEMI-96.

source intensity. From the backprojected or deconvolved event data, MEGAlib then allows for the generation of Cartesian and spherical images of the source location. More information on MEGAlib Compton imaging techniques can be found in *Zoglauer* (2000, 2011).

5.4.4.1 ARM verification

The obtainable angular resolution was verified through imaging of two sources of similar energies separated by 20° in the azimuthal direction. Fig. 5.17 shows the two point spread functions, left, and a Compton reconstructed image, right, of a ^{22}Na source (511 keV) and a ^{137}Cs source (662 keV) measured at a 100 cm distance from HEMI-96. Because the angular resolution varies slightly as a function of energy, sources with similar line energies were used for the demonstration. The image contains approximately 1000 events (10 s observation time) and was obtained after 20 iterations using a maximum likelihood method. An event cut based on the instrument geometry has been applied to include only events where the first two Compton scatter interactions occur in different detection planes. The reason for this cut is due to ambiguity in the source location when reconstructing hits that occur within the same detection plane.

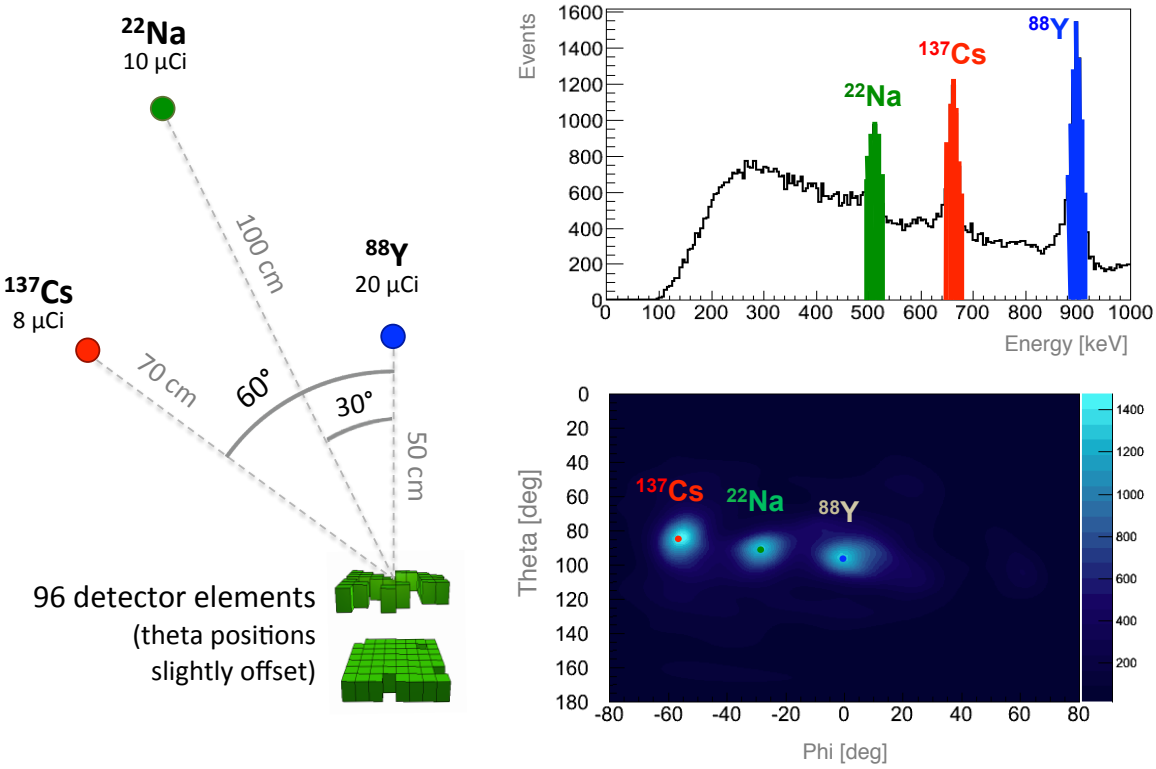

Figure 5.18: A three source measurement obtained with the HEMI-96 instrument of ^{88}Y on-axis, ^{22}Na at Φ=30°, and ^{137}Cs at Φ=60°. An energy gate is applied to the Compton reconstructed spectra, top right, prior to simultaneous imaging of the three sources, bottom right.

5.4.5 3 Source Measurement

A measurement of three different sources at different locations in phi with respect to the HEMI detector was made in order to demonstrate source localization. The source strengths for ^{22}Na-22 (Φ=30°), ^{137}Cs (Φ=60°), and ^{88}Y (on-axis) were approximately 10 μCi, 8 μCi, and 20 μCi, respectively. The data was reconstructed in Compton mode using only events where the incoming photon scatters from the top plane to the bottom plane. Shown on the left of Fig. 5.18 is an illustration of the source locations and activities. The top right of Fig. 5.18 is the three source Compton reconstructed energy spectrum which includes two-site to five-site events. For the image reconstruction, a $\pm 1.4\ \sigma$ energy window is applied to each peak: ^{22}Na-22 (green), ^{137}Cs (red), and ^{88}Y (blue). Below the energy spectrum is shown a simultaneous image of the three sources showing their correct locations. The image contains ~10,000 counts over a 30 minute observation time. Deconvolution was performed using 20 iterations of a maximum likelihood algorithm.

5.5 Sensitivity in Spectral and Compton Modes

The true metric of an instrument is how well it is able to detect and image a source above a radioactive background. The detection and imaging sensitivity depends upon the efficiency of the instrument, the observation time, and the background conditions. Concerning the detector characterization the key element is the efficiency of the instrument, which can be described in terms of the effective area. Based upon the effective area, the sensitivity of an instrument is a quantitative description of the minimum flux that can be detected within a specified significance above background. This value can be described in terms of the minimum activity that a source must emit in order to be detected or imaged under certain circumstances (e.g., background activity, distance from source, observation time, event cuts).

5.5.1 Effective Area

Because not all of the photons that are incident upon the geometric area of a detector interact to produce counts or real events in the detector, the effective area represents the area of the detector that does result in detector hits or useable events. The effective area is a reduction from the geometric area as a result of both the intrinsic detector efficiency, i.e. the ratio of the number of incident photons to the number of photons that interact within the detector material to produce counts, and a reduction of counts due to event selections used in the reconstruction process. As shown in Eq. 5.5, the effective area depends upon the direction and energy of incident photons, where A_{geo} is the geometric area of the detector, $N_{incident}$ is the number of photons incident upon the detector, and $N_{detected}$ refers to the total number of recorded events after selections. $N_{incident}$ takes into account the solid angle of detection as well as the attenuation of photons in air between the source and detector.

$$A_{eff}(E,\theta,\phi) = A_{geo}\frac{N_{detected}}{N_{incident}} \tag{5.5}$$

When determining the effective area through simulations, the Eq. 5.6 is used to determine the effective area, where A_{start} corresponds to the start area of the photons and N_{start} is the number of counts generated from this area over a given observation time.

$$A_{eff}(E,\theta,\phi) = A_{start}\frac{N_{detected}}{N_{start}} \tag{5.6}$$

Table 5.3 shows the effective area for spectral and Compton imaging modes for HEMI-96 at 662 keV based upon simulations of a far-field, on-axis ^{137}Cs source. The geometric cut in imaging mode includes only those events where the first two interactions occur in different detection planes. An efficiency of 100% corresponds to an effective area equal to the geometric surface area of the instrument, i.e. 64 cm^2 in spectral mode and 32 cm^2 in imaging mode.

Mode and Event Cuts	Efficiency to 662 keV photons
Spectral single-site hits	
All events	51.2 %
Full-energy peak (±20 keV)	8.0 %
Compton imaging	
All events	8.3 %
Full-energy peak (±20 keV)	3.4 %
Geometric cut	0.60 %
ARM cut (± 6.6°)	0.34 %

Table 5.3: HEMI-96 efficiencies to 662 keV incident photons obtained from simulations of an on-axis ^{137}Cs source at 1 m distance. An efficiency of 100% corresponds to an effective area equal to the geometric surface area of the instrument, i.e. 64 cm^2 in spectral mode and 32 cm^2 in imaging mode.

5.5.2 Sensitivity

The sensitivity of a detector is a description of the minimum flux which can be measured by the instrument within a given significance. At the sensitivity limit, the number of detectable source counts, N_s, is defined by the minimum flux, F_{min}, according to Eq. 5.7 (*Jacobson*, 1975).

$$N_s = F_{min} A_{eff} T_{obs} \tag{5.7}$$

The number of source counts that satisfies the minimum detectable flux is dependent upon the signal to noise ratio as shown Eq. 5.8, where n is the number of standard deviations away from the photopeak energy required for detection and ΔM_s is the uncertainty in the measurement. Typically a standard deviation of 3σ or 5σ is considered statistically significant, depending upon the application.

$$n\sigma = \frac{N_s}{\Delta M_s} \tag{5.8}$$

The uncertainty in the measurement, ΔM_s, takes into consideration the uncertainty in the source counts and in the background counts. Because the observation times for standoff detection are typically within the range of a few seconds to a few minutes, the photon statistics in the background photopeak region over these short observation times are limited. This is due to the small effective area (and geometric area) of the HEMI prototype instrument and the relatively low background activity in the HEMI laboratory environment. To minimize the statistical uncertainties in the calculated sensitivities, Poisson statistics are obtained by using a longer background observation time. The differing source and observation times are then normalized in the minimum detectable flux calculation, Eq. 5.9, where C_b is the

background count rate, and T_s and T_b are the source and background observation times, respectively. A derivation of Eq. 5.9 can be found in *Jacobson* (1975).

$$F_{min}(E,\theta,\phi) = \frac{n^2 + n\sqrt{n^2 + 4C_bT_s(1+\frac{T_s}{T_b})}}{2A_{eff}T_s} \tag{5.9}$$

In practice, the source and background are simulated separately in order to determine the sensitivity. For the HEMI instrument, the source counts and background counts, over their respective observation times, are found by integrating over the region of $\pm 1.4\ \sigma$ of the photopeak energy. In imaging mode, the counts are derived from the resolution element of the point spread function (PSF), i.e. $\pm$FWHM of the ARM distribution in Compton mode. The same energy cut is applied to the PSF. Compton mode also includes a plane-to-plane geometric event cut.

5.5.3 Minimum Detectable Activity

For nuclear threat detection, it is useful to look at the minimum activity a source must have in order to be detected by an instrument in either spectral or imaging modes. In order to put the minimum detectable flux in terms of the MDA, the branching ratio of the source, R_b, the energy-dependent photon attenuation in air, ϵ, and the radial distance to the source, r, are taken into consideration, as shown in Eq. 5.10.

$$MDA = F_{min}\frac{4\pi r^2}{\epsilon R_b} \tag{5.10}$$

The resulting minimum detectable activities for a 3σ significance of the 662 keV line from a ^{137}Cs source measured on-axis with the HEMI-96 prototype are shown in Fig 5.19. A difference of roughly two orders of magnitude is seen for the MDA in spectral vs. imaging mode. As a point of comparison, the grey arrows in Fig 5.19 indicate the MDAs for a 20 second observation time at a 20 m standoff distance: Minimum activities of $\sim$0.2 mCi in spectral mode and $\sim$20 mCi in Compton imaging mode are required to detect and image a ^{137}Cs source, respectively. These calculations were performed using a stable, well-characterized laboratory background. In a real-world detection scenario, the same MDA results may not apply as a fluctuating background with unknown isotopic abundances and distributions can significantly affect the detection and imaging sensitivities.

5.6 Coded-Aperture Mode Analysis

Using HEMI as a coded aperture instrument in addition to a Compton imager allows for increased sensitivity in the energy range from hard X-rays to soft gamma-rays. Imaging in this band is relevant for applications in Homeland Security, particularly for the detection and imaging of a ^{235}U source, as its strongest emission line is at 185.7 keV. As described in

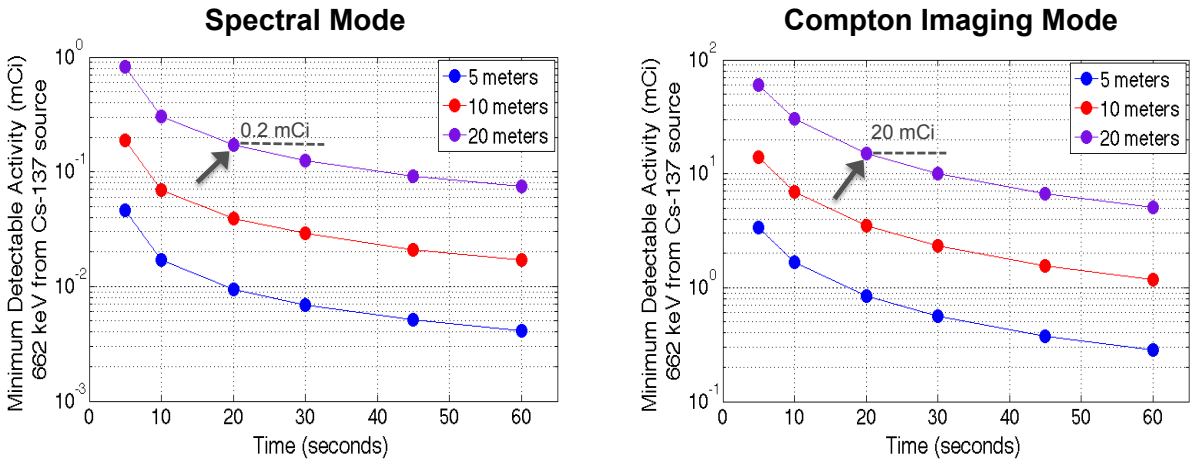

Figure 5.19: Minimum detectable activities for a 3σ significance detection of 662 keV from a ^{137}Cs source. Various on-axis distances from a HEMI-96 instrument are shown. Grey arrows indicate the minimum detectable activities at a 20 meter standoff distance with 20 seconds of observation time: ~0.2 mCi in spectral mode and ~20 mCi in Compton imaging mode.

Chapter 2, photoabsorption interactions dominate over Compton scattering at lower energies, i.e. <300 keV for CdZnTe, thus motivating the use of geometrical optics techniques for increased imaging sensitivity in this region.

The image quality from a coded-mask instrument depends upon the mask pattern, the geometric configuration, e.g., the mask pixel spacing and the distance between the mask and detection plane, the position resolution of the detectors, the extent of coding, and the method used for image reconstruction. The mask optimization and reconstruction algorithms that were used for HEMI were developed by *Zoglauer* (unpublished, 2012). This section describes the coded-aperture design for HEMI. Coded-aperture imaging from measured calibration sources in the laboratory is demonstrated for the HEMI-96 prototype.

5.6.1 Mask Pattern

The development of HEMI as a coded aperture instrument began with the choice of a mask pattern with a specified ratio of transparent elements to total mask area, i.e. the open fraction denoted as f_e. To obtain the best signal-to-noise ratio, the open fraction of the mask is optimized according to the expected point source intensity relative to the background intensity (*Gunson and Polychronopulos*, 1976). It was found that the optimum fraction is $f_e = 1/2$ if the background level dominates over the source intensity. This result was reviewed under various detection scenarios (*in't Zand*, 1992 and *Skinner*, 2007). Considering the real-world HEMI application, an open fraction of $f_e = 1/2$ is an appropriate choice.

An optimal mask pattern has an autocorrelation function that is a delta function, i.e. a Point Spread Function (PSF) consisting of a single peak from source photons surrounded by flat sidelobes or a plateau from background photons. A pinhole, for example, has an optimal PSF but poor sensitivity, as the pinhole size limits the detectable flux. The pinhole can be enlarged but at the cost of angular resolution. For this reason, a random pinhole pattern was first suggested for use in astronomical telescopes by *Dicke* and *Ables* (1968). The random placement of multiple pinholes enlarges the open area for increased flux, thus providing better sensitivity to point sources, while maintaining the angular resolution by keeping the size of the pinholes small. The random placement of the holes preserves the uniqueness of the mask pattern, thus allowing for an optimal PSF.

In addition to the random pinhole pattern, several choices of mask patterns exist such as Non-Redundant Arrays, Uniformly Redundant Arrays (NRAs and URAs, respectively), and geometric designs. A review of these patterns can be found in, e.g., *Caroli* (1987). Several of these patterns have instrument geometry requirements that make them infeasible for use with HEMI. URAs, for example, rely on the repetition of the coded pattern in cycles of whole numbers for good image quality, thus requiring a large fully-coded field-of-view, i.e. a mask that is much larger than the detection plane, in order to project several sequences of the same pattern for a given source location. Because the mask of HEMI is the same size as the back detection plane, a fully coded field-of-view is only obtainable for sources that are directly on-axis. Additionally, the spatial limitation of 64 channels on each detector plane (32 mask detectors) and the cubic-centimeter sized elements (square surface area) of the HEMI prototype instrument limits the permutations and shapes that would be required for an optimal NRA or for most physically realizable geometric patterns. Thus a random pinhole pattern was determined to be an appropriate choice for the HEMI prototype instrument.

5.6.2 Mask Optimization

In an ideal coded-mask instrument, photons from a source either pass through the transparent elements of the mask unobstructed and are absorbed by the backplane, or are fully photoabsorbed by the front plane, creating a shadow of the mask pattern onto the backplane. For an optimized mask, the projected shadow pattern from the mask onto the detection plane encodes each source location in a unique way. Depending upon the source position relative to the central axis of the instrument, the pattern maintains the same code but is shifted on the position sensitive detection plane. Given the uniqueness of the pattern, the projected shadow relative to the detection plane can be decoded to yield the direction of the incoming source photons.

In order to obtain an optimized mask pattern, i.e. a reconstructed image resulting in a delta function with flat side-lobes, a set of random masks was generated and simulations performed using sources within the mask field-of-view. The figure-of-merit for each pattern includes a reconstructed image that has a relatively uniform efficiency across the field-of-view with no spurious responses, e.g., "ghost" sources, artifacts, sidelobes, or excessive noise. A completely uniform field-of-view is not achievable for HEMI because the mask must maintain

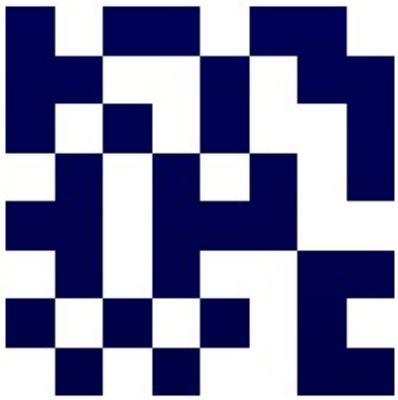

Figure 5.20: The optimized random mask pattern as implemented in HEMI-96.

randomness within a small geometric area. It is also an important figure-of-merit that the source location for all directions can be accurately resolved, given the limitation that all off-axis source locations are within a partially coded field-of-view for HEMI.

First, sets of random mask patterns were generated and subsequently evaluated. In order to ensure that the best mask patterns were optimized globally rather than locally, a genetic algorithm was used to evolve the patterns obtained from a large set of random masks (*Zoglauer*, private conversation). The algorithm varied the patterns by switching and inverting elements and exchanging sections of patterns between mask pools.

Additionally it was required that each n x n sub-pattern maintain a maximum closed fraction (1 - f_e) given by Eq. 5.11, and that no n x n sub-pattern repeats within the entire mask pattern. For the 8 x 8 HEMI mask plane, a sub-pattern of $n = 4$ was used, corresponding to a open fraction of $f_e \gtrsim 0.44$ in each 4 x 4 area, while maintaing a total open fraction of $f_e = 0.5$.

$$1 - f_e < \frac{1}{2} + \frac{1}{n \,\mathrm{x}\, n} \tag{5.11}$$

Approximately 10,000 patterns were generated and evaluated for the HEMI mask. Upon implementation of the evolved optimized mask pattern, it was found that some of the opaque elements of the mask coincided with dead or noisy channels in the HEMI front plane. As an unfortunate consequence, the final mask pattern varied from the optimized pattern by a few pixels. The final random mask pattern for HEMI is shown in Fig. 5.20.

5.6.3 Angular Resolution

The angular resolution of a coded-mask instrument is a function of instrument geometry and can be determined from trigonometry as shown in Eq. 5.12, where d is the horizontal spacing between the mask pixels and L is the distance from the mask to the detection plane. For HEMI, the center-to-center distance between planes is 7.5 cm. The lexan casing surrounding each detector gives a horizontal spacing between pixels of 1.4 cm. This yields an angular resolution for HEMI in coded-aperture mode of $\Phi \sim 10.6°$.

$$\Phi = arctan(d/L) \tag{5.12}$$

The separation distance between the two planes was set at 7.5 cm distance as a trade-off between angular resolution in both Compton and coded-mask mode (larger separation distances yield better angular resolution) and Compton efficiency, as decreasing the separation distance between planes yields more Compton scatter events.

5.6.4 Coded-Aperture Imaging

After accumulation of data (build-up of detected photons), the source position must be decoded from the resulting shadowgram. For HEMI this was done by cross-correlating the measured pattern on the backplane with pre-determined patterns from known source locations obtained through simulation. To this effect, far-field mono-energetic sources were simulated at various incident angles within the instrument field-of-view. It was found that rather than running full Monte Carlo simulations for each position, the photoabsorption probabilities could instead be used to deduce the flux distribution on the backplane as a function of the source energy, incidence angle, and interacting materials. The resulting simulated images essentially create a library of patterns that each relate to a specific source location in the sky.

Because the source energy is first determined through spectroscopy, the appropriate mono-energetic source simulations can be pre-selected prior to matching of the patterns. A cross-correlation method is then used to assess the best match between measured and simulated patterns.

5.6.5 Source Measurements

For each measurement in coded-mask mode, the calibration source simulations were performed using the exact geometric configuration and detector response that were used in the measurements (e.g., active/dead channels, threshold settings, etc.). Fig. 5.21 shows resulting images from the cross-correlation method. A source was placed and data acquired at theta = 0°, 10°, then 20° and phi = 0° from the HEMI-96 instrument. The reconstructed images are shown for the 80 keV line ($\pm$ 1.4σ) from a ^{133}Ba source at the three locations, top right and for the 511 keV ($\pm$ 1.4σ) line from a ^{22}Na line, bottom right.

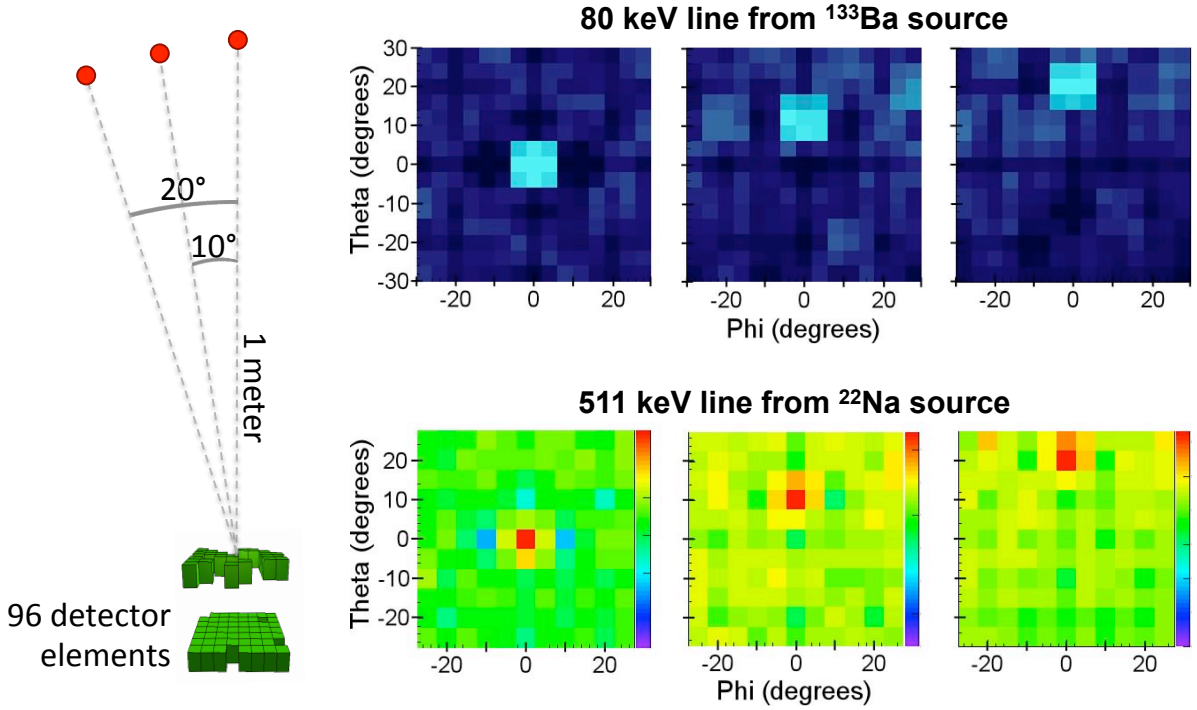

Figure 5.21: An illustration of measured source locations, left, and the resulting images obtained through cross-correlation of the 80 keV line from a ^{133}Ba source, top right, and the 511 keV line from a ^{22}Na source, bottom right.

One can see from Fig. 5.21 that the source location becomes less resolved as the incidence angle of the source increases. As mentioned in section 5.6.1, for the HEMI prototype instrument a fully-coded field of view is only possible for on-axis sources. Because the HEMI mask is the same size as the detection plane, as the incidence angle of a source increases the working zone of the mask is decreased. This results in a projected shadow pattern that is shifted away from the back detection plane, thereby only a partially-coded pattern makes it onto the backplane. This is limiting in that the shadowgram contains only a portion of the mask, thus the projected image is less unique.

5.7 Summary

The HEMI instrument has been successfully calibrated and benchmarked through a combination of measurements and Monte Carlo simulations, achieving good agreement between measurement and simulation and a well-understood detector response. The characterization of the HEMI-96 prototype yielded a system energy resolution of 2.4% FWHM at 662 keV, an angular resolution of 9.5° FWHM at 662 keV in Compton mode, and a 10.6° angular

resolution in coded aperture mode. The HEMI-96 instrument showed a total efficiency of 51% for single-site hits and 8% for Compton events for a 662 keV source, corresponding to effective areas of 32.6 cm^2 and 2.56 cm^2, respectively. After event cuts, the effective area for Compton imaging of the 662 keV photopeak is $\sim$0.1 cm^2. Imaging of point sources in both Compton and coded aperture modes have been demonstrated. The minimum detectable activity of a ^{137}Cs at a 20 m distance with 20 seconds of observation time is estimated to be $\sim$0.2 mCi in spectral mode and $\sim$20 mCi in Compton imaging mode.

Chapter 6

Field Tests

The initial goal of the HEMI project was to demonstrate spectroscopy and imaging capabilities of the prototype instrument in a laboratory environment within the context of developing a scaled-up version for applications in nuclear security. Following the Fukushima Dai-ichi Nuclear Power Plant accident in March of 2011, an urgent need for gamma-ray detection technologies arose in order to assess and ameliorate the clean-up of radioactive contamination. Although the use of CdZnTe detector arrays for the purpose of environmental remediation was initially proposed by *Luke, et al.* (2001), the HEMI prototype was not designed for this application, and the relevance of HEMI for this purpose was unforeseen at the start of the project (2008). However, the instrument design allowed for relatively simple modifications to make it suitable for operations in the field. Through a collaboration primarily with the University of Tokyo, the Japanese Atomic Energy Agency (JAEA), the Furukawa company, U.C. Berkeley, and the Lawrence Berkeley National Laboratory, the HEMI instrument underwent modifications and was brought to Japan in August of 2013 for field testing from an aerial platform within the Fukushima prefecture.

The field testing of the HEMI instrument had two main goals. The first goal was to commission the instrument for use in an outdoor environment in order to evaluate the CdZnTe detector performance in the field, particularly from an aerial platform. The field testing in Fukushima was the first known helicopter deployment of a Compton imaging instrument. The second goal was to evaluate the imaging capabilities of the instrument to localize high activity regions (hotspots) amidst diffuse background contamination. Achievement of the latter goal would demonstrate that aerial imaging, specifically with the HEMI technology, can aid in the environmental remediation of radioactively contaminated land.

This chapter describes the motivation for aerial imaging within the Fukushima prefecture and the technological requirements for this application. The modified HEMI instrument hardware, aerial deployment, and analysis of measured data obtained during the commissioning run of 2013 are described. A summary of the findings along with recommendations for future aerial deployment of imaging instruments are given.

6.1 The Fukushima Dai-ichi Nuclear Power Plant Accident

On March 11, 2011, a 9.0 magnitude earthquake, known as the Great East Japan or Tōhoku Earthquake, occurred off the Pacific coast of Japan, generating a large tsunami and causing extensive damage and loss of life. A 15 meter high tsunami wave struck the area of the Fukushima Dai-ichi Nuclear Power Plant (FNPP), disabling the power supply and cooling systems, causing core meltdown and a series of three explosions at the plant (*World Nuclear Association*, 2014). The explosions resulted in a large-scale release of radioactive material into the environment. The radioactive plume from the plant deposited substantial amounts of radionuclides primarily within a 20 km radius from the plant and extending up to 30 km to the northwest of the FNPP due to winds at the time of the explosions. As a result of the fallout, a government-mandated exclusion zone was declared for public safety, resulting in at least 185,000 people displaced from their homes (*IAEA, Fukushima Nuclear Accident Update Log*, 2011). Additionally, radioactive contamination was detected in food and agricultural products as a result of the fallout. This necessitated the disposal of food in some cases and a halt in the production and distribution of food from affected areas.

Initial surveys to deduce the scale of the contamination revealed dose rates of up to 170 μSv/hr within a 30 km zone surrounding the plant, as detected in the weeks following the accident. Dose rates as high as 400 mSv/hr were reported directly at the FNPP site (*IAEA, Fukushima Nuclear Accident Update Log*, 2011). The increase in background levels detected outside of the 30 km zone (and globally) were below levels considered dangerous for human health. The natural radioactive background varies geographically and with altitude, but as a point of comparison the global average dose rate from background is 2.4 mSv/yr, or 0.27 μSv/hr. The highest reported dose rates (from areas regularly inhabited by humans) range from 40 mSv/yr, or 4.6 μSv/hr, as detected in regions of Brazil and Sudan up to $\sim$30 μSv/hr in Ramsar, Iran (*World Nuclear Association*, 2014).

The primary contaminants released from the plant are shown in Table 6.1. The ^{131}I was of immediate concern because of its deleterious health effects, but due to its short half-life it is no longer present in the environment. The presence of the longer-lived ^{137}Cs and ^{90}Sr isotopes are still of great concern in terms of direct exposure to humans and animals, and also because of their potential to contaminate agriculture and livestock for generations.

Methods to survey and decontaminate the affected regions were implemented shortly after the accident. However, because of the scale of the contamination and the difficulty of the clean-up, nearly 3 years after the nuclear accident the evacuation orders have not been lifted for the affected zones.[1] Monitoring of food, air, and water for dangerous levels of

[1] On April 1, 2014 the first no-entry order was lifted for Tamura, a decontaminated town within the Fukushima prefecture, allowing the $\sim$355 former residents to return to their homes. Tamura is located approximately 20 km west of the FNPP, on the opposite side of a mountain range from the plant. The background levels reported for Tamura at the time the order was lifted ranged from 0.11 to 0.48 μSv/hr (*Reuters*, 2014).

Isotope	Emission	Half-life
^{134}Cs	β, X-ray, γ ray	2.06 yr
^{137}Cs	β, X-ray, γ ray	30.07 yr
^{131}I	β, X-ray, γ ray	8.02 d
^{90}Sr	β	28.79 yr

Table 6.1: Primary contaminants dispersed into the environment as a result of the FNNP accident.

radioactivity are ongoing, and land-use limitations are still in place.

6.2 Decontamination Methods

The goal of decontamination is to reduce the annual dose rates in the affected areas to levels that are acceptable for human habitation and eventually for agricultural use as well. This includes a clear understanding of both the spatial and temporal aspects of contaminants, namely the transport and accumulation of radionuclides in the environment.

The primary target for clean-up in terms of gamma-ray emitters is the longer-lived radioactive cesium. Because cesium binds to clay particles in soil, sample testing found that up to 76% of the contaminants do not leach into soil deeper than 5 cm from the surface (*Tanaka*, 2012). Thus, it was initially concluded that the removal of the top layers of soil, from 5 - 6 cm, would remove the majority of the contamination. Following removal, the topsoil is contained in large bags and stored in fields at or near the Dai-ichi power plant for three years. After this time the bagged soil will be moved to an Interim Storage Facility for a duration of up to 30 years (*IAEA Final Report*, 2013).

Although this method has shown to be locally effective, there are several reasons why it is not ideal. First, removal of the topsoil also removes nutrients from the soil, therefore even after successful decontamination, rehabilitation of the land for agricultural may still be necessary. Additionally, removing the soil from the entire affected region is a labor-intensive and time-consuming process. In areas that are inaccessible, land-use restrictions will still need to be in place. Finally, the mechanisms for transport and accumulation of radionuclides in the environment are not fully understood. Of particular concern is the transport of radionuclides from contaminated zones into areas that have already been decontaminated. For this reason, the localization and clean-up of higher activity regions, i.e. hotspots, before they become dispersed or recirculated in the environment is necessary.

6.3 Motivation for Surveys with HEMI

The clean-up efforts are aided and assessed by handheld counters, spectrometers, and imagers on the ground to estimate the activity within contaminated regions. Methodical ground

measurements can reveal localized changes in background levels both before and after decontamination as well as areas in which the radioactive materials tend to accumulate. However, ground surveys are time consuming and need to be done carefully and with adequate sampling in order to ensure that an area is devoid of hotspots.

Spectrometers are also routinely used for aerial surveys. For these surveys an area is slowly scanned by detectors mounted to Unmanned Aerial Vehicles (UAVs). The acquired countrates at each point are then mapped as a function of position at each point. Interpolation between points (∼5 - 10 meter separation distance) is used to estimate the ground activity. There are several drawbacks to this method. Scanning large areas point-to-point over the entire exclusion zone is a very time consuming process. Additionally, the acquired countrates are associated with just one position corresponding to the GPS coordinates of the helicopter. In reality, the detectors are surveying and accumulating counts from a 4π distribution at each point, as the detectors are unshielded. This induces uncertainties in localizing the areas of accumulation. Also, the interpolation between points allows for localized high intensity regions to become smeared out over a much larger region. The consequence of this is potentially the obscuration of hotspots.

Ideally, one would like to readily localize areas of high contamination in order to prioritize and systematically remove radioactive soil from the most affected regions. An efficient approach to accomplish this goal may be through aerial imaging. Through imaging, the spatial distribution and morphology of radioactive emissions within the entire field-of-view (FoV) of an instrument can be obtained. This could potentially allow for faster assessment and more precise localization of hotspots for each aerial deployment. The existence and imaging of hotspots in Fukushima on the ground was previously demonstrated by the Japanese Aerospace Exploration Agency, JAXA, (*Normile*, 2013, and *Takahashi*, private conversation). Compton imaging from an aerial platform had not been demonstrated prior to the HEMI field tests.

The HEMI instrument was a good candidate for testing the efficacy of gamma-ray imaging from an aerial platform. The instrument demonstrated good energy resolution and imaging capabilities, and the response at 662 keV from ^{137}Cs had already been benchmarked. Because the CdZnTe detectors perform well at ambient temperature, the auxiliary equipment needed to operate the instrument is minimal. The relatively low mass of HEMI (<3 kg) and its low power consumption (∼8 Watts) are within the payload and portability constraints of the UAV that is currently utilized in the Japanese Atomic Energy Agency (JAEA) clean-up program.

6.4 Instrument Preparation and Deployment

In order to prepare the HEMI instrument for operations from an aerial platform, several modifications were made to ruggedize the HEMI assembly, a new hermetically sealed enclosure for the instrument was built, and a secondary environmental chamber was designed and fabricated to house the HEMI auxiliary equipment and to interface with the UAV, specifi-

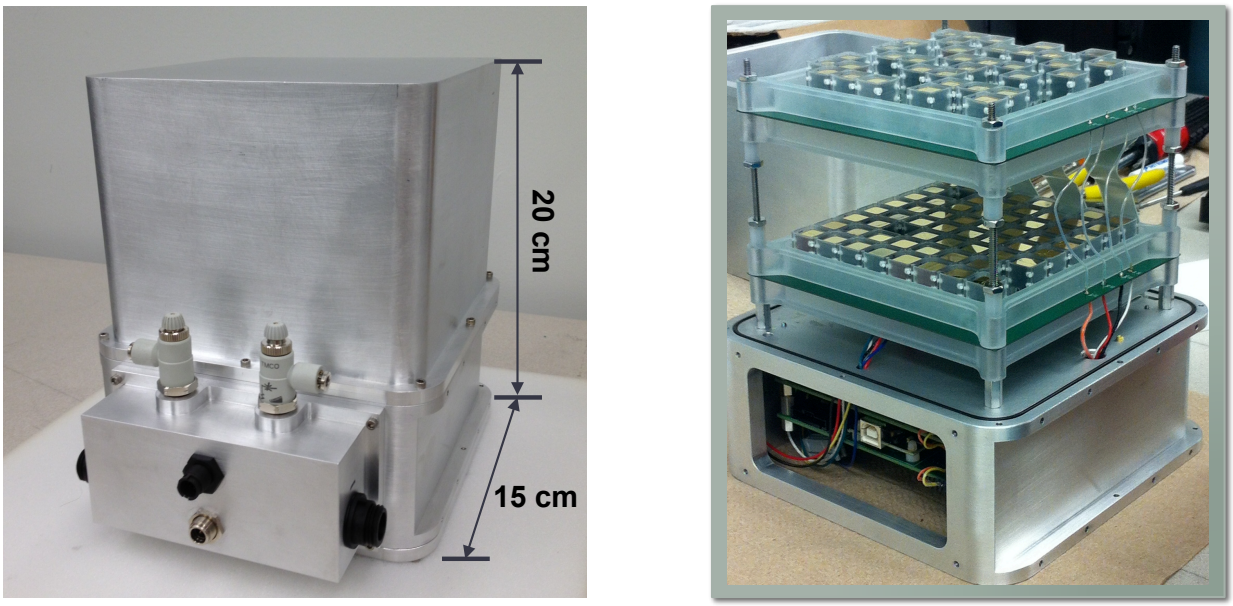

Figure 6.1: The modified HEMI enclosure with ports for dry nitrogen purge, left, and the ruggedized HEMI array mounted to the base of its hermetically sealed enclosure, right.

cally the Yamaha RMAX, mounting hardware. The UAV payload constraints required that the system maintain a low mass (nominally less than 15 kg), a small volume to fit under the UAV with additional bottom clearance, and autonomous power and DAQ systems that allow for portability. Several operational conditions that may affect the detector performance, e.g., temperature, humidity, vibration or other mechanical instabilities were addressed in the HEMI rebuild and chamber designs as well as throughout operations in the field. Finally, imaging and localization tasks were aided by the addition of an onboard camera and a global positioning system.

6.4.1 Hardware Design and Modifications

Fig. 6.1 shows the modified HEMI array within the redesigned enclosure. First, the two-planar configuration was made more rigid by thickening the support rods between planes and by adding teflon stiffeners above and below each of the two motherboards. The array enclosure was redesigned for compactness by reducing the size of the electronics compartment and by shortening the distance between the array and the outer box. The distance between the two detection planes was kept at 7.5 cm. To minimize vibration the HEMI instrument was placed in shock foam mounts inside of the environmental chamber.

High temperatures and extreme humidity were of particular concern for deployment during the summer in Japan. Based on studies showing improved energy resolution of CdZnTe detectors with the application of moderate cooling from 20°C down to -20°C (*Amman*, 2006),

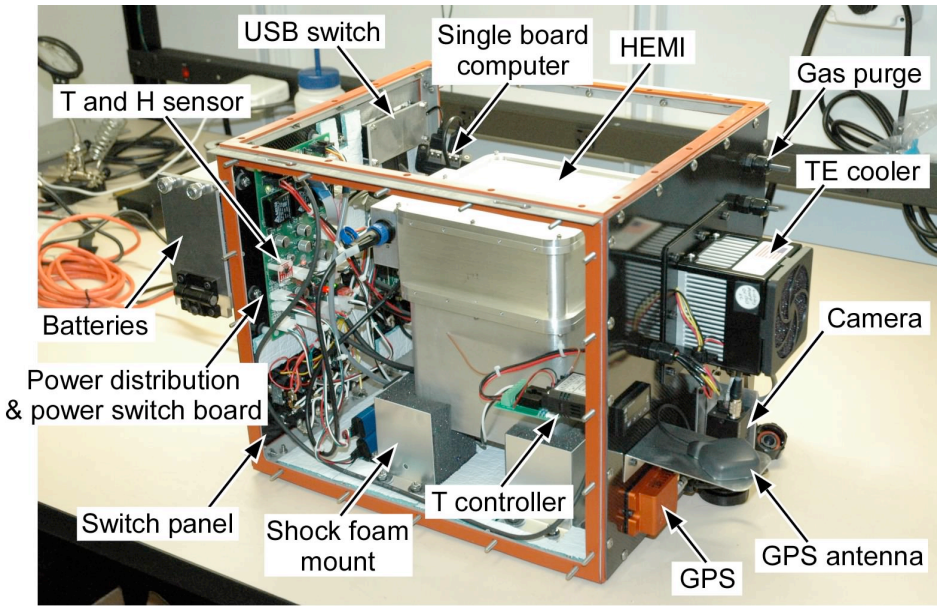

Figure 6.2: The HEMI instrument and auxiliary equipment mounted to the environmental chamber.

degradation of the energy resolution relative to the laboratory environment was anticipated for temperatures exceeding 20°C. High humidity was a concern as it can cause high voltage breakdown, leading to detector damage. Therefore the new HEMI enclosure was designed and built to be hermetically sealed and equipped with ports to allow for a dry nitrogen purge. A temperature and humidity sensor was mounted inside the enclosure underneath the bottom detection plane.

Fig. 6.2 shows the HEMI environmental chamber. A Peltier cooler with a temperature controller and several small fans for circulation were added to the environmental chamber in order to manage the temperature of the enclosed volume surrounding the HEMI instrument. Additionally, mylar was added to the outside of the environmental chamber for optical reflectivity to reduce the temperature from solar heating.

The chamber holds 2 lithium-ion batteries (∼200 Wh), an Aurora PC104 single-board computer with HEMI DAQ installed, and a solid state drive for data storage. A camera, GPS, and GPS antenna are mounted to the outside of the environmental chamber. A schematic of the electrical system and signal distribution is shown in Fig. 6.3.

6.4.2 Operations and Deployment

Individual detector operation, threshold settings, and data acquisition functionality were checked after mounting the outer box to the UAV prior to each take-off as well as immediately upon return. The detectors and the majority of the auxiliary equipment were all functioning

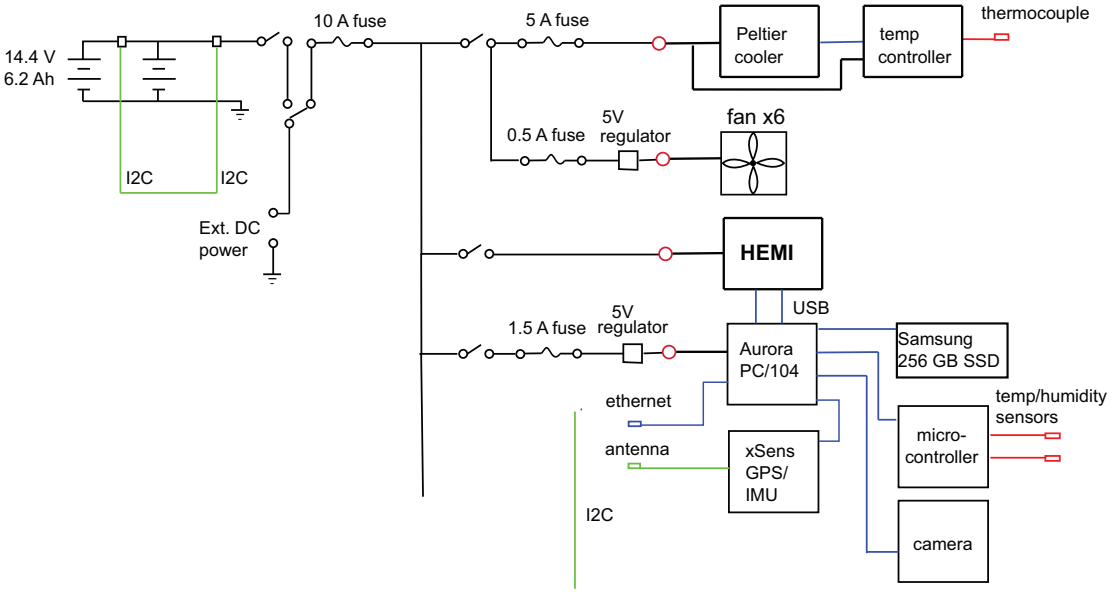

Figure 6.3: The electrical and signal schematic for the portable HEMI system.

properly throughout the measurement campaign. The only design limitation of the auxiliary equipment was that the thermoelectric cooler was unable to compensate for the operational heat load of the system. Care was taken to keep the temperature inside the HEMI enclosure at ambient temperature (∼30°C in the field) during the stationary measurements and in between aerial deployments by venting the box. However the starting temperature inside the instrument enclosure was typically 34°C with an increase of a few degrees over the duration of each flight.

There were two issues with the data acquisition system. First, an unknown halt in the data acquisition system occurred at approximately 10 minutes into the first aerial deployment, although this was a minor concern and did not occur during any of the other measurements. More importantly, fluctuations in the countrates were observed in the acquired data throughout the measurement campaign. This seemed to have an effect on the total output for rates above ∼ 30 kHz. A fluctuation appears in the data once every 3 seconds, and was later found to be a buffering issue in the DAQ multi-threaded software. This issue has since been resolved.

The field tests were conducted in Namie-machi, Fukushima prefecture on August 28th and 29th, 2013. Fig. 6.4 shows measurement sites 1 and 2, located approximately 8 km and 11 km from the Fukushima Dai-ichi Nuclear Power Plant, respectively. The field testing consisted of 3 aerial deployments as summarized in Table 6.2, 2 stationary measurements, and a calibration run. Fig. 6.5 shows the instrument being mounted underneath the UAV, left, and prepared for flight, right. To reliably obtain a signal, the GPS antennae was mounted to the top of the UAV tail during the flights. Fig. 6.6 shows the instrument in flight and its

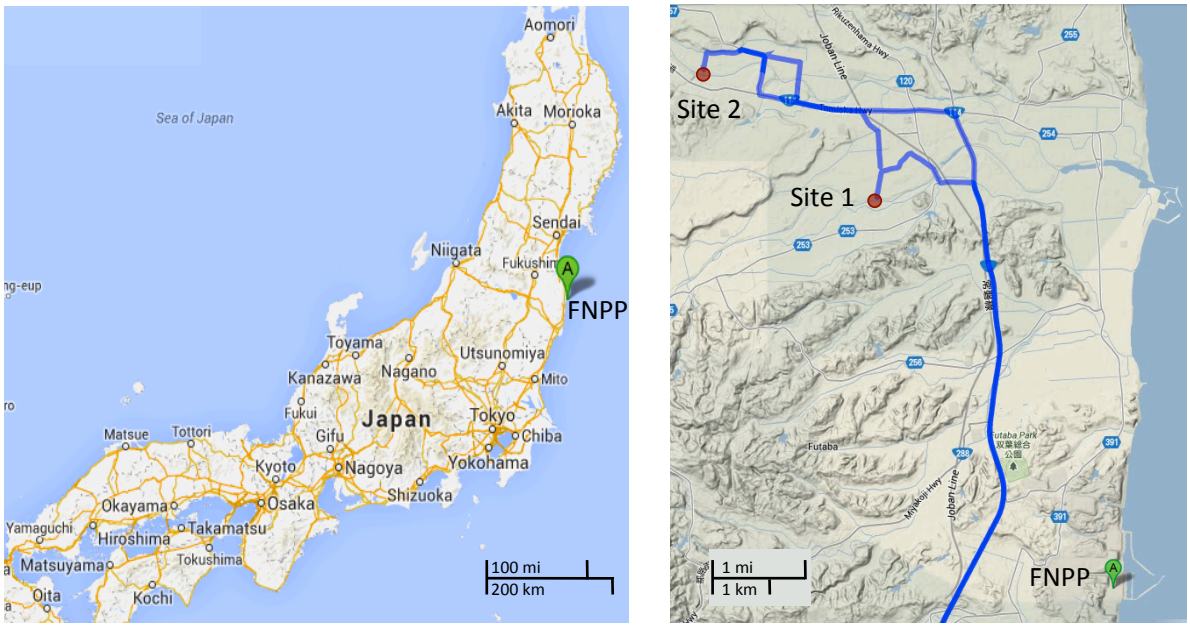

Figure 6.4: Map of Honshu, the main island of Japan, left, and the locations of the 2 measurement sites, right. The green markers indicate the location of the Fukushima Dai-ichi Nuclear Power Plant (FNPP, green marker). The blue lines map the route taken by car to reach the test sites (courtesy Google maps, GPS route courtesy John Kua).

orientation to ground during the Site 1 measurement.

Location	Altitude (m)	Hover (min:sec)	Average Countrate (Hz)
Site 1	10 m	10:45	19,000
	20 m	13:44	24,000
Site 2	10 m	10:30	38,000
	20 m	17:20	32,000

Table 6.2: The aerial hover measurements taken during the HEMI field testing campaign in Fukushima.

6.5 Field Performance

The first goal of the measurement campaign was to evaluate the performance of the CdZnTe detectors and HEMI system in the field. To this end, the CdZnTe detectors performed very well, e.g., without electrical or mechanical failures or atypical noise issues, and exhibited very good spectral performance throughout the measurement campaign. Fig 6.7 shows an example

Figure 6.5: The HEMI instrument enclosure during mounting to the UAV, left, and the Yamaha RMax with the HEMI payload prior to take-off for the first flight measurement, right.

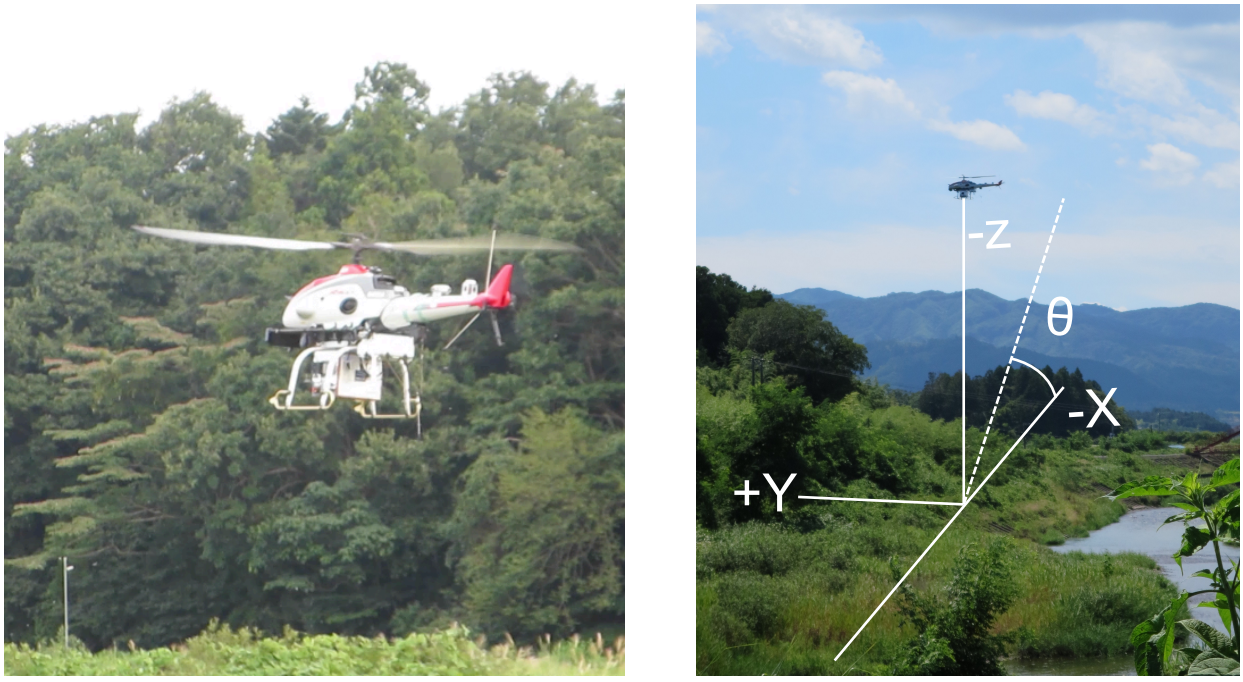

Figure 6.6: The HEMI instrument in flight. Coordinate system with respect to ground during hover measurements at Site 1 is shown, right.

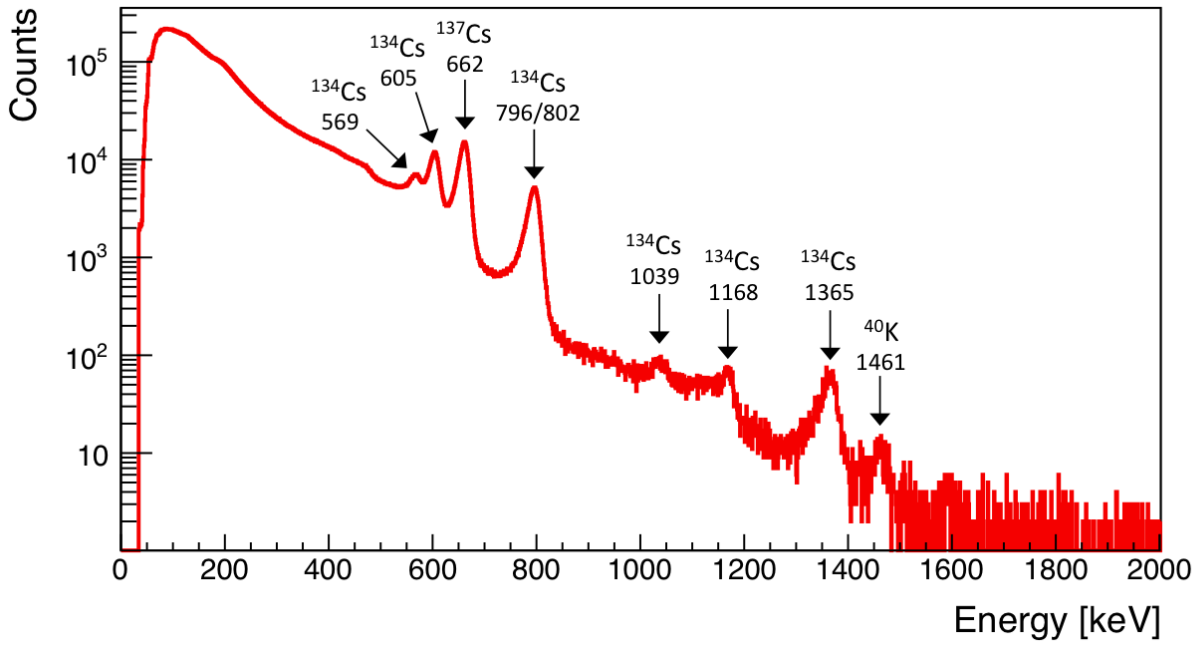

Figure 6.7: Summed energy spectra of the Site 2 measurement at 20 m obtained by the 90-detector HEMI instrument. Prominent isotopes and their respective line energies in keV are labeled.

spectrum from data acquired during the 20 m altitude hover flight at Site 2. Prominent peaks from the ^{134}Cs and ^{137}Cs contamination are labeled, as well as the ^{40}K peak from natural background. The energy resolution at 662 keV varied from 2.5% to 2.8% FWHM as compared to typically 2.4% FWHM as measured within the laboratory environment. This proved the instrument capable of good performance under extreme field conditions (e.g., high temperature, high humidity, mechanical vibration).

6.6 Survey Results

The good spectral performance of the instrument in the field allowed for preliminary analysis of the relative activities and distribution of the cesium contamination at the two measurement sites. In addition to measurements with the HEMI system, additional surveys were conducted using a single CdZnTe spectrometer (manufactured by Kromek), a handheld Geiger counter, and a Hitachi-Aloka TCS-172B NaI handheld spectrometer. For the Aloka measurements, dose rates are adjusted for cesium after background subtraction and measured at a 1 m distance from ground. This instrument was owned and operated by JAEA.

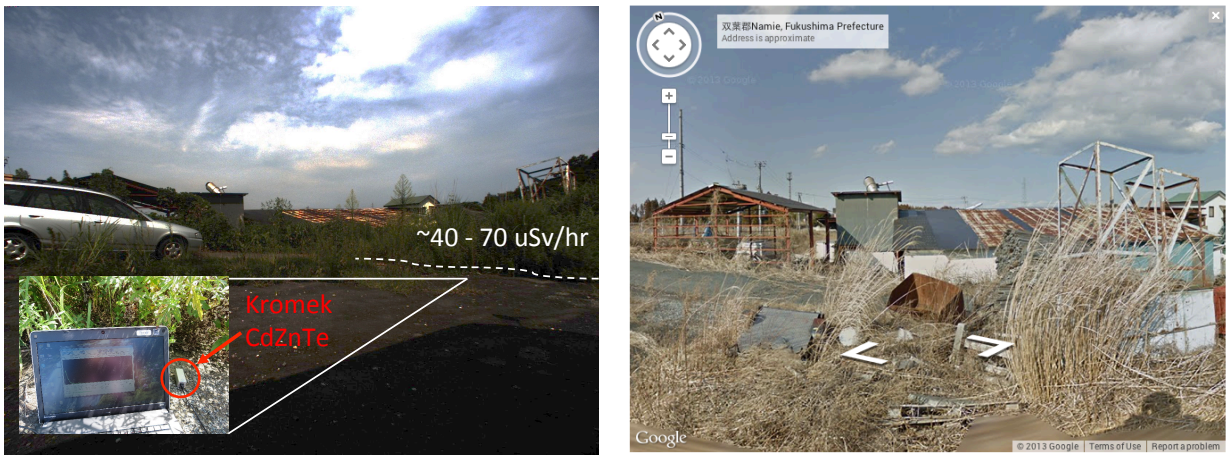

Figure 6.8: Image near the Site 1 staging area taken with the HEMI auxiliary camera, left. Areas of high activity were detected with handheld meters, as indicated by the dashed white lines.The image on the right was taken of the same area using Google Street View Car around March of 2013 (image courtesy Google).

6.6.1 Staging Area Survey, Site 1

The ground activity as measured by personal dosimetry at Site 1 was observed to be 2 - 3 μSv/hr. Upon arrival on-site, the single CdZnTe Kromek spectrometer and handheld Geiger counter were used to survey the area. The survey revealed areas of high activity in the vegetation just a few meters from the staging area. Fig. 6.8 shows one of the surveyed areas, left, with the Kromek instrument and PC, left inset image. The JAEA followed-up these measurements with a survey using the NaI handheld spectrometer, revealing a diffuse area of emission of at least 2 m^2, with dose rates ranging from 40 - 70 μSv/hr.

This first observation of the staging area at Site 1 emphasizes the need for a better assessment of ground activity. Although initial ground surveys and an aerial countrate map of the area using a lanthanum bromide detector yielded dose rates of 2 - 3 μSv/hr (*JAEA*, private conversation), it became evident upon inspection that there were areas within this region that exceeded the averaged readings by at least a factor of 20. It follows that regions of higher activity can easily become obscured through the current survey methods, emphasizing the need for a more effective way of assessing the the true ground activity.

The image of the Site 1 staging area in Fig. 6.8, right, was taken with the Google Street View Car in March of 2013. The images within the no-entry zone were taken to show the effects of the nuclear incident and to allow former residents to see the state of their homes and neighborhoods (*Google "Memories for the Future" project*, 2013). The potential exists for combining the Street View imagery with gamma-ray imaging to allow for a visualization of the level of contamination in the no-entry zones. Although radioactive background distributions and intensities will change over time, to first order the combined

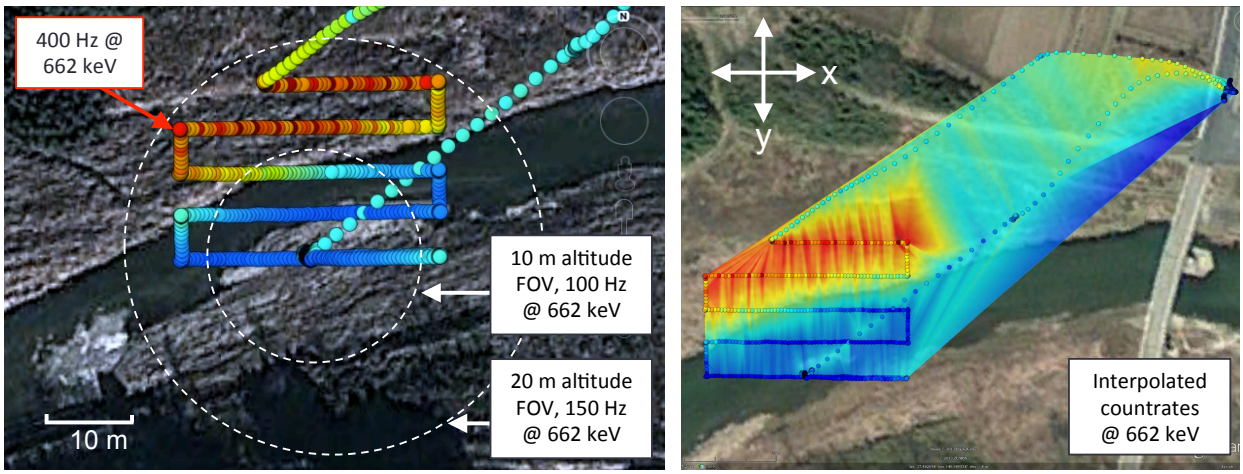

Figure 6.9: Site 1 measurement area: The countrates during a 10m altitude scan are plotted in one second bins to show the relative intensities at each point, right. Red and blue circles correspond to higher and lower countrates, respectively. The dashed circles indicate a 100° FoV for the 10 m and 20 m altitude hover measurements. The right plot shows a linear interpolation between neighboring bins in both the ±x and ±y directions (countrate visualizations courtesy J. Kua, Google Earth).

imagery would be a viable and easily accessible method to inform the public, former residents, as well as radiation workers of areas of higher activity.

6.6.2 Aerial Measurements, Site 1

The two aerial hover measurements at Site 1 took place at approximately the same location near the bank of the Takase River. The measurements were obtained in two separate flights: one at a 20 meter altitude on the first day of the campaign and the second flight at a 10 meter altitude on the second day. Additionally, a point-to-point scan at a 10 meter altitude was performed on the second day, encompassing the Site 1 hover locations and covering a ground area of approximately 500 m^2. Fig. 6.9 shows the results of the scan and the countrates obtained during the two hover measurements. Each circle represents accumulated counts over 1 second. Red circles correspond to higher countrates (peak is ∼400 Hz) and the dark blue circles are relatively low activities. The dashed circles indicate a 100° FoV, corresponding to the approximate Compton acceptance angle for HEMI given a plane-to-plane separation distance of 7.5 cm. The locations of the hover measurements are at the center of each respective circle (the two hover locations were slightly offset from one another, hence the circles are not exactly concentric).

As indicated in Fig. 6.9, left, the countrate from the 10 meter altitude measurement was approximately 30% lower than the countrate at 20 meters. It is expected that for uniform

background emission, a change in altitude would not change the flux due to geometric effects alone. An increase in the solid angle at higher altitudes corresponds to an increase in the observed area. In the case where the altitude is doubled, the area of the ground seen by the instrument increases by a factor of 4. However, since the distance to the ground has doubled, the flux from any given patch will have decreased by 1/4. Thus a change in flux as a function of altitude is not expected under the assumption of uniform background emission. Additionally, attenuation of the flux through atmospheric absorption should cause a decrease in flux at higher altitudes. Therefore, the increased countrate at the higher altitude implies that the background is nonuniform.

The observed increase in countrate as a function of increasing altitude occurs at Site 1 for primarily 2 reasons. First, one can see from Fig. 6.9 that the river figures more prominently in the FoV of the lower altitude. The river is expected to have little or no activity, as the contamination is expected to have washed away, and any contamination that may be settled at the bottom of the river would be significantly attenuated by the water. However, the difference in area occupied by the river in the FoV is only $\sim$5%. The second difference can be seen in the countrate scan map, as it appears that the ground had a much higher relative activity on the opposite side of the riverbank than at the hover locations. The maximum countrate over what appears to be diffuse emission, indicated in red, was approximately 400 Hz at 662 keV. This active region was outside of the FoV at 10 m, but detectable during the 20 m altitude measurement. Additionally, it is plausible that the area outside of the 10 m FoV and on the same side of the riverbank as the hover sites also had a higher activity. This nonuniformity detected at only the higher altitude seemingly accounts for the unexpected increase in flux with increasing altitude for the Site 1 measurements.

Fig. 6.9, right, shows a 2-dimensional countrate distribution derived from the Site 1 scanning survey at a 10 meter altitude. The smeared lines are an interpolation between the countrates at each 1 second bin and its two nearest neighbors in the $\pm$ x and $\pm$ y directions (*Kua*, private conversation). One can see an inconsistency in the distribution which appears to be fluctuations in the countrates from one 1-second bin to the next. From the GPS data acquired during the scan, the helicopter velocity and altitude were very stable. This was later found to be a result of the buffers set too low in the HEMI DAQ software. This issue was resolved for future measurements, but unfortunately affected the data quality of the initial field tests.

6.6.3 Ground Measurements, Site 1

On the end of the second day of measurements, ground truth of the Site 1 hover locations was obtained by the JAEA members, as shown in Fig. 6.10, left, using the handheld Hitachi-Aloka NaI spectrometers. These measurements revealed dose rates ranging from 2 - 3 μSv/hr, i.e. the same dose rates as the diffuse background emission in the region. Additionally, Fig. 6.10, right shows a Google Earth image of the Site 1 area obtained several days after the FNPP explosions. The hover sites, indicated in yellow, were nearly underwater at that time, so it is

Figure 6.10: The JAEA members obtaining ground measurements at the Site 1 location using handheld meters, left. The image on the right shows the Site 1 area nearly underwater a few days after the explosions in March, 2011 (image courtesy Google Earth).

likely that the area was either not directly exposed to the initial plume, or any high-activity contamination was washed away shortly afterwards.

Given the ground truth measurements and Site 1 history in combination with the results from the aerial scan, it appears that the Site 1 hover measurements did not include regions of higher activity, aside from the diffuse emission on the periphery of the 20-meter altitude FoV. This distribution, including the high activity region on the opposite bank, was later confirmed through aerial measurements using a scintillator-based instrument (*Shimazoe*, private conversation).

6.6.4 Aerial Measurements, Site 2

Two hover measurements at altitudes of 10 m and 20 m were performed at the Site 2 location. The data was acquired during the same helicopter flight. In both measurements, the instrument was centered above the same location on the ground. Fig. 6.11, right, shows a 100° FoV for each of the two measurements. Fig. 6.11, left, shows a visualization of the countrates at the 10 m and 20 m altitudes. The low-activity point of take-off and landing can be seen by the blue vertical bins. Contrary to the measurements at Site 1, at Site 2 the countrate decreased as a function of altitude by $\sim 22\%$.

By the inverse-square law, the photon flux at higher altitudes decreases by $1/\mathrm{H}^2$, where H is the altitude, i.e. the on-axis distance from the ground to the detector. Thus a factor of 2 increase in altitude leads to a factor of 4 decrease in flux. However, as the solid angle of detection remains the same with increasing altitude, the area of ground observed by the detector increases by a factor of 4 for a factor of 2 increase in altitude. Therefore, to first order the incident flux on the instrument from a uniform background remains constant as a function of altitude.

Due to atmospheric absorption, however, the incident flux is lower at higher altitudes. Taking into consideration photon attenuation over the solid angle of detection, the resulting flux can be described by Eq. 6.1, where the flux F, integrated over the solid angle, depends on the photon energy E, the angle of incidence θ, and the altitude H. An assumed uniform background activity is given by B, and λ is the mean free path of photons through a medium. For, e.g., 662 keV photons in air, the mean free path is $\lambda \sim 100$ meters. Eq. 6.1 can be solved numerically (trapezoidal method) for a 100° FoV and 662 keV photons. The solution under the assumption of a uniform background yields a difference in flux of less than 2% between 10 m and 20 m altitudes. Therefore, the detected 22% difference in countrate as a function of altitude at 662 keV implies that the background at Site 2 is not uniform. In this case the higher countrate at the lower altitude may indicate the presence of a hotspot that is closer to the center of the FoVs and visible from both altitudes.

$$F(\theta, E, H) = 2\pi B \int cos\theta e^{(-H/\lambda cos\theta)} d\theta \tag{6.1}$$

For a hotspot directly on-axis, photon attenuation at 662 keV accounts for a difference in flux of ∼10%. One can see from Fig. 6.11, left, that the higher activity region extends for at least 10 meters along the river bank. For these reasons, one can conclude that the region of higher activity is also diffuse. Unfortunately, ground truth for the Site 2 hover area was not obtained. As the Site 1 activity measured at 10 meters (100 Hz) roughly corresponds to the activity of the diffuse background emission at 662 keV, the activity at Site 2 observed at a 10 meter altitude (310 Hz) must be approximately 3 times higher than the background.

6.7 Preliminary Compton Image Reconstruction

As Site 1 did not contain any hotspots aside from a diffuse region on the periphery of the 20 meter altitude measurement, the following preliminary image reconstruction will focus on obtaining an image from the Site 2 measurements. As with the characterization of HEMI in the laboratory, individual hits are first grouped together as Compton events based upon a coincidence window. The events are reconstructed, and the resulting signal-to-noise ratios are evaluated at each altitude. Following appropriate event cuts and a correction for the geometric efficiencies of the instrument, a preliminary gamma-ray image is obtained of Site 2.

6.7.1 Coincidence Timing

For the 10 meter and 20 meter Site 2 measurements, a coincidence search was applied to the data based upon a 2.5 μs time window between adjacent detector hits, as described in Chapter 5, Section 4.1. From the time histograms as shown in Fig. 6.12 one can immediately see that the grouped events are dominated by chance coincidences from the high activity background. This poses a problem for image reconstruction, as the majority of the reconstructed

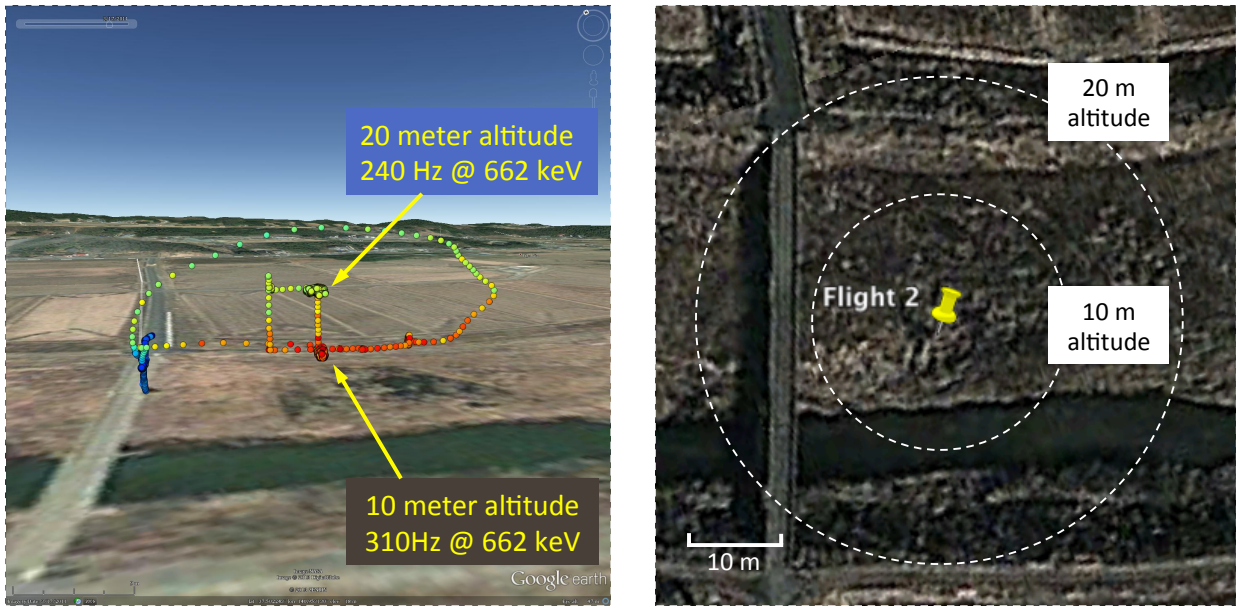

Figure 6.11: Site 2 measurement area: The countrates during travel and at the 10m and 20 m altitude hover measurements are plotted in one second bins to show the relative intensities at each point, left. Red and blue circles correspond to higher and lower countrates, respectively. The dashed circles, right, indicate a 100° FoV for the 10 m and 20 m altitude hover measurements (countrate visualizations courtesy J. Kua, Google Earth).

Compton events will be false coincidences. The true to chance coincidence rate for events within the coincidence window is approximately 1:3 for the 20 meter altitude measurement and 1:4 for the measurement at 10 meters.

6.7.2 Energy Reconstruction

Following the coincidence search, the chance and true Compton events are reconstructed. At the stage of analysis, some of the false coincidences can be eliminated through CSR in combination with photoabsorption and scattering cross-sections. Fig. 6.13 shows the reconstructed energy spectrum of the most prominent ^{137}Cs and ^{134}Cs peaks. At each altitude, the signal-to-noise (SNR) ratio was estimated for the 662 keV photopeak ($\pm$ 1.4σ). The peak to background ratio was slightly worse at 10 meters, 1:4, as compared to 20 meters, 1:3. For this reason, Compton image reconstruction of the 20 meter altitude measurement at Site 2 will be described below.

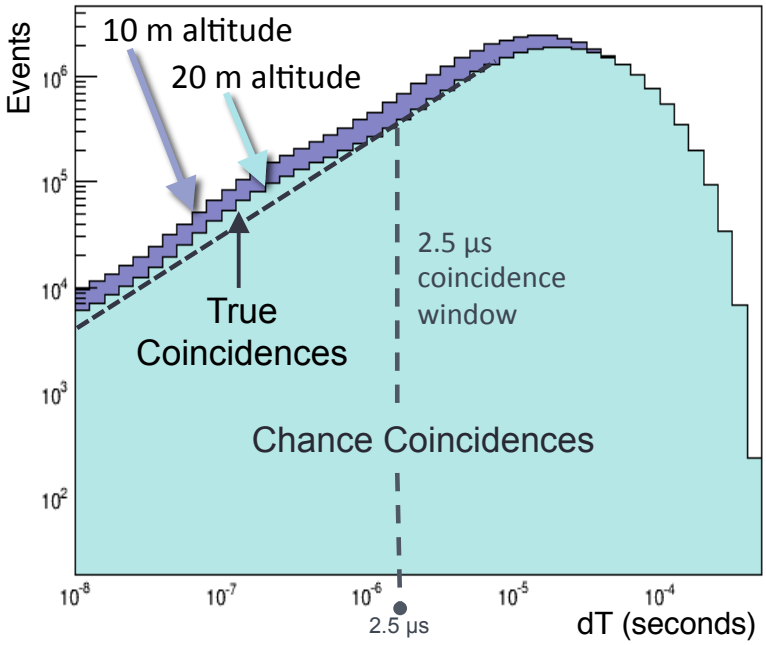

Figure 6.12: Difference in time between adjacent detector hits for the site 2 measurements. At altitudes of 10 meters and 20 meters, the true:chance coincidence ratio within the 2.5 μs window was 1:4 and 1:3, respectively.

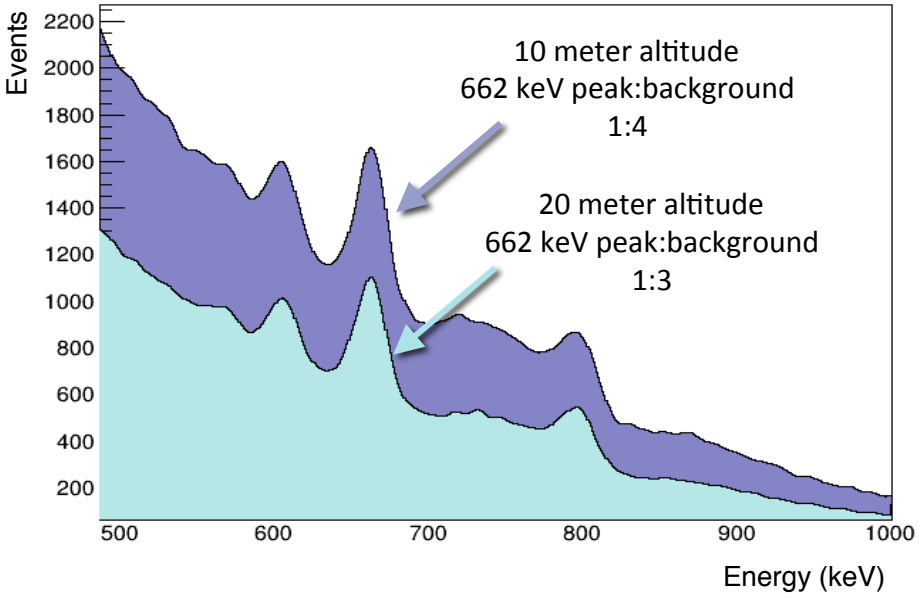

Figure 6.13: The prominent peaks in the reconstructed energy spectrum for Site 2 at 10 meter and 20 meter altitudes. The peak to background ratio for each measurement is indicated.

6.7.3 Image Reconstruction

Because of the geometry of the HEMI prototype (2 square detector arrays, as opposed to a spherical array, for example) the detection and imaging efficiencies vary as a function of incidence angle. In order to correct for this, simulations were performed using a spherical far-field 662 keV source incident upon the HEMI instrument in vacuum. The efficiency correction was then applied to the reconstructed image from the Site 2 measurement at 20 meters. Fig. 6.14 shows the corrected, backprojected image overlaid onto an aerial view of Site 2 from Google maps. As the MLEM imaging algorithm is tuned for convergence onto a point source, events which may reflect the actual diffuse emission are redistributed. As we expect the source to be diffuse, backprojection is used in this case.

In Fig. 6.14, the shading from dark blue to red corresponds to a factor of 8 increase in intensity. Given that the angular resolution of HEMI at 662 keV allows for a resolution on ground of 3.3 meters from a 20 meter altitude, it should theoretically be possible to image the interface between the higher activity riverbank and the cold river. One can see from Fig. 6.14 that the image reveals slight differences between the land and the river. Future improvements in HEMI imaging, which are beyond the scope of this work, will need to enhance this difference further.

It is noted that a correction for attenuation of photons emitted from a planar source as a function of incidence angle would more accurately represent the detection scenario, providing a more complete efficiency correction. However, the difference in attenuation of 662 keV photons on-axis as compared to the edges of the FoV at a 20 meter altitude is $<10\%$. Additionally, accounting for photon attenuation would provide a symmetric correction. In the case of locating a hotspot at Site 2, an asymmetric distribution is expected due to the location of the river relative to the hover spot, thus the photon attenuation has little effect on correcting the source distribution.

In addition to the regular geometric cuts and energy cut applied to the reconstructed event data prior to imaging, several other event cuts were attempted in analyzing the field measurements. These included, e.g., different geometrical cuts, the use of smaller coincidence time windows, the inclusion of the ^{134}Cs photopeaks, subtraction of an off-peak reconstructed image to eliminate background, but none of these selections had a noticeable effect on the final image quality.

Additionally, simulations were performed using a terrain map resembling the Site 1 area. The simulated background was uniformly distributed with the same true-to-chance coincidence ratio as seen in the 20 meter altitude measurement. The reconstructed images from simulations did not reveal a prominent interface between the land and the river.

The preliminary Compton imaging results are promising as some differentiation can be seen between the river and the land. However, it is evident that more information with greater reliability was obtained through countrate scans than through imaging, given the present HEMI technology and configuration, choice of measurement sites for the commissioning run, and image reconstruction method.

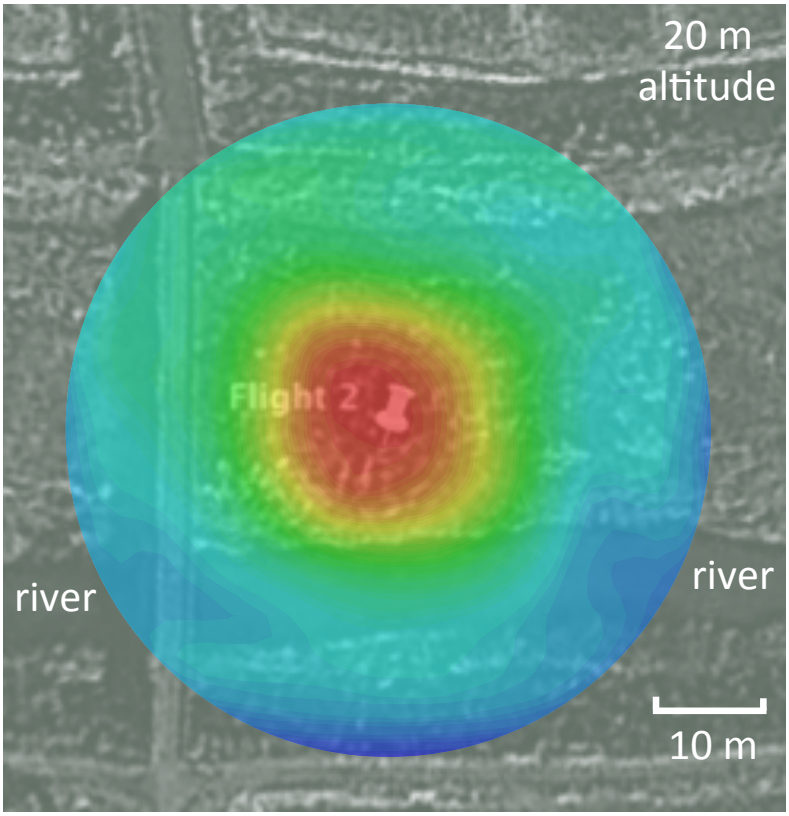

Figure 6.14: Image reconstructed from the Site 2 measurement at a 20 meter altitude. The Compton reconstructed image is overlaid onto a geographic map of the site (courtesy Google).

6.8 Challenges to Imaging in the Field

The characterization of the HEMI instrument in the laboratory focused on imaging of far-field point sources within a low-activity background environment. For the field measurements, there exists several apparent differences that make imaging much more challenging.

Predominately, the relatively low background activity in the laboratory did not create many chance coincidences. In the field, however, the Compton reconstructed events are dominated by chance coincidences, as the background rate increased by at least a factor of 100. Additionally photons arrive at the instrument from essentially a 4π FoV. In the absence of shielding (primarily due to payload limitations in the current UAV program), the background hits can only be filtered out through event selections. This high rate of false coincidences was perhaps the biggest challenge to creating accurate images.

The diffuse distribution of both the sources and the background was also a primary challenge to successful imaging. Localization of a point source allows for reconstructed Compton cones to overlap in one specific location corresponding to the origin of the photons. In the case of diffuse emission, the Compton cones overlap in many places, as this reflects

the distribution of the source. However, either a very good SNR is needed to reconstruct a region of emission, or a FoV that is much larger than the active region. Because the FoV was not much bigger than the source emission, the concentration of Compton circles dominated and passed through the FoV.

Issues such as the buffer overload, appropriate choice of a measurement site, and complete ground truth measurements including larger area scans over the hover sites will be addressed prior to another field run with the HEMI instrument. Different imaging techniques are currently being to developed to better adapt to the specific detection scenarios of the HEMI field tests, e.g., alternative maximum likelihood and filtered backprojection methods (*Haefner*, private conversation). Furthermore, as coded-mask imaging is not relevant for this application, the instrument should be optimized for Compton mode, e.g., if confined to an open fraction of 50% in the top array, a checkerboard pattern would allow for a more uniform FoV and better Compton efficiency. Due to limitations within the HEMI program, changes to the detector array were not possible prior to the field measurements.

For future aerial measurements, several recommendations can be made based upon the HEMI commissioning run:

- Detectors with a faster response would reduce the coincidence window, thus eliminating many of the chance coincidences prior to event reconstruction. A faster response could theoretically also accommodate much higher countrates, although the countrate issue for HEMI was not limited by detector deadtime. Scintillators, for example, would be a good choice, especially high-Z materials with nanosecond time response such as the GAGG scintillator (*Kamada*, 2011).

- A Compton camera with a larger FoV and less geometric biases could more accurately image the ground distribution. A half-sphere geometry with a back absorbing plane would be a good choice (*Zoglauer*, 2010).

- Better detector energy resolution would increase the signal-to-noise ratio. For germanium this would be a trade-off between energy resolution and simplicity/ease of operation. A silicon tracker in front of an absorber plane, such as the JAXA field instrument as described in Chapter 2, may be a good choice for future aerial measurements, as they have good energy resolution (see Chapter 7.3.1) and do not require cooling.

- An improved angular resolution would allow for more precise differentiation between hot and cold areas in the imaging. For the HEMI instrument, the 1 cm^3 position resolution is the biggest limiting factor in obtaining good angular resolution.

6.9 Summary

Field testing proved the HEMI instrument capable of good spectral performance, e.g., 2.5% - 2.8% FWHM at 662 keV, even under conditions of high temperature and high humidity.

Additionally, helicopter deployment of a Compton imaging instrument was demonstrated for the first time. Initial surveys emphasized the need for better assessment of background activities, as hotspots can easily become obscured through the current methods. The high rate of false coincidences from the background as well as the small, uneven field-of-view effect were the main factors that limited the imaging capabilities of the instrument. Aerial imaging has the potential to provide source localization to aid in the Fukushima clean-up, however future tests would benefit from the use of instruments with faster response and a larger field-of-view.

Chapter 7

A CdZnTe-based Telescope for Gamma-ray Astrophysics

The highly penetrative nature of gamma rays allows for a unique probe into the most violent explosions and dynamic sources in the universe. Gamma-rays are emitted as a result of, e.g., radioactive decay of elements produced from nucleosynthesis in supernovae and non-thermal processes in pulsars and black holes. Observations in this energy regime can help us to understand the nuclear, magnetic, and gravitational forces that are present within astrophysical sources and events that lead to the emission of gamma rays.

A next generation telescope in the medium-energy gamma-ray regime requires good energy resolution for the study of line emissions resulting from Galactic nucleosynthesis. Good angular resolution is needed to resolve point sources, thus providing a means to correlate gamma-ray emission with sources that are seen in other wavebands. Additionally, a telescope must have good efficiency and a high sensitivity to detect and image sources above a complex background.

This chapter explores the use of the HEMI CdZnTe detectors and the multimode imaging concept towards a design of a future gamma-ray telescope. The HEMI CdZnTe detector response is well understood after successful benchmarking with laboratory measurements. With a benchmarked detector model, through simulation one can arrive at reliable performance predictions of scaled models, such as a next generation gamma-ray telescope. For future medium-energy gamma-ray telescopes, CdZnTe offers several advantages such as its high-Z for good absorption, large volume detectors for simplified electronics, and little or no cooling requirements, thus allowing for reduced background due to minimization of passive material surrounding the instrument.

The multimode imaging concept is also relevant for the design of a new telescope. Compton telescopes such as COMPTEL and NCT (see Chapter 2) have demonstrated good imaging capabilities in the medium-energy gamma-ray regime, for example, the all-sky map of ^{26}Al by COMPTEL (*Oberlack*, 1996) and the image of the Crab Nebula by NCT (*Bandstra*, 2011). The high sensitivity needed for an astrophysical instrument can be achieved through the capabilities of a Compton telescope with regards to its background rejection capabilities

and as a result of excellent energy, position, and timing resolution. Furthermore, adding a coded mask to a Compton telescope can significantly improve its angular resolution far below the Doppler limit within, e.g., a small area of its field-of-view.

A preliminary study of a combined Compton and coded aperture telescope that utilizes an array of double-sided silicon strip detectors (DSSD Si) as Compton scatter planes and the benchmarked HEMI CdZnTe detectors as absorbers, referred to as "Space HEMI", is described in this chapter. A passive mask covering a narrow (10°) FoV is added to the Compton telescope in order to improve the on-axis angular resolution for dedicated observations. Through simulations of sources in the energy range between 200 keV and 6 MeV, an initial assessment of the achievable energy resolution, angular resolution, and effective area is given. The sensitivity for line sources and a continuum source is estimated based upon the expected background in a low-Earth orbit. Additionally, localization of two 511 keV point sources separated by 0.2° is demonstrated using combined Compton and coded-aperture imaging modes.

7.1 Science Objectives

As described in Chapter 1, the observation of astrophysical gamma rays can provide a deeper understanding of the physical processes that take place in objects such as massive stars, supernovae, novae, pulsars and black holes. The observation of nuclear lines and their properties, such as spectral shape, intensity, temporal variability, and spatial distribution allows for insight into the physics that occurs in stellar evolution, particularly during the stages where stellar transformation results in nucleosynthesis. These nuclear lines come from, e.g., ^{26}Al in star-forming regions, young supernovae remnants such as ^{44}Ti, and the production of ^{60}Fe in massive stars (*Diehl*, 1998). The observation of ^{56}Co line emission would allow for a better understanding of SNe Type Ia explosion mechanisms. This is a key scientific objective as SNe Ia are considered standard candles and inform much of what we know about dark energy, although their explosion mechanisms are not well understood. The observation and study of the nuclear deexcitation lines from ^{12}C and ^{16}O can yield information about cosmic rays and the composition of the interstellar medium (*Bloemen*, 1999). Finally, the primary focus of this study is on the 511 keV line from positron emission in the galaxy. An excess of 511 keV emission has been observed within the Galactic Center (GC), however the origin of the positrons is still unknown (*Knödelseder et al.*, 2005). The ability to make high resolution measurements, i.e. angular resolution of $<1°$, of the Galactic Center is needed in order to gain a clearer picture of the intensity and morphology of this emission, i.e. to resolve possible point sources of positron emission and to provide a correlation between the 511 keV spatial distribution and other known astrophysical objects in the GC region. In addition to nuclear line science, the study of continuum sources, e.g., the Crab pulsar, AGN, compact objects, and GRBs, is a also a key scientific objective in medium-energy gamma-ray astrophysics.

7.2 Telescope Design

In order to improve upon past and current observations in medium-energy gamma-ray astrophysics, several factors need to be considered in the design of a next generation telescope. The telescope must have good energy resolution to allow for accurate nuclear line shape analysis. Good angular resolution is needed in order to resolve and accurately locate potential point sources while remaining sensitive to diffuse emission. A wide field-of-view would allow for uniform sky coverage and sensitivity to transient sources. Additionally, a large effective area and background rejection capabilities are needed in order to achieve a high sensitivity.

For nuclear line emission such as the 1809 keV line from ^{26}Al and the 511 keV annihilation line, excellent energy resolution is needed for optimizing the signal-to-noise ratio and for obtaining accurate narrow line spectroscopy. Broadened lines such as emissions from ^{56}Co, ^{44}Ti, and molecular de-excitation require energy resolutions that are finer than the amount of broadening, i.e. 2 - 3% is generally adequate. As described in Chapter 1, relativistic effects that occur during the production and interaction processes of these lines create distinct shapes that can indicate red or blue-shifted sources as well as lines that are broadened with multiple components. Thus the ability to resolve these shapes is a necessary component to understanding the underlying physics of these sources.

Compton telescopes typically are capable of only moderate angular resolution, i.e. on the order of a few degrees. A Compton telescope design that includes a coded mask can improve upon this at lower energies by at least a factor of 10. Because the angular resolution of a coded-mask instrument is based entirely upon geometry, the achievable angular resolution is not limited by the energy resolution or by Doppler broadening. The addition of a mask would allow for point source localization, which is important for areas in the sky that are dense with objects, such as the Galactic Center.

The coded mask can be designed to occupy only a small area of the telescope FoV. This would allow for pointing capabilities and localization of point sources without limiting the flux in the wider FoV. Since the narrow FoV mask obscures only a small part of the sky, the Compton telescope can observe the rest of the sky in normal Compton mode, as many science targets require only moderate angular resolution. The uniform sky coverage as a result of the wide FoV would allow for all-sky surveys of continuum sources, transients, and diffuse emission, e.g., pulsars, AGN, GRBs, and Galactic diffuse emission from ^{26}Al and ^{60}Fe.

In terms of achieving high sensitivity, the most important factor for telescopes in the medium-energy gamma-ray regime is the ability to prevent and reject background events. This can be achieved through detector design, such as limiting the amount of passive material in an instrument, by using measurement techniques that allow for background rejection, such as Compton reconstruction, and by applying appropriate event selections to improve the signal-to-noise ratio.

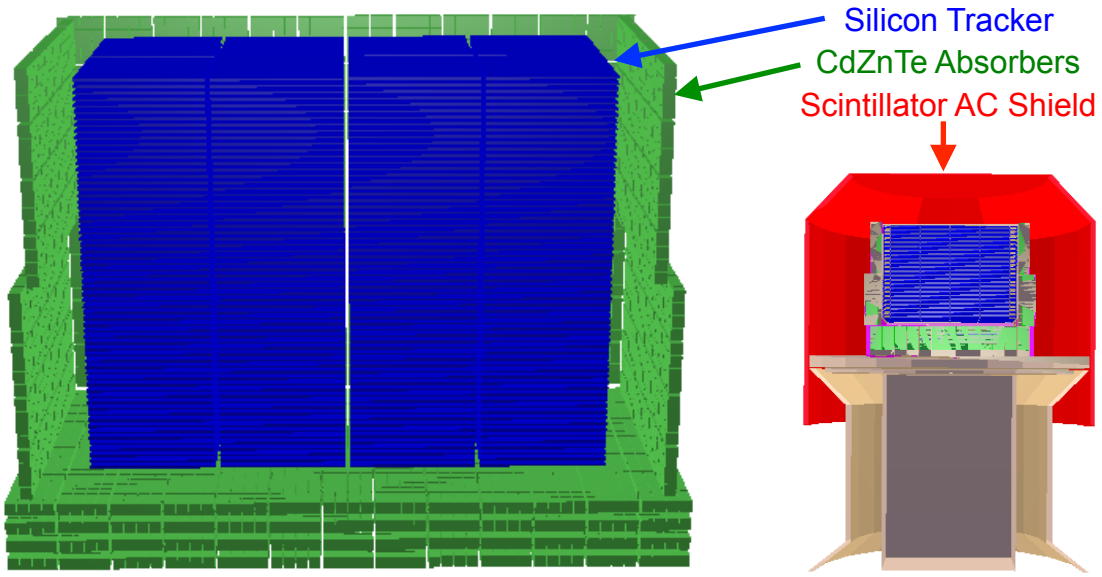

Figure 7.1: Left: Geomega mass model of Compton telescope consisting of a silicon tracker array (blue) and CdZnTe absorber planes (green). Right: Mass model of Organic scintillator anti-coincidence (AC) shield surrounding tracker and absorber detectors.

7.3 Space HEMI

The proposed design of Space HEMI consists of a silicon tracker in which the first Compton interaction takes place, a CdZnTe absorber surrounding the tracker on 5 sides, an organic scintillator used as an anti-coincidence shield for charged particles, and a passive coded mask comprised of tungsten pixels above the tracker. Additional passive materials such as detector electronics, a frame for the tracker, and additional support structures for the telescope were included in the model. The mass model for the Compton telescope is shown in Fig. 7.1, left, with the silicon tracker shown in blue and the CdZnTe elements shown in green. The right image shows the telescope mounted on a support structure and surrounded by the anti-coincidence (AC) veto dome, red. The total mass of the proposed Space HEMI instrument with support structure and shielding is ∼530 kg. This mass is feasible for a Mid-sized Explorer (MIDEX) NASA mission.

7.3.1 Silicon Tracker

The Compton tracker consists of multiple layers of double-sided silicon strip detectors and is based upon the Gamma-Ray burst Investigation via Polarimetry and Spectroscopy (GRIPS)

telescope (*Greiner*, 2008 and *Zoglauer*, 2008). A low-Z material such as silicon (Z=14) is a good choice for a Compton scatter plane, as an incident photon can scatter many times in the tracker before becoming fully absorbed. These multiple interactions allow for improved background rejection. Additionally, low-Z materials such as silicon have a smaller contribution from Doppler broadening to the angular resolution as well as a higher Compton cross-section (relative to its photoabsorption cross-section) as compared to medium-Z to high-Z materials such as Ge and CdZnTe. The simulated detectors have an energy resolution of 1 keV FWHM over a 0.2 to 10 MeV energy range and a 0.5 mm strip pitch, allowing for a telescope with good overall energy and angular resolution. Noise and trigger thresholds of 5 keV and 10 keV, respectively, were used in the simulated performance parameters.

Each silicon wafer is 10 by 10 cm wide with 0.5 mm wide strip electrodes on the top and bottom of the silicon material. The top strips are orthogonal to the bottom strips in order to obtain x-y position information for each interaction. The position resolution is given by the 0.5 mm strip pitch of the silicon detectors. Several wafer thicknesses were simulated to optimize the angular resolution and effective area at 511 keV before arriving at a thickness of 2 mm.

The tracker consists of 4 by 4 wafers, yielding a total geometric surface area of 1600 cm^2. As with the GRIPS telescope, 64 layers of wafers were used (1,024 total Si detectors) with the spacing between layers set to 0.5 cm in order to provide a high Compton efficiency over a wide FoV. The total mass of silicon in the tracker is ∼50 kg.

7.3.2 CdZnTe Absorbers

For Space HEMI, the lanthanum bromide calorimeters that were used in the GRIPS design were replaced with 1-cm^3 coplanar-grid CdZnTe detectors. The large volume, ambient-temperature CdZnTe detectors have the advantages of simplified electronics, low power consumption, a high active to passive material ratio, and a high average Z ($Z_{ave} = 49$), making them an ideal candidate for a Compton telescope absorption plane. The CdZnTe detector response and performance is based upon the benchmarked HEMI detectors. The energy resolution of the highest performing CdZnTe detector was used in this case, i.e. 1.5% FWHM at 662 keV, as a reasonable approximation of the obtainable energy resolution over a long-term production phase. A benchmarked time resolution of 0.5 μs was used in the simulation.

The absorber planes consist of a single layer of 7200 elements surrounding the tracker on 4 sides and a 52 by 52 array of elements 4 layers deep underneath the tracker (10,816 elements). The number of layers surrounding the tracker on all 5 sides was varied in simulation in order to optimize for full absorption of high-energy photons without having excessive detector material. The final model contained 18,016 CdZnTe detector elements with a total mass of ∼103 kg.

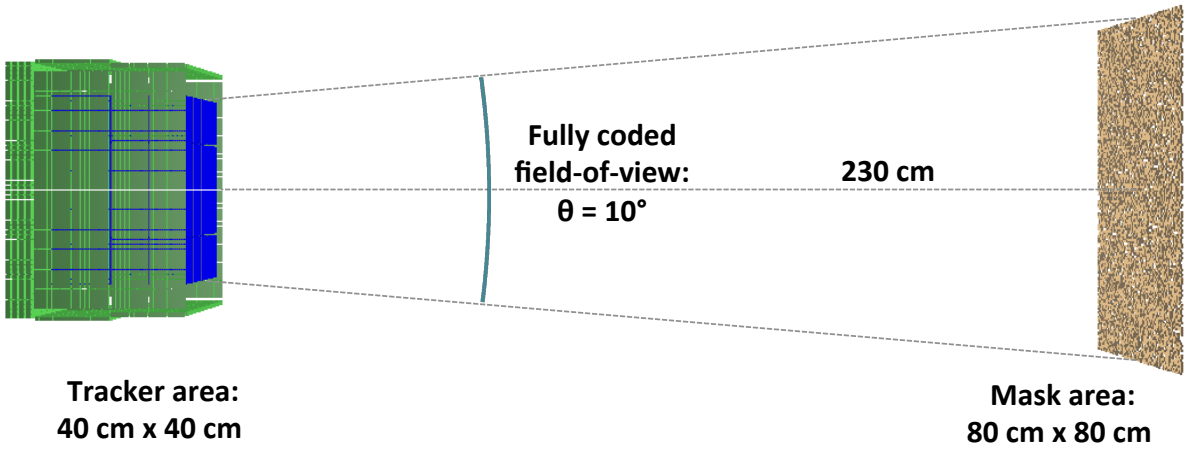

Figure 7.2: The Compton telescope combined with the tungsten coded mask with a separation distance of 2.3 meters

7.3.3 Coded Mask

The Compton telescope is combined with a 50% filled tungsten mask (Z = 84) with a size of 80 x 80 cm. The mask consists of 0.5 cubic centimeter pixels arranged in a 160 x 160 random mask pattern (not optimized). The pixel spacing and the distance from the mask to the Compton telescope was designed to provide a 10° FoV and an angular resolution, Φ, in pointing mode of 0.125° (∼7.5 arcminutes). This is described in Eq. 7.1 (previously Eq. 5.12), where the separation distance from mask to detector is $L = 2.3$ meters and d represents the 0.5 cm pixel spacing. The 5 mm thickness of the pixels provides a ∼60% attenuation for 511 keV gamma rays.

$$\Phi = arctan(d/L) \tag{7.1}$$

The mask with telescope is shown in Fig. 7.5. The geometric mask area is 6400 cm^2 and has a total mass of ∼30 kg.

7.3.4 Anti-coincidence Shield

An organic plastic scintillator anti-coincidence (AC) shield surrounds the Compton telescope on all sides, (Fig. 7.1, red). The AC shield allows for the veto of unwanted charged particle background events. An energy resolution of 10 keV (1σ Gaussian) and a trigger threshold of 50 keV were used for the shield. The total mass of the plastic scintillator and related components is ∼70 kg.

7.4 Simulated Performance

Simulations were performed using Cosima, and the data analysis including event and image reconstruction for the telescope were performed using MEGAlib, as described in Chapter 4. The instrument was placed in low-Earth, near-equatorial orbit. A series of monoenergetic far-field line sources from 200 keV to 10 MeV were simulated on-axis, as described in Table 7.1. A 511 keV source broadened by $\sigma = 1.25$ keV was also simulated at various incident angles. The broadening is based upon observations of the line from INTEGRAL/SPI (*Jean*, 2003). Additionally, a Crab-like source with a power law index of 2.17, also observed by SPI (*Sizun*, 2004), was simulated to predict the sensitivity of Space HEMI to continuum sources.

Energy (keV)	Source
200	nonspecific
511	e^+e^-, β^- decays, etc.
847	$^{56}Ni \rightarrow {}^{56}Co$
1157	^{44}Ti
1332	$^{60}Fe \rightarrow {}^{60}Co$
1809	^{26}Al
4440	$^{12}C^*$ molecular deexcitation
6130	$^{16}O^*$ molecular deexcitation
511 $\pm$1.25	broadened e^+e^- line
continuum	power law index 2.17

Table 7.1: Astrophysical nuclear line emissions and continuum source simulated with Space HEMI.

Performance estimates are given for Compton and coded-mask modes. For the Space HEMI Compton reconstruction, a slightly different method was used as compared to the HEMI prototype reconstruction. A coincidence search did not need to be applied as coincident hits are already merged together in the simulation, therefore adjacent hits were clustered together to form Compton events. It was required in the Compton Sequence Reconstruction that the first hit occur in the silicon tracker. Nominally this implies a FoV of $<90°$ due to the positioning of the Si tracker inside the CdZnTe well, however due to passive material surrounding each CdZnTe detector, transmission still occurs at higher incidence angles to allow for the first interaction to take place in the tracker. Therefore the performance was evaluated over a 120° FoV. Additionally, an Earth horizon cut was used to eliminate events which originate at or below the horizon to reduce background events generated from albedo photons.

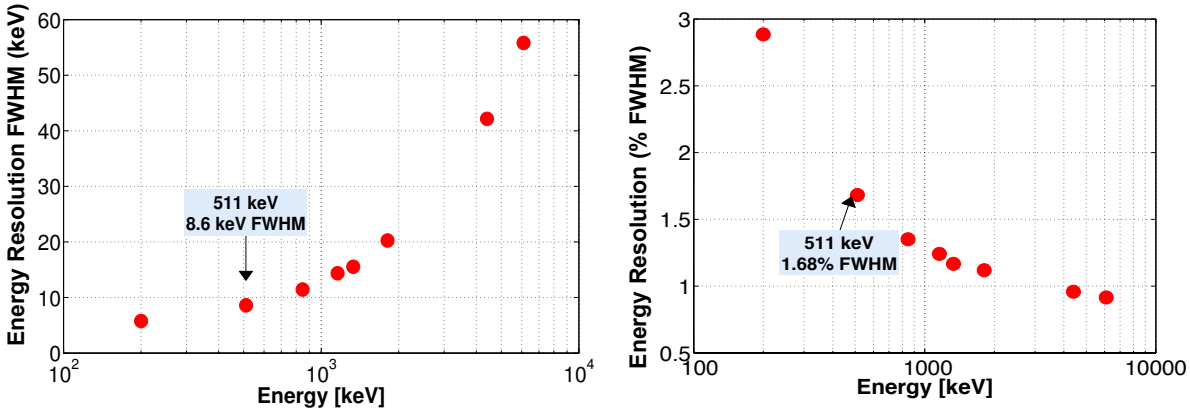

Figure 7.3: Energy resolution, including multiple-site events, as a function of energy in terms of the FWHM, left, and percent, right.

7.4.1 Energy Resolution

Using the performance parameters described in the previous section, the simulated photopeak energy resolution for the telescope is shown in Fig 7.3 as a function of energy in terms of the FWHM, left, and percent, right. This estimation includes multiple-site events. The overall energy resolution of the telescope corresponds to 1.68% FWHM at 511 keV.

The telescope energy resolution depends upon the energy resolutions of both the silicon tracker and the CdZnTe absorbers. After Compton reconstruction, the good energy resolution of the Si DSSD detectors is reflected in the overall energy resolution of the telescope because most of the Compton interactions occur in the tracker. The energy resolution of each hit adds in quadrature to get the total energy resolution per event. For a 3-site event, for example, the total energy resolution is given by Eq. 7.2.

$$\Delta E_{tot} = \sqrt{\Delta E_1^2 + \Delta E_2^2 + \Delta E_3^2} \tag{7.2}$$

7.4.2 Angular Resolution

As described in Chapter 5.4.3, for Compton events the angular resolution measurement (ARM) is defined as the angular distance between the known source position and the closest reconstructed position on the Compton cone (i.e. the ARM is the width of the Compton cone). It is a function of energy resolution, position resolution, and Doppler broadening. Fig. 7.4 shows the ARM as a function of energy, left, and incidence angle for a 511 keV broadened line source, right. A $\pm 3\sigma$ photopeak energy window was used to determine the ARM. The degradation in the ARM at higher incidence angles is due to geometric effects. Because a photon is more likely to scatter into a neighboring detector rather than between planes at higher incidence angles, the average distance between the first two interactions is

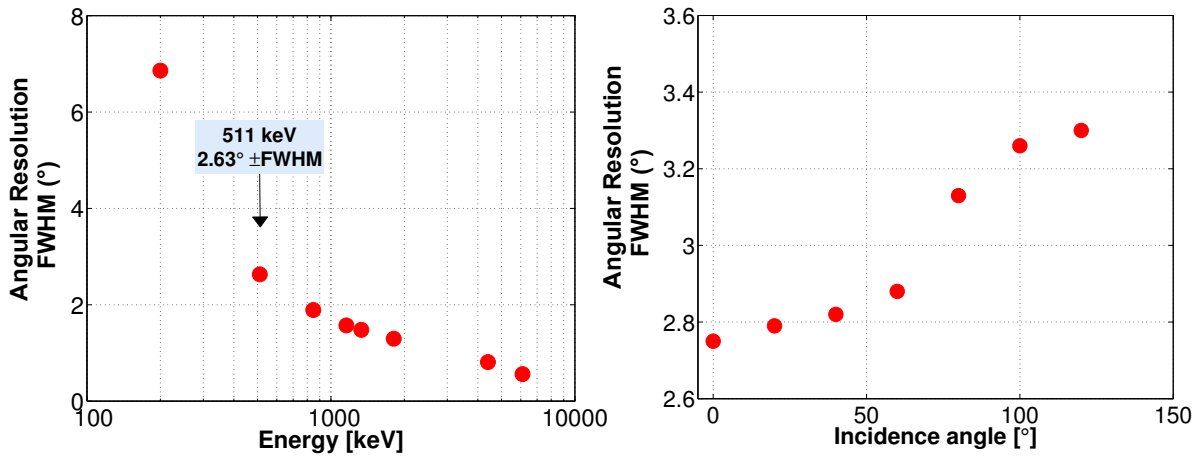

Figure 7.4: Angular resolution measurement as a function of energy, left, and incidence angle, right, for a 511 keV broadened line source, right. For sources that pass through the 10° mask FoV, the angular resolution is 0.125°.

shorter, i.e. 9.9 cm at 120° vs 13.2 cm for on-axis photons. The angular resolution within a 10° FoV is 0.125° at all energies as a result of the coded mask design. This is roughly a factor of 20 improvement at 511 keV over the achievable angular resolution in Compton mode.

7.4.3 Effective Area

As described in Chapter 5.5.1, the effective area is a reduction from the actual geometric area of a detector due to the intrinsic detection efficiency and the event cuts required for Compton reconstruction. The event cuts include an energy window of $\pm 1.4\sigma$ around each line energy, an ARM cut of $\pm 3\sigma$, and an Earth horizon cut. No mask was included in these simulations. Given the 50% open fraction of the mask and a 60% transmission of 511 keV photons through tungsten, one can expect a 30% reduction in effective area within the 10° FoV: The effective area is 183 cm^2 for the Compton telescope without the mask and 132 cm^2 with the mask at 511 keV.

7.5 Sensitivity Estimates

The sensitivity of Space HEMI can be determined based upon the effective area estimates and a model of the expected background flux. There are several challenges to achieving a high sensitivity in a Compton telescope. The flux from astrophysical gamma-ray sources is typically low, especially compared to the background flux from cosmic rays and the Earth's albedo. Additionally activation of both passive and active components of the telescope,

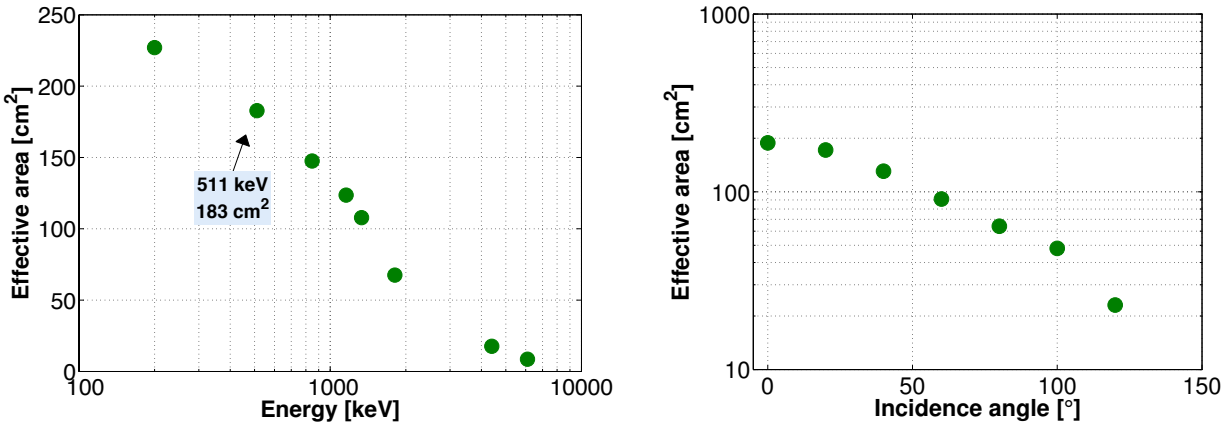

Figure 7.5: Effective area as a function of energy, left, and as a function of incidence angle for a broadened 511 keV source, right.

particularly from cosmic-ray interactions as well as charged particles trapped in the Earth's magnetic fields, creates a pervasive source of background which generally either reaches a statistical equilibrium or continues to increase over time. In addition to the low flux from target gamma-ray sources, the total interaction cross-section reaches a minimum in the Compton regime. Therefore good background reduction techniques are essential for obtaining high sensitivity and can be achieved through a combination of a good telescope design, good energy and angular resolution, CSR discrimination, and through careful event selections.

7.5.1 Background Model

Because gamma-rays are absorbed by the Earth's atmosphere, observations of astrophysical sources require placing the telescope at balloon altitudes or in space. The expected background for Space HEMI is hugely dependent upon the choice of orbit for the satellite. In this case, a near-equatorial, low-altitude orbit was chosen. This orbit would minimize exposure to cosmic rays and to high-energy charged particles in the South Atlantic Anomaly. A 575 km orbit with a 6° inclination has been extensively studied for the NuSTAR mission (*NuSTAR collaboration*), thus the NuSTAR background model was used for this study.

The gamma-ray background, shown in Fig. 7.6, consists of extragalactic X-rays and γ rays, annihilation photons, albedo photons up to several MeV, electrons, positrons, protons, and neutrons. Activation within passive and active volumes of the instrument from hadronic interactions were included in the simulation.

The Compton reconstructed background components, shown in Fig. 7.6, were simulated and then reconstructed using the BackgroundMixer program in MEGAlib. From the multiple components one can see that the 511 keV background is excessive, thus making high

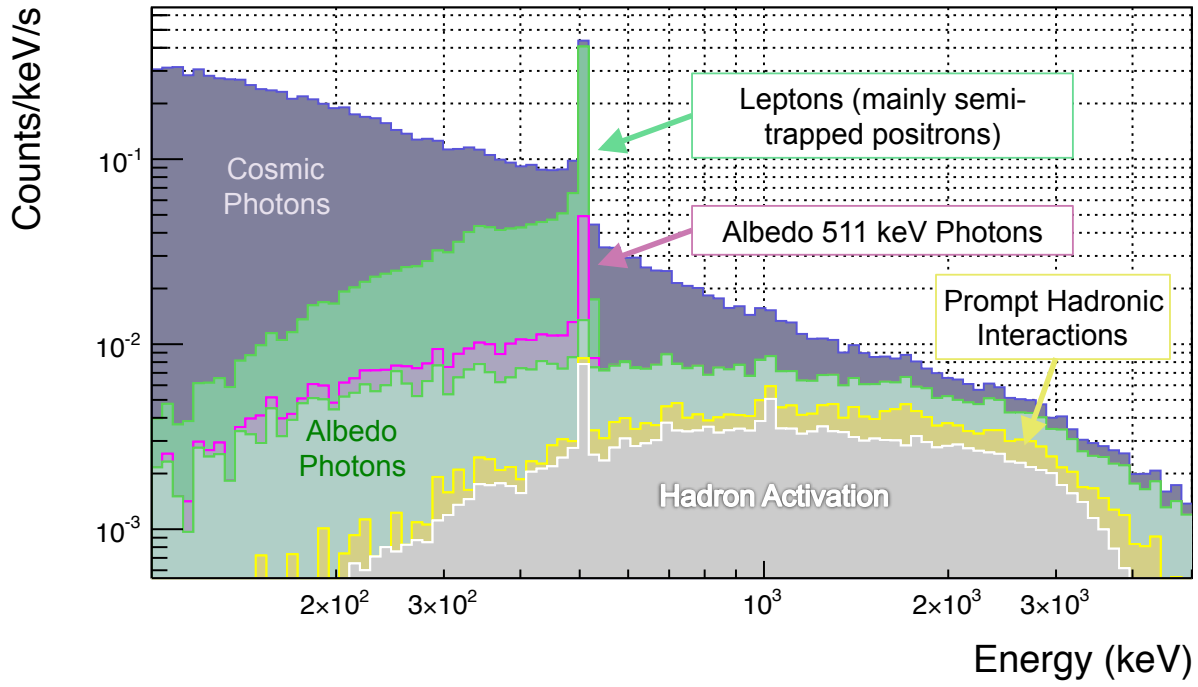

Figure 7.6: Reconstructed background after sensitivity optimized event cuts for a 575 km orbit with a 6° inclination.

sensitivity of true sources at this energy very challenging.

7.5.2 Sensitivity

The telescope sensitivity is a description of the minimum flux which can be measured by the instrument within a given significance above background. Fig. 7.7 shows the calculated sensitivities with optimized event cuts as a function of energy for monoenergetic narrow line sources, left and the continuum sensitivity for a simulated Crab-like source with a power law index of 2.17. The observation time was 1 megasecond in pointing mode. For scanning the whole field-of-view over a two-year observation time, the all-sky sensitivity of a 511 keV broadened line source is 3.6 x 10^{-6} ph/cm^2/s. Simulations for the calculated sensitivities do not include the coded mask.

7.6 Image Reconstruction

Compton and coded-mask imaging techniques can be combined to obtain better resolution of point sources by taking advantage of the good background rejection capabilities of a Compton telescope and the high angular resolution achievable from coded mask. First Compton event

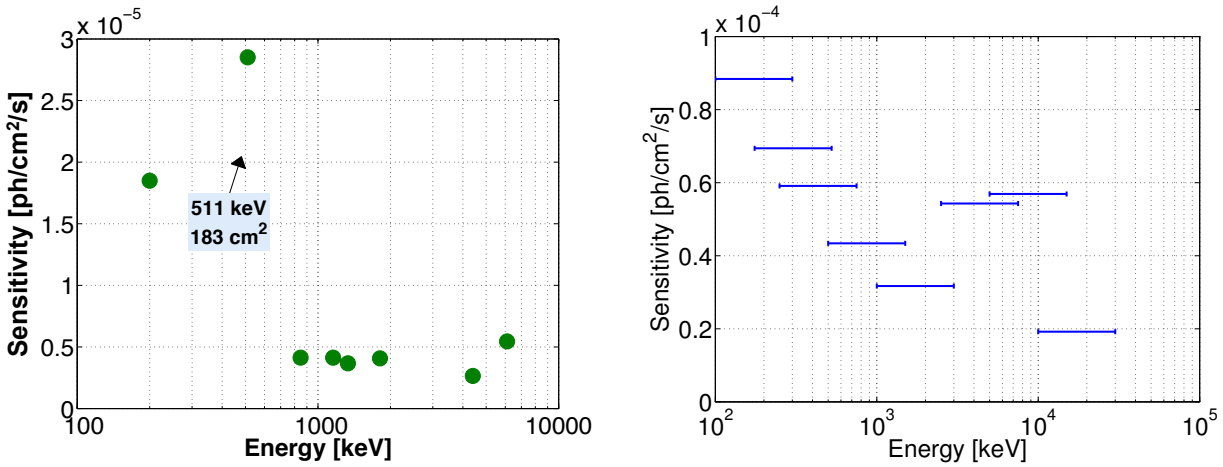

Figure 7.7: Sensitivity as a function of line source energy, left, and continuum sensitivity for a simulated Crab-like source, right, over an observation time of 1 Ms.

reconstruction and imaging is performed. The region of overlap of the Compton circles identifies the source location with an angular resolution as given by the ARM distribution. For each reconstructed point of origin, the probability that the photon was photoabsorbed as it passed through the mask is calculated. This results in a shadow pattern projected onto each Compton event circle as illustrated for an image reconstruction of one Compton event in Fig. 7.8. The pixellation of the pattern limits the point of origin, thus greatly improving the angular resolution.

Fig. 7.9 shows a demonstration of the multimode imaging capabilities of Space HEMI. Simulations of two 511 keV point sources separated by 0.2 degrees were performed. A list-mode maximum-likelihood expectation-maximization algorithm was used for the deconvolved images. In the top two images, only reconstructed Compton events were used. Both before and after deconvolution the two sources are not separable. The image reconstruction in the bottom two images takes into account the absorption probabilities of the initial photons through the coded mask. The image before the deconvolution shows some additional noise due to the overlapping coded-mask patterns superimposed onto the Compton imaging space. However, the deconvolved image clearly shows that the two sources can be separated.

7.7 Comparison with Other Space Instruments

To assess the capabilities of Space HEMI as a future telescope, Tables 7.2 and 7.3 show comparisons of performance parameters at 511 keV and 1809 keV, respectively, of the instrument to other medium-energy gamma-ray telescopes, e.g., INTEGRAL/SPI as described in Chapter 2 and an Advanced Compton Telescope (ACT) design based upon germanium detectors. One can see from the table that for nuclear line spectroscopy, the germanium-

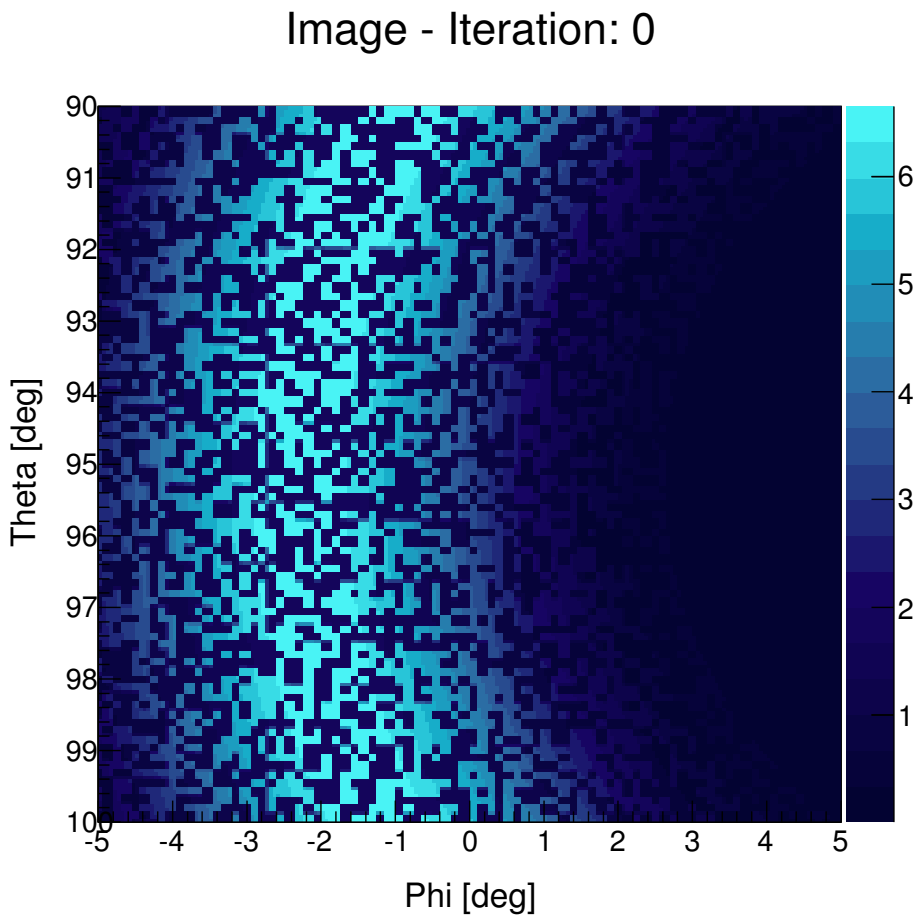

Figure 7.8: Reconstructed Compton circle (backprojection) overlaid with the projected mask pattern. The pixellation of the mask within a narrow FoV significantly improves the angular resolution.

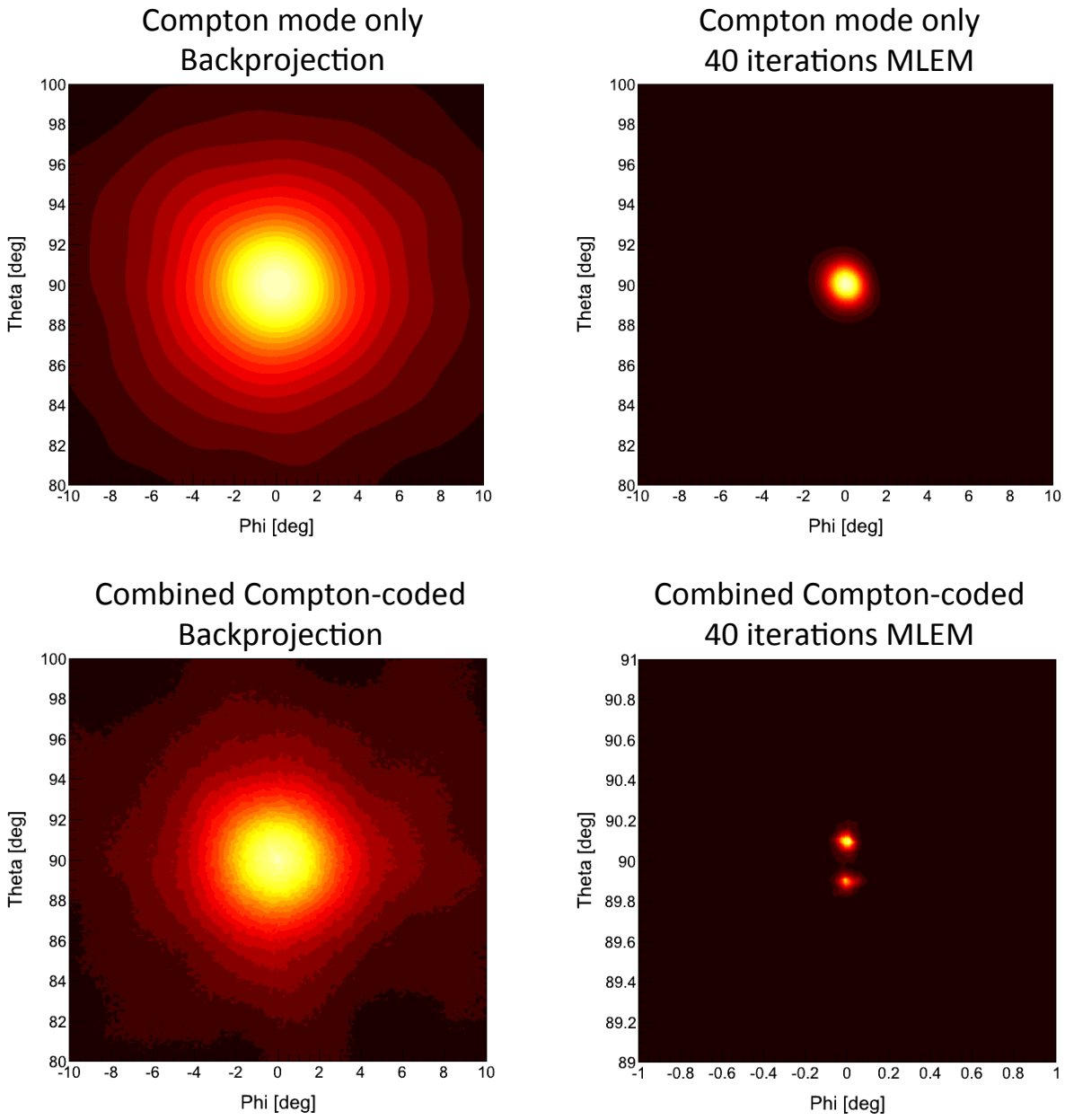

Figure 7.9: Top left: Back projection using Compton mode only. Bottom left: Back projection using a combined Compton-coded mask mode. Top right: Deconvolved image after 40 iterations in Compton mode only. Bottom right: Combined Compton and coded-mask mode image after 40 iterations. Note the change in scale between the bottom two images (images courtesy Andreas Zoglauer).

based instruments significantly exceeds the performance of Space HEMI in terms of energy resolution. However, the angular resolution without the mask is comparable to the other two instruments. A big improvement at lower energies is seen in angular resolution with the use of the mask. Theoretically, a mask can be added to any future Compton telescope in order to achieve a high angular resolution at energies below ∼0.5 MeV, depending upon the mask thickness and material.

In terms of sensitivity, the Space HEMI design is a good candidate for a next-generation telescope. It exceeds the sensitivity of SPI, although the sensitivity is not as good as the germanium ACT sensitivity. However, a direct comparison is difficult because the geometric area of the ACT and consequently its effective area are much larger than Space HEMI. For a direct comparison, the instrument would need to be scaled and other factors would also need to be considered, such as cost and detector availability.

Table 7.2: Telescope Performance Comparison at 511 keV

	Space HEMI	INTEGRAL/SPI	ACT (Ge, 2005)
Energy Resolution (% FWHM)	1.68	0.38	0.51
Angular Resolution (° FWHM)	2.63° Compton 0.125° with mask	2.5°	2.6°
Effective Area (cm^2)	183	∼100	801
3σ Sensitivity on-axis ($ph/cm^2/s$)	8.8 x 10^{-6}	4.8 x 10^{-5}	1.7 x 10^{-6}

Table 7.3: Telescope Performance Comparison at 1809 keV

	Space HEMI	INTEGRAL/SPI	ACT (Ge, 2005)
Energy Resolution (% FWHM)	1.12	0.14	0.19
Angular Resolution (° FWHM)	1.30°	2.5°	1.4°
Effective Area (cm^2)	68	∼85	479
3σ Sensitivity on-axis ($ph/cm^2/s$)	4.12 x 10^{-6}	3.1 x 10^{-5}	2.1 x 10^{-7}

(*ESA SPI Observer's Manual*, 2011, and *NASA ACT Study Report*, 2005)

7.8 Summary

Based upon laboratory measurements and benchmarked simulations of the HEMI CdZnTe detectors, the Space HEMI telescope has achievable energy resolutions of 1.68% FWHM at 511 keV and 1.11% at 1809 keV, on-axis angular resolutions in Compton mode of 2.63° ±FWHM at 511 keV and 1.30° ±FWHM at 1809 keV, and is capable of resolving sources to at least 0.2° at lower energies, e.g., 511 keV, with the use of a coded mask. An initial assessment of the instrument yields an effective area of 183 cm^2 at 511 keV and an anticipated all-sky sensitivity of 3.6 x 10^{-6} photons/cm^2/s for a broadened 511 keV source over a 2 year observation time. Additionally, combining a coded mask with a Compton imager to improve point source localization for positron detection has been demonstrated.

These capabilities meet several scientific objectives in medium-energy gamma-ray astronomy, such as achieving the sensitivity and accuracy required for nuclear line studies and allowing for improved observations of the spatial distribution of Galactic 511 keV emission. However, an Advanced Compton Telescope design using detectors with better energy resolution, such as germanium, would significantly improve the sensitivity to line emission. However the Space HEMI design and achievable sensitivity would serve well as a telescope for an all-sky survey. A CdZTe detector array, in particular, is a good candidate as an absorption plane behind a tracker, as demonstrated, or as an absorbing focal plane behind a wave optics telescope, such as in a Laue lens instrument.

Although this study focused primarily on applying the HEMI detector technology and multimode concept to a space mission, improvements to the simulated performance is anticipated with the use of the silicon tracker in its full capacity. The tracker is capable of reconstructing the direction of the recoil electron for incident photon energies above ∼2 MeV. This reduces the reconstructed Compton circle to an arc, as many incident directions can be eliminated by tracking the recoil electron. Additionally, for energies higher than 5 - 10 MeV pair production processes dominate in silicon, and the tracker can be used to track the electron-positron and determine the initial photon direction using conservation of momentum.

Chapter 8

Closing Remarks

The goal of the development of the HEMI prototype instrument and software was to demonstrate the capabilities of CdZnTe detectors as well as the multimode imaging concept with an active coded mask for nuclear threat detection. To this end, the instrument was successfully characterized and exhibits good detector response both in the laboratory and in the field. In addition, the multimode imaging capabilities for point sources were demonstrated. Field testing from an aerial platform proved the instrument and its detectors capable of good performance and stability despite elevated temperatures, high humidity, and vibrations. Additionally, the use of CdZnTe detectors and multimode imaging in an astrophysical telescope design demonstrated the potential for achieving high sensitivity and excellent angular resolution for space-based observations. Although the prototype instrument and the benchmarked detector response proved successful in these applications, there remain several paths for optimization of the instrument as well as technological challenges that need to be addressed prior to widespread deployment of a CdZnTe-based, HEMI-type instrument. The main advantages, limitations, and means for improvement of the instrument design and technology are summarized below.

8.1 CdZnTe Detector Technology

Since CdZnTe detectors can operate at ambient-temperatures, they are a prime candidate for their application in future gamma-ray instrumentation. This work has demonstrated that large-volume, coplanar-grid detectors can offer advancements in several fields due to their good response, simplified electronics, and minimal operational requirements. The detector response proved stable over time as well as in extreme environments, such as during the field testing in Fukushima. However, several improvements can be made to this technology and its readout electronics which will enhance the capabilities of CdZnTe-based instrumentation for future applications.

Data Acquisition Hardware and Software

With respect to the readout electronics, the front-end electronics that are packaged with each CdZnTe detector work well, however the data acquisition system has a few drawbacks. The energy resolution becomes degraded at high countrates because a baseline restoration was not implemented in the system. Furthermore, the energy range of the CdZnTe detectors is cutoff in the low end of the spectrum due to the high noise floor. This is a result of possible noise-induced triggering near the low-energy threshold as well as the coarse adjustment of the noise threshold in the Peak Detect Derandomizer (PDD) ASIC (see Chapter 3). The noise floor issue limits the detection of photons below ∼40 keV for both single-site hits and for Compton scattered photons that result in energy depositions below the noise threshold, thus leading to incomplete Compton events. The consequence is a reduction in the Compton efficiency, effective area, and ultimately the sensitivity of the instrument. An additional drawback in the data acquisition system is the saturation at higher energies limiting the range to below ∼2.5 MeV due to settings in the overall gain adjustment in the system.

These issues can be addressed either through system redesign, such as adding a baseline restoration to the DAQ or adjusting the gain to obtain a higher range. Other solutions include ASIC design iterations or replacement of the PDD ASIC readout with discrete electronics. The latter solution has been proven effective for the commercially-produced Kromek CdZnTe detectors (*Amman, private conversation*).

Additionally, the DAQ boards have several channels which are nonoperational, thus limiting the efficiency and uniformity in response of the instrument. This is especially an issue for coded-mask reconstruction, as dead channels in the front plane interfered with the placement of detectors in the optimized mask pattern. Dead channels in the backplane also created spatial biases in the field-of-view, although the inactive channels were reproduced in the simulation. This issue could be addressed by replacing faulty components or the data acquisition boards, however spare parts were not available during the course of the HEMI project.

Timing

The time response of the HEMI detectors was a major limitation in reconstructing the data from the field. The large number of chance coincidences caused a very poor signal-to-noise ratio in imaging mode. One way to discriminate against chance events in the reconstruction is to reduce the Compton coincidence window. The coincidence window is set by two factors: 1. The drift time of the electrons across the length of the detector, and 2. The uncertainty in the pick-off time from the shaped signal.

To address the first issue, the drift time is a function of the electron mobility, the drift length, and the applied bias voltage. Using smaller detectors would decrease the length and subsequently reduce the drift time. In terms of electron mobility, improvements may be possible with further advancement in the growth processes of CdZnTe. Improvements in the fabrication process as well as the application of moderate cooling would allow for operation at higher bias voltages.

The uncertainty in the pick-off time is due to the time being collected after the signals are shaped. Changes could be made to the front-end electronics to obtain the hit time from the pre-shaped pulses. Furthermore, an ASIC redesign could allow for more precise timing via readout of the cathode signal. This would provide better timing accuracy through a depth of interaction measurement, i.e. using the ratio of the grid to the cathode signals (*He*, 2000), thus leading to a significant improvement in the position resolution as well. This design change, albeit with a sacrifice in terms of simplicity, would allow for a more narrow Compton coincidence window, thus improving the background rejection capabilities of a CPG CdZnTe-based instrument.

CdZnTe Material

The development of CdZnTe as a detector material has been motivated primarily by its capability to operate with little or no cooling. With the invention of the coplanar-grid method, large-voxel CdZnTe detectors became capable of good spectroscopy and energy resolution, although there is still room for improvement. By reducing broadening mechanisms through moderate cooling and applying a higher bias voltage, an energy resolution of 1% FWHM at 662 keV has been achieved (*Amman*, 2006). However with the current design and fabrication methods and without cooling this resolution is unattainable. This is due in part to non-uniformities that occur in the growth process that lead to charge carrier trapping, thus causing spatially nonuniform trapping and limiting the energy resolution.

These irregularities and inclusions in the crystals lead to large variations in the detector-to-detector performance. For the HEMI-96 instrument, the energy resolutions varied by as much as a factor of two. This was initially an issue for the coded-mask reconstruction: The same energy cut was applied to the photoabsorbed peaks of each detector. The differences in peak-broadening from detector-to-detector resulted in differences in efficiency within the specified energy window, leading to uncertainty in the reconstructed source position. However, this issue was resolved by taking the individual detector performance into account in the simulation.

Improvements to the CdZnTe detector performance, such as advancements in the growth process to obtain better material uniformity or modifications to the electrodes to improve the charge collection efficiency, may lead to better energy resolution in the future. Additionally, the application of moderate cooling has shown to improve the energy resolution of CdZnTe detectors (*Amman*, 2006).

CdZnTe Atomic Number

An additional factor in the choice of CdZnTe as a detector material is its high atomic number. It is advantageous in terms of photoabsorption probability, however the Compton scattering cross-section is very low as compared to lower-Z materials, such as silicon. This is one factor that reduces the Compton efficiency and subsequently the effective area and sensitivity of the HEMI instrument. Additionally, high-Z materials have a high Doppler

broadening, thus limiting the achievable angular resolution in Compton mode. However, the limiting factor for the HEMI CdZnTe detectors is by far the position resolution.

Voxel Size

The cubic centimeter CdZnTe crystals allow for a simplified instrument design, as they greatly reduce the amount of electronics required to operate the system. This subsequently limits the number of electronics-induced problems that always occur in real-world operations. However, a significant compromise in terms of performance is imposed by the use of large voxels.

The main issue with the large-volume detectors is that the position resolution is determined by the size of the detector. This affects the achievable angular resolution in Compton mode as it induces a large uncertainty in position, especially for nearby detector-to-detector hits, e.g., hits within the same plane. This results in either a broad ARM distribution with long tails or in events whose interaction sequence cannot be reconstructed, thus reducing the effective area and subsequently the sensitivity. The effective area of HEMI in Compton imaging mode is reduced by half through the ARM cut, but more significantly, the area is reduced by over 80% due to the geometry cut to eliminate events where the first two hits occurred within the same plane. The best way to remedy this problem is to reduce the voxel size. Alternative HEMI configurations may also improve the effective area, as discussed in the geometry section below.

The large voxel size also leads to misreconstructed Compton events for several other reasons. Compton scatter events that occur within the same detector cannot be separated in the measurement. As seen in the simulation, many events have two hits per voxel. For single-site events this is not an issue, but if an additional scatter occurs after such an event, the reconstructed Compton scatter angle will be incorrect. Additionally, reconstructing the full-energy from an escape photon using Compton Sequence Reconstruction, as described in Chapter 5, cannot be used for HEMI event data because of the large uncertainty in the interaction locations.

With regards to coded-aperture mode, because the mask pixel size and spacing is limited to the cubic centimeter voxels, adding the mask doesn't improve the angular resolution over Compton mode, as demonstrated in the Space HEMI design. Much finer angular resolution can be achieved by reducing the pixel size of the mask (or by increasing the distance between planes at the cost of Compton efficiency).

In summary, smaller pixels would allow for better angular resolution in both Compton and coded-mask mode, higher Compton efficiency, a larger effective area, and ultimately better sensitivity, albeit at the cost of simplicity. As mentioned under the Timing section, a depth of interaction method would also improve the position resolution, but additional electronics and an ASIC design would be needed.

Detector Production

With regards to the CdZnTe material growth and detector fabrication, a large-scale deployment of HEMI-type instruments would entail large-scale commercial production of CPG detectors. For the HEMI instrument development, a production rate of ∼200 detectors per year was demonstrated by Redlen Technologies. An increase of several orders of magnitude in production would be needed to build numerous portable instruments for nuclear security purposes, a large FoV instrument for environmental monitoring, or for an astrophysics instrument, such as Space HEMI. To increase the yield at low cost and without sacrificing detector performance, improvements to the current CPG fabrication technology as a well as additional infrastructure at the production facility would be required. To motivate this step forward, a continued demand and a stable market for CPG CdZnTe detectors would need to be established.

8.2 HEMI Geometry

The present HEMI configuration is sufficient for laboratory testing and demonstration purposes. However, to improve the efficiency and sensitivity for real-world applications, the instrument would need to be modified to minimize geometric biases in the present design, enlarge the field-of-view, and increase the effective area.

As evident in the imaging particularly for the field measurements, the present HEMI configuration shows geometrical biases in the reconstructed Compton events. These biases are primarily due to the misreconstruction of plane-to-plane scattering events and from events that scatter in the front plane but do not reach the back plane. The former issue is addressed above (see section on "Voxel Size"), but may also be improved by choosing a different configuration for the instrument, e.g., larger spacing between detectors.

Aside from reducing the voxel size of the detectors, the best solution to the geometrical biases is to redesign the instrument to have a much larger, more even field-of-view. To first order, reinvestigating the plane-to-plane spacing of the current configuration could improve the FoV. An optimized spacing was determined early in the program, although the simulations were performed prior to the full characterization of the detector response. However, any improvement in the FoV for the current design can only be obtained at the cost of the angular resolution of the system.

Ideally, an instrument that effectively increases the solid angle coverage of the instrument is needed. Half-spherical arrays as mentioned in Chapter 5, for example, would increase the FoV leading to an increased effective area in Compton mode, as a greater range of incident photon angles could be reconstructed. Such a configuration would also address the small field-of-view effect that was seen for the field measurements, i.e. the field-of-view of the instrument was not much larger than the size of the source (see Chapter 6). For any significant improvements in the FoV, a complete redesign of the instrument would be necessary.

The other issue with respect to the HEMI field-of-view is that the front plane is the same size as the backplane. In mask mode, this results in all off-axis sources within the FoV

being only partially coded, thus making localization of these sources much less accurate as demonstrated in Chapter 5. For a pointing instrument this geometry may be ok, but for applications where the source location is unknown imaging in mask mode is not very reliable. Additionally, as mentioned in Chapter 5 the small mask area constrains the possibility of having a truly random pattern and a completely uniform FoV. This limits the uniqueness of the projected shadow pattern, thus degrading the image quality.

Another issue with having stacked detector arrays of the same size is that gamma rays (either background or source emissions) at large incidence angles, e.g., angles greater than $\sim 50^{\circ}$ for the current configuration, can miss the front plane but hit the backplane. In mask mode, this kind of event would alter the shadow pattern of any real sources within the smaller field-of-view, thus preventing accurate reconstruction. In Compton mode it can significantly increase the number of chance coincidences, which was particularly a problem for the HEMI field measurements. The effect in Compton mode, however, is easy to correct, as one can require that only events where the first hit occurs in the front plane is included in the reconstruction.

At least two approaches to resolve the array size problem can be taken. First, the mask can be made much larger than the backplane to increase the overall FoV in Compton mode and the fully-coded FoV in mask mode. This design change could be relatively simple, but would require the addition of more detectors and electronics, as well as a redesign of the DAQ boards and support structures. The result would be, perhaps, a less portable system with a larger payload and greater power consumption, but would provide a much better field-of-view for both imaging modalities. A simpler change can be made by adding shielding around the outside of the instrument on 4 sides (or 5 sides for applications where upscattered photons are expected) to avoid hits that first hit the backplane. This would make the instrument slightly less portable, and for field operation this change would require deployment using a UAV capable of a higher payload.

8.3 Future Applications

The proven CdZnTe detector performance and imaging capabilities of the HEMI instrument for the purpose of nuclear threat detection paves the way for the use of this technology for other applications. The efficacy of this technology and the HEMI design to make advancements within the three fields studied in this work are briefly summarized below.

8.3.1 Nuclear Threat Detection

Overall, the characterized performance and achievable sensitivity of the HEMI prototype fulfilled the requirements for the nuclear threat detection program. Its good energy resolution (2.4% FWHM at 662 keV) is an improvement over scintillator-based systems for this application, such as TMI discussed in Chapter 2. The spectral analyzer program developed for HEMI proved sufficient for laboratory testing with calibration sources, however the program

will need to be tested with other instruments in order to refine the settings and verify its robustness. Additionally, the detection and identification challenges in the case of shielded sources has not yet been tested.

It was originally proposed that the HEMI instrument may also have capabilities in the field of neutron detection and imaging for Homeland Security purposes. CdZnTe has a high neutron capture cross-section for thermal neutrons, particularly in the isotope ^{113}Cd. Simulations were performed of 1 meV neutrons incident on-axis upon a HEMI-96 instrument. In the single-detector hit energy spectrum very clear peaks were present as expected from prompt gamma emission following neutron capture, particularly at 558 keV as a result of the ^{113}Cd(n, γ)^{114}Cd reaction. However the gamma-rays emitted from the capture/decay process have no preferential direction and therefore cannot conventionally be traced back to the origin of the incident neutron. Further investigation of the possibility of neutron imaging with a HEMI-like instrument is beyond the scope of this work.

8.3.2 Environmental Monitoring in Fukushima

During field testing, the HEMI instrument demonstrated reliability and good spectral performance, i.e. 2.5% - 2.8% FWHM at 662 keV, even under extreme environmental conditions. Initial surveys of the area, particularly on the ground, emphasized the need for better means of assessing ground activities prior to rehabitation of affected areas. Compton imaging proved effective with the HEMI prototype in the lab, however in the field the instrument was limited by its restricted and uneven field-of-view and high false coincidence rate. To first order, resolving the possible buffering issue in the DAQ would allow for a more accurate assessment of ground activity and possibly improve the imaging. Improvements for field measurements could also be obtained by repatterning the front plane of detectors to optimize for efficiency in Compton mode, as lower energy source localization through mask mode is not relevant for detection in Fukushima. Furthermore, improved image reconstruction methods can be developed specifically for HEMI operations under these circumstances, e.g., diffuse, high activity backgrounds, diffuse sources, and background activities that are dominant in the same energy regime as the source emission. Advanced imaging techniques could prove effective for achieving the goal of efficiently localizing hotspots above a diffuse background.

The capabilities of the HEMI instrument and suggestions for further improvements and more appropriate designs have been given in Chapter 6. In summary, a future instrument for environmental monitoring, particularly with respect to the Fukushima clean-up efforts, would benefit from a larger FoV, better angular resolution, and ultimately a faster response, thus allowing for improved imaging of hotspots above a diffuse background.

8.3.3 Gamma-ray Astrophysics

Investigation of the Space HEMI gamma-ray telescope was successful in that initial estimates of its performance showed good potential for advancements in this field. The instrument design achieved high sensitivity at a much lower cost than LaBr, for example, with a simpler

and perhaps less expensive design than a germanium-based instrument, and with higher performance in terms of energy resolution than previous scintillation-based instruments, such as COMPTEL. An important aspect of this study was the use of a coded mask to greatly improve the angular resolution over a conventional Compton telescope within a small FoV. For a future telescope design based upon CPG CdZnTe detectors, production issues would need to be addressed, such as high yield and reliable performance.

As mentioned in Chapter 7, the CdZnTe telescope is not ideal in terms of nuclear line science requiring very fine energy resolution, however the simplicity of the detectors, minimal operational requirements, and good absorption properties may motivate further investigation for, e.g., its use as an absorber plane behind a Compton telescope or a focal plane for a Laue lens instrument.

8.4 Conclusions

Regardless of the current limitations of the HEMI instrument configuration and CdZnTe detectors, the benchmarked response and proven capabilities of this technology as demonstrated with the prototype instrument and through simulation is an important step towards the application of large-volume CdZnTe coplanar-grid detectors for a variety of applications. The need for ambient-temperature detector technologies across a variety of disciplines can be addressed with the use of this technology. Furthermore, the multimode imaging concept with the use of an active mask has been demonstrated and can be readily improved upon in the design of future gamma-ray imaging instruments based upon the findings of this work.

References

Ables, J. G. 'Fourier Transform Photography: A New Method for X-Ray Astronomy.' *Proc. Astron. Soc. Australia*, **1**: 172, 1968.

Agostinelli, S. et al. 'Geant4 - A Simulation Toolkit.' *Nuclear Instruments and Methods A*, **506**: 250-303, 2003.

Amman, M. and Luke, P. N. 'Optimization Criteria for Coplanar-Grid Detectors.' IEEE Transactions on Nuclear Science, **46**(3), 1999.

Amman, M. et al. 'Temperature Study of CdZnTe Coplanar-Grid Detectors.' *IEEE TNS*, **53**(5), 2006.

Amman, M. et al. 'Evaluation of THM-Grown CdZnTe Material for Large-Volume Gamma-Ray Detector Applications.' *IEEE TNS*, **56**(795), 2009.

Amman, M. et al. 'Detector Module Development for the High Efficiency Multimode Imager.' *Nuclear Science Symposium Conference Record*, **981**, 2009.

Anderson, C. 'The Positive Electron.' *Physical Review*, **43**(6): 491-494, 1933.

Aprile, E. and Doke, T. 'Liquid xenon detectors for particle physics and astrophysics.' *Rev. Mod. Phys.*, **82**, 2010.

Bandstra, M. S. et al. 'Detection and imaging of the Crab nebula with the Nuclear Compton Telescope.' *The Astrophysical Journal*, **738**(1), 2011.

Barrière, N. et al. 'Developing a method for soft gamma-ray Laue lens assembly and calibration.' *Nucl. Instrum. Meth.* **A741**: 47-56, 2014.

Berger, M. et al. 'XCOM: Photon cross sections database.' *NIST Standard Reference Database 8 (XGAM)*, 1998.

Bertolini, G. and Coche, A. 'Semiconductor Detectors.' *North-Holland Publishing Co., Amsterdam*, 1968.

Bildsten, L. et al. 'Helium destruction and gamma-ray line emission in accreting neutron stars.' *Astrophysical Journal*, **408**(2): 615-636, 1993.

Bloemen, H. et al. 'The Revised COMPTEL Orion Results.' *The Astrophysical Journal*, **521**: L137-L140, 1999.

Bossew, P. 'A very long-term HPGe-background gamma spectrum.' *Applied Radiation and Isotopes*, **62**: 635-644, 2004.

Bouchet, L. et al. 'On the morphology of the electron-positron annihilation emission as seen by SPI/INTEGRAL.' *The Astrophysical Journal*, **720**(2): 1772-1780, 2010.

Brun, R., Rademakers, F. 'ROOT - An object oriented data analysis framework.' *Nucl. Instr. and Methods in Physics A*, **389**(1-2): 81-86, 1997.

Burbidge, Burbidge, Fowler, and Hoyle 'Synthesis of the Elements in Stars.' *Rev. Mod. Phys.*, **29**(547), 1957.

E. Caroli, E. 'Coded aperture imaging in X- and gamma-ray astronomy.' *Space Science Reviews*, **45**(3-4): 349-403, 1987.

Cho, H. Y. 'Measurement of the drift mobilities and the mobility-lifetime products of charge carriers in a CdZnTe crystal by using a transient pulse technique.' *JINST*, **6**, 2010.

The CMS collaboration 'Observation of a new boson with mass near 125 GeV in pp collisions at $\sqrt{s} = 7$ and 8 TeV.' *JHEP*, **06**(081), 2013.

Compton, A. 'A Quantum Theory of the Scattering of X-rays by Light Elements.' *Phys. Rev.*, **21**: 483, 1923.

De Geronimo, G. 'Characterization of an ASIC for CPG Sensors with Grid-Only Depth of Interaction Sensing.' *IEEE TNS*, **53**(456), 2006.

Dicke, R. H. 'Scatter-Hole Cameras for X-Rays and Gamma Rays.' *Astrophysical Journal*, **153**: L10, 1968.

Diehl, R. and Timmes, F. X. 'Gamma-Ray Line Emission from Radioactive Isotopes in Stars and Galaxies.' *The Publications of the Astronomical Society of the Pacific* **110**(748): 637-659, 1998.

Diehl, R. 'Nuclear astrophysics lessons from INTEGRAL.' *Rep. Prog. Phys.*, **76**, 2013.

Dirac, P. A. M. 'The Quantum Theory of the Electron.' *Proc. R. Soc. Lond. A*, **117**, 1928.

Eckert, M. 'Max von Laue and the discovery of X-ray diffraction in 1912.' *Ann. Phys.*, **524**: A83-A85, 2012.

Ekström, L. P. and Firestone, R. B. 'WWW Table of Radioactive Isotopes.' *http://nucleardata.nuclear.lu.se/nucleardata/toi*, 1999.

European Space Agency 'SPI Observers Manual.' *INT-SOC-DOC-022*, **2**, 2011.

Friedman, J. '353QH smoothing algorithm.' *Proc. of the 1974 CERN School of Computing, Norway*, 1974.

Fuggle, J. C. and Mårtensson, N. 'Core-Level Binding Energies in Metals.' *J. Electron Spectrosc. Relat. Phenom.*, **21**(275), 1980.

Galison, P. 'Image and Logic: A Material Culture of Microphysics.' *Chicago: University of Chicago Press*, 1997.

Galloway, M. et al. 'Spectral Analysis for the High Efficiency Multimode Imager.' *Nuclear Science Symposium Conference Record*, **1119**, 2010.

Gerward, L. 'Paul Villard and his Discovery of Gamma Rays.' *Physics in Perspective*, **1**(54): 367-383, 1999.

Gold, R. 'An iterative unfolding method for response matrices.' *Argonne National Laboratories*, **ANL-6984**, 1964.

Google 'Memories for the Future.' *http://www.miraikioku.com*, 2013.

Greiner, J. et al. 'Gamma-ray burst investigation via polarimetry and spectroscopy (GRIPS).' *Experimental Astronomy*, **23**(1): 91-120, 2009.

Gunson, J. and Polychronopulos, B. 'Optimum design of a coded mask x-ray telescope for rocket applications.' *Mon. Not. Roy. Astron. Soc.*, **177**: 485-497 1976.

Habs, D. et al. 'Refractive Index of Silicon at γ Ray Energies.' *Phys. Rev. Lett.*, **108**, 2012.

Harris, M. J. et al. 'Detection of γ-ray lines from interstellar ^{60}Fe by the high resolution spectrometer SPI.' *Astronomy & Astrophysics*, **433**(3): L48-L52, 2005.

He, Z. et al. 'Measurement of material uniformity using 3-D position sensitive CdZnTe gamma-ray spectrometers.' *Nuclear Instruments and Methods in Physics Research A*, **441**(3): 459-467, 2000.

Hubbell, J. H. 'Electronpositron pair production by photons: A historical overview.' *Radiation Physics and Chemistry*, **75**: 614-623, 2006.

Hynes, M. V. et al. 'The Raytheon-SORDS Trimodal Imager.' *Proc. of SPIE*, **7310**, 2009.

In't Zand, J. J. M. 'A coded-mask imager as monitor of galactic X-ray sources.' *Ph.D. thesis, University of Utrecht*, 1992.

International Atomic Energy Agency, Vienna 'Inventory of radioactive waste disposals at sea.' *IAEA-TECDOC-1105*, 1999.

International Atomic Energy Agency 'Fukushima Nuclear Accident Update Log.' *http://www.iaea.org/newscenter*, 2011.

International Atomic Energy Agency 'The Follow-up IAEA International Mission on Remediation of Large Contaminated Areas Off-Site the Fukushima Dai-ichi Nuclear Power Plant Tokyo and Fukushima Prefecture, Japan.' *Final Report*, Oct. 2013

Jacobson, A. S. et al. 'A balloon-borne Ge/Li/ spectrometer for gamma-ray astronomy.' *Nuclear Instruments and Methods*, **127**: 115-124 1975.

Jean, P. et al. 'Spectral analysis of the Galactic e+e- annihilation emission.' *Astronomy and Astrophysics*, **445**(2): 579-589, 2006.

Kamada, K. et al. '2- inch diameter single crystal growth and scintillation properties of Ce:$Gd_3Al_2Ga_3O_{12}$.' *Journal of Crystal Growth*, **352**(1): 88-90, 2012.

Klein, O. and Nishina, T. 'Über die Streuung von Strahlung durch freie Elektronen nach der neuen relativistischen Quantendynamik von Dirac.' *The European Physical Journal A - Hadrons and Nuclei (Historical Archive)*, **52**(11-12): 853-868, 1929.

Knödelseder, J. et al. 'The all-sky distribution of 511 keV electron-positron annihilation emission.' *Astronomy & Astrophysics*, **441**: 513-532, 2005.

Knoll, G. 'Radiation Detection and Measurement.' *Wiley*, 2010.

Krane, K. 'Introductory Nuclear Physics.' *Wiley*, 1988.

Lin, R. et al. 'The Reuven-Ramaty High-Energy Solar Spectroscopic Imager (RHESSI).' *Solar Physics*, **219**: 3-32, 2002.

Lin, R. et al. 'RHESSI Observations of Particle Acceleration and Energy Release in an Intense Solar Gamma-Ray Line Flare.' *The Astrophysical Journal Letters*, **595**(2), 2003.

Luke, P. N. 'Unipolar Charge Sensing with Coplanar Electrodes- Application to Semiconductor Detectors.' *IEEE Transactions on Nuclear Science*, **42**(4), 1995.

Luke, P. N. 'Electrode configuration and energy in gamma-ray detectors.' *Nuclear Instruments and Methods in Physics Research A*, **380**: 232-237, 1996

Luke, P. N. et al. 'Electrode Design for Coplanar-Grid Detectors.' *IEEE Transactions on Nuclear Science*, **44**(3), 1997.

Luke, P. N. et al. 'A CdZnTe coplanar-grid detector array for environmental remediation.' *Nuclear Instruments and Methods in Physics Research A* **458**: 319-324, 2001.

Luke, P. N. et al. 'Factors Affecting Energy Resolution of Coplanar-Grid CdZnTe Detectors.' *IEEE TNS*, **51**(3): 1199, 2004.

Lund, N. 'A study of focusing telescopes for soft gamma rays.' *Exp. Astronomy*, **2**: 259-273, 1992.

Mariscotti, M. A. 'A method for automatic identification of peaks in the presence of background and its application to spectrum analysis.' *Nuclear Instruments and Methods*, **50**: 309-320, 1967.

Morhác, M. 'An algorithm for determination of peak regions and baseline elimination in spectroscopic data.' *Nuc. Instr. Meth. A*, **600**(2):478-487, 2009.

NASA 'Advanced Compton Telescope concept study report.' *http://www.ssl.berkeley.edu/act*, 2005.

Nobel Lectures, Physics 1901-1921. *Elsevier Publishing Company, Amsterdam*, 1967.

Normile, D. 'Cooling a Hot Zone.' *Science*, **339**: 1028-1029, 2013.

Novikova, E. I. et al. 'A γ-ray background model for Monte Carlo simulations' *Nuclear Instruments and Methods A*, **579**: 279-283, 2007.

Nuclear Regulatory Commission: *http://www.nrc.gov*.

Nuclear Threat Initiative: *http://www.nti.org*.

Nygren, D. R. and Marx, J. N. 'The Time Projection Chamber.' *Phys. Today*, **31**(N10): 46-53, 1978.

O' Connor, P. et al. 'Amplitude and Time Measurement ASIC with Analog Derandomization: First Results.' *IEEE Trans. Nucl. Sci.*, **50**(892), 2003.

Oberlack, U. et al. 'The COMPTEL 1.809 MeV all-sky image.' *Astronomy and Astrophysics Supplement*, **120**(311), 1996.

Oppenheimer, J. R. and Plesset, M. S. 'On the Production of the Positive Electron.', *Phys. Rev.*, **44**(53), 1933.

Prantzos, N. et al. 'The 511 keV emission from positron annihilation in the Galaxy.' *Rev. Mod. Phys.*, **83**(1001), 2011.

Rutherford, E. 'The Magnetic and Electric Deviation of the easily absorbed Rays from Radium.' *Phil. Mag.*, **6**(5): 177, 1903.

Rutherford, E. and Andrade, C. 'The Wavelength of the Soft Gamma Rays from Radium B.' *Phil. Mag.*, **6**: 854-868, 1914.

Ryan, C. G. 'SNIP, a statistics-sensitive background treatment for the quantitative analysis of PIXE spectra in geoscience applications.' *Nuc. Instr. Meth. B*, **34**: 396-402, 1988.

Rybicki and Lightman 'Radiative Processes in Astrophysics.' *Wiley*, 2004.

Schönfelder, V. et al. 'Instrument Description and Performance of the Imaging Gamma-Ray Telescope COMPTEL aboard NASA's Compton Gamma Ray Observatory.' *ApJ Suppl.*, **86**(657), 1993.

Schönfelder, V. 'The Universe in Gamma Rays.' *Springer*, 2001.

Sizun, P. et al. 'The INTEGRAL/SPI Response and the CRAB Observations.' In *ESA SP-552: 5th INTEGRAL Workshop on the INTEGRAL Universe*, 815-818, 2004.

Skinner, G. K. 'Diffractive/refractive optics for high energy astronomy I. Gamma-ray phase Fresnel lenses.' *Astronomy and Astrophysics*, **375**: 691-700, 2001.

Skinner, G. K. 'The sensitivity of coded mask telescopes.' *Applied Optics*, **47**: 2739-2749, 2008.

Spieler, H. 'Semiconductor Detector Systems.' *OUP Oxford*, 2005.

The Super-Kamiokande Collaboration 'The Super-Kamiokande Detector.' *Nucl. Instrum. Meth.*, **A501**: 418-462, 2003.

Tajima, T. et al. 'Soft Gamma-ray Detector for the ASTRO-H Mission.' *Proc. SPIE Int. Soc. Opt. Eng.*, **7732**(34), 2010.

Tanaka, K. 'Vertical profiles of Iodine-131 and Cesium-137 in soils in Fukushima Prefecture related to the Fukushima Daiichi Nuclear Power Station Accident.' *Geochemical Journal*, **46**: 73-76, 2012.

Vedrenne, G. et al. 'SPI: The spectrometer aboard INTEGRAL.' *Astronomy and Astrophysics*, **411**: L63-L70, 2003.

Wakeford, D. et al. 'The SORDS trimodal imager detector arrays.' *Proc. of SPIE*, **7310**, 2009.

Wilderman, S. J. et al. 'List-mode Maximum Likelihood Reconstruction of Compton Scatter Camera Images in Nuclear Medicine.' *IEEE Trans. Nucl. Sci.*, **45**:957, 1998.

World Nuclear Association: *http://www.world-nuclear.org*.

Zoglauer, A. 'Methoden der Bildrekonstruktion für das Comptonteleskop MEGA.' *Diploma thesis, Technische Universität München*, 2000.

Zoglauer, A. and Kanbach, G. 'Doppler broadening as a lower limit to the angular resolution of next generation Compton telescopes.' *X-Ray and Gamma-Ray Telescopes and Instruments for Astronomy, Proceedings of SPIE*, **4851**: 1302-1309, 2003.

Zoglauer, A. 'First Light for the Next Generation of Compton and Pair Telescopes.' *Doctoral thesis, TU Munich*, 2005.

Zoglauer, A., Andritschke, R., Schopper, F. 'MEGAlib - the Medium Energy Gamma-ray Astronomy Library.' *New Astronomy Reviews*, **50**(7-8):629-632, 2006.

Zoglauer, A. et al. 'Nuclear astrophysics capabilities of the GRIPS telescope.' *New Astronomy Reviews*, **52**(7-10): 431-435, 2008.

Zoglauer, A. et al. 'Cosima the Cosmic Simulator of MEGAlib.' *IEEE Nuclear Science Symposium Conference Record*, 2009.

Zoglauer, A. et al. 'First Results of the High Efficiency Multi-mode Imager (HEMI).' *Nuclear Science Symposium Conference Record*, **887**, 2009.

Zoglauer, A. et al. 'Aerial Standoff Detection with the High Efficiency Multimode Imager (HEMI).' *Nuclear Science Symposium Conference Record*, **566**, 2010.

Zoglauer, A. et al. 'Design, Implementation, and Optimization of MEGAlibs image reconstruction tool Mimrec.' *Nuc. Instr. Meth. A*, (626): 568-571, 2011.

Zoglauer, A. et al. 'Status of MEGAlib's Real-Time Analysis Tool Realta.' em Nuclear Science Symposium Conference Record, **1344**, 2011.

Zweibel, E. and Heiles, C. 'Magnetic fields in galaxies and beyond.' *Nature*, **385**(6612): 131-136, 1997.